POLITECNICO
MILANO 1863

The HyperLander Launch System

Giovanni N. D'Aloisio – Alessandro Zambelli – Giacomo Confetti

Maxence N. Brugerolles – Théo Helluy – Pablo Villar Peris

Francisco J. Torres Huesca – Elif Eren – Justyna W. Oleszycka

Final Report of Assignment No. 1

Course of Launch Systems
School of Industrial Engineering
Academic Year 2025-2026

Authorship Declaration

This section details the individual contributions of each team member to the *HyperLander* project. The project was developed collaboratively, with each member taking lead responsibility for specific subsystems. All team members have contributed substantially to this project according to the distribution outlined above. Moreover, each team member is capable of answering detailed questions about their specific subsystem(s), and all team members are capable of answering high-level questions regarding the overall system design and how subsystems interrelate. All team members contributed to system-level integration and consistency checks, inter-subsystem interface definition and validation, trade-off analysis, design iterations, performance budget verification, requirements flow-down and compliance verification, under the leadership of **A. Zambelli** and **G. N. D'Aloisio**.

Team Members (in Alphabetical Order)

Name & Surname	Student ID	E-Mail
Maxence Noe Brugerolles	11151155	maxencenoe.brugerolles@mail.polimi.it
Giacomo Confetti	10697125	giacomo.confetti@mail.polimi.it
Giovanni Nicola D'Aloisio (Backup Ref.)	11066730	giovanninicola.daloisio@mail.polimi.it
Elif Eren	11052783	elif.eren@mail.polimi.it
Théo Helluy	11142101	theo.helluy@mail.polimi.it
Justyna Wioletta Oleszycka	11154236	justynawioletta.oleszycka@mail.polimi.it
Francisco José Torres Huesca	11151294	franciscojose.torres@mail.polimi.it
Pablo Villar Peris	11151964	pablo.villar@mail.polimi.it
Alessandro Zambelli (Ref.)	10771223	alessandro1.zambelli@mail.polimi.it

Work Distribution by Design Areas

Payload
Lead: G. N. D'Aloisio
Contributors: F. J. Torres Huesca, G. Confetti

Propulsion
Lead: G. N. D'Aloisio & T. Helluy
Contributors: A. Zambelli

Structures
Lead: A. Zambelli & G. N. D'Aloisio
Contributors: T. Helluy, J. W. Oleszycka

Layout, Mass Distribution & Graphics
Lead: G. N. D'Aloisio
Contributors: T. Helluy, A. Zambelli

Ascent Trajectory
Lead: A. Zambelli & G. Confetti
Contributors: M. N. Brugerolles, P. V. Peris, F. J. Torres Huesca

Descent Trajectory & Re-entry
Lead: F. J. Torres Huesca & G. Confetti
Contributors: M. N. Brugerolles, P. V. Peris, G. N. D'Aloisio

Aerodynamic Modeling
Lead: G. Confetti
Contributors: E. Eren & A. Zambelli

Carrier Analysis
Lead: M. N. Brugerolles
Contributors: G. Confetti

Guidance, Navigation & Control
Lead: E. Eren

Risk, Reliability and Safety
Lead: P. V. Peris
Contributors: F. J. Torres Huesca, A. Zambelli

Copyright Notice

Team Members and Section Leadership

Each section of this work is the intellectual property of its respective lead author(s), with contributions from team members as specified in the Authorship Declaration.

Restrictions

No part of this publication may be reproduced, distributed, or transmitted in any form or by any means, including photocopying, recording, or other electronic or mechanical methods, without the prior written permission of the authors, except in the case of:

- Brief quotations embodied in critical reviews and certain other noncommercial uses permitted by copyright law
- Academic citation with proper attribution
- Internal use by Politecnico di Milano for educational and assessment purposes

Permission Requests

For permission requests or inquiries regarding commercial use, please contact the team representatives:

- Alessandro Zambelli: alessandro1.zambelli@mail.polimi.it
- Giovanni Nicola D'Aloisio: giovanninicola.daloisio@mail.polimi.it

Disclaimer

This work was prepared as an academic assignment for the Course of Launch Systems at Politecnico di Milano. While every effort has been made to ensure accuracy, the authors make no warranty, expressed or implied, regarding the completeness, reliability, or suitability of the information contained herein for any particular purpose.

Acknowledgements

We wish to dedicate this work and express our sole and profound gratitude to the *Hypersonic Cow*. That in change of faith in its perfect aerodynamic design, protects aerospace engineers in whatever aerospace engineers do.

Your inspiration was the necessary thrust.

> *We choose to go to the Moon and do the other things in this decade,*
> *not because it they are easy, but because they are hard.*
>
> *J. F. Kennedy*

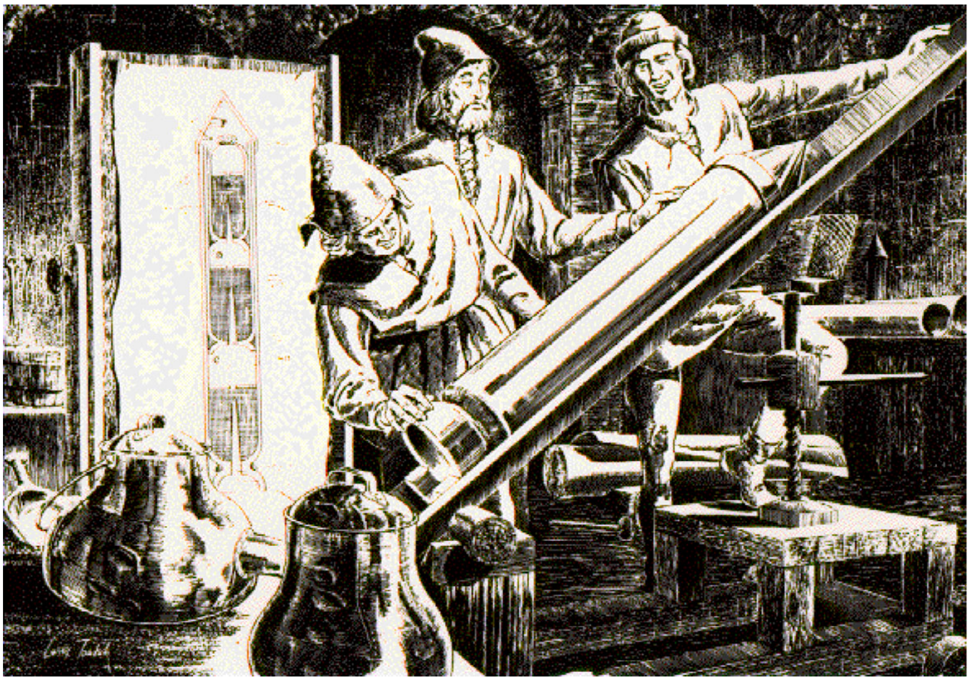

Figure 1: Building a staged rocket, drawing from artillery expert Kazimierz Siemienowicz.

Executive Summary

This report presents the comprehensive design, analysis, and sizing of an air-launched **Two-Stage-To-Suborbit** (TSTS) launch system for crewed antipodal point-to-point transportation. The mission requires delivering **6 passengers** across ~ 20000 km with ± 20 km landing accuracy via a ballistic trajectory, using an **expendable launcher** with **high TRL** (Technology Readiness Level > 6, AD2 risk $< 40\%$) and parachute-based landing system.

After rigorous trade-off analysis of ground-based and air-launched architectures, the selected baseline is an **air-launched TSTS system** carried by the **Scaled Composites Model 351 Stratolaunch** *Roc* aircraft, featuring a **winged Pegasus ® XL-style rocket** with **LOX/LCH$_4$** propulsion for both stages, obtained by rescaling the Sea-Level & Vacuum versions of the SpaceX ® **Raptor 2** engines used onboard *Super Heavy-Starship* launch vehicle. The nominal mission is designed to achieve $v_f = 7.75$ km/s with a **114266 kg** initial mass.

A lightweight **6-crew Orion Crew Exploration Vehicle CM**-derived capsule with **triple-parachute landing system** and rescaled **Launch Abort System** (LAS) provides the required landing accuracy via precision ballistic trajectory control, maintaining high operational flexibility, safety, and TRL compliance. Complete mission analysis, trajectory analysis, aerodynamic characterization, structural sizing with validated structural indices and performance verification confirm full compliance with all assignment requirements.

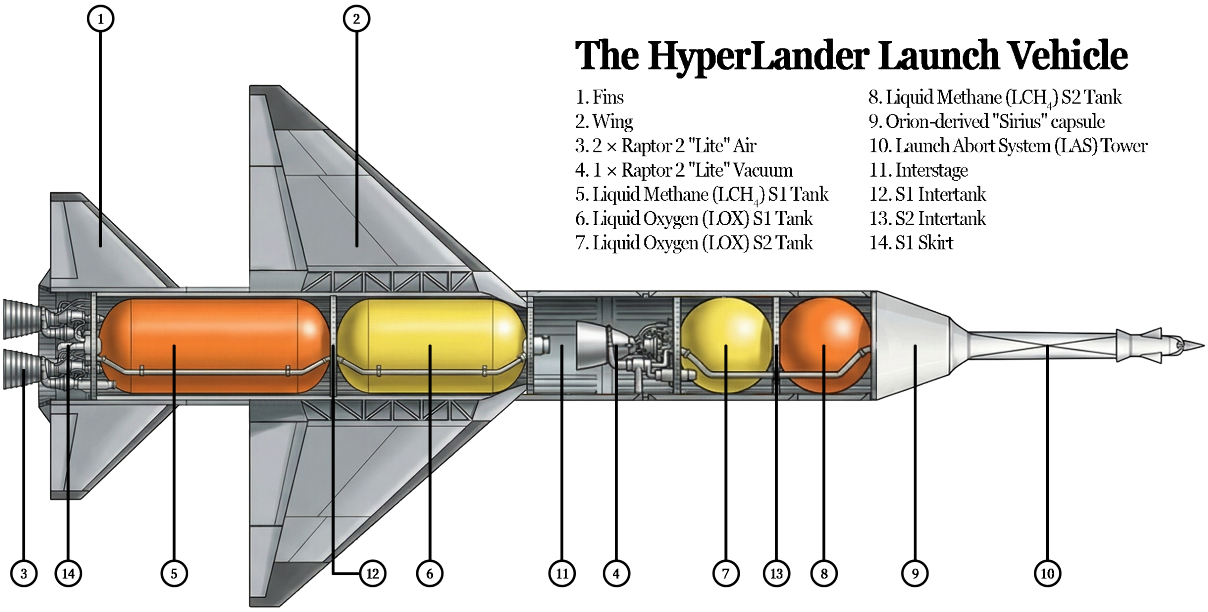

Nomenclature

Symbol	Parameter	Unit
ΔV_{tot}	Total Mission Delta-V	m/s
ΔV_{req}	Required Delta-V	m/s
M_0	Gross Lift-Off Weight	kg
m_{pay}	Payload Mass	kg
$M_{\text{HyperLander}}$	Mass of the designed launcher	kg
$M_{\text{Pegasus XL}}$	Mass of the reference baseline	kg
μ	Mass ratio ($M_{\text{HL}}/M_{\text{Peg}}$)	–
λ	Linear scaling factor	–
T/W	Thrust-to-Weight Ratio	–
Max-Q	Maximum Dynamic Pressure	Pa
LV	Launch Vehicle	–
I_{sp}	Specific Impulse	s
$\dot{m}$	Mass Flow Rate	kg/s
O/F	Oxidizer-to-Fuel Ratio	–
P_c	Chamber Pressure	bar
C_F	Thrust Coefficient	–
FFSC	Full-Flow Staged Combustion	–
$\varepsilon_{\text{nozzle}}$	Expansion Ratio	–
A_t	Throat Area	m^2
A_e	Exit Area	m^2
L_{nozzle}	Nozzle Length	m
ε_s	Structural Ratio	–
m_{dry}	Dry Mass	kg
m_{prop}	Propellant Mass	kg
W/S	Wing Loading	kg/m^2
t/c	Thickness-to-chord ratio	–
N_p	Number of Passengers	–
m_{GLM}	Gross Launch Mass	kg
d	Maximum Outer Diameter	m
V_{press}	Pressurized Volume	m^3
v_{spec}	Specific Volume per Passenger	m^3/pax
η	Cylindrical Packing Efficiency	–
ℓ_{press}	Pressurized Module Length	m
d_{base}	Base Diameter	m
d_{top}	Top Diameter	m
θ	Sidewall Angle	deg
$m_{\text{cap, wet}}$	Capsule Wet Mass	kg
m_{crew}	Crew Mass	kg
m_{cargo}	Cargo Mass	kg
Id^2	Volume Parameter	m^3
$a_{\text{limit}}(t)$	Acceleration Limits	g_0
g_0	Standard Gravitational Acceleration	m/s^2

(continued on next page)

(continued from previous page)

Symbol	**Parameter**	**Unit**
$T(t)$	Thrust Profile	N
T_{max}	Maximum Thrust	N
ψ	Thrust Regression Coefficient	–
t_{burn}	Burn Time	s
$(F/W)_0$	Initial Thrust-to-Weight Ratio	–
ε_{LAS}	LAS Structural Ratio	–
ζ	Propellant Fraction	–
f_{LAS}	Total LAS Mass Fraction	–
m_{LAS}	Total LAS Mass	kg
ρ_{prop}	Propellant Density	kg/m^3
V_{motor}	Motor Volume	m^3
r_{motor}	Motor Radius	m
d_{motor}	Motor Diameter	m
ℓ_{motor}	Motor Length	m
AR	Aspect Ratio	–
λ_{taper}	Taper Ratio	–
Λ	Sweep Angle	deg
C_p	Local pressure coefficient	–
$C_{p,\text{max}}$	Stagnation pressure coefficient	–
C_L	Lift coefficient	–
$C_{L\alpha}$	Lift curve slope	rad^{-1}
C_D	Total Drag coefficient	–
$C_{D,\text{pressure}}$	Pressure (wave) drag coefficient	–
$C_{D,\text{friction}}$	Skin friction drag coefficient	–
$C_{D,\text{base}}$	Base suction drag coefficient	–
$C_{D,\text{mol}}$	Free molecular drag coefficient	–
$C_{D,\text{newton}}$	Continuum Newtonian drag coefficient	–
$C_{\text{D, 0}}$	Parachute drag coefficient	–
C_N	Normal force coefficient	–
$C_{N,\text{body}}$	Corrected body normal force coefficient	–
$C_{\text{d,c}}$	Cross-flow drag coefficient	–
C_f	Average skin friction coefficient	–
F_c, F_{Re}	Van Driest transformation factors	–
η_{cf}	Cross-flow efficiency factor	–
$w(h)$	Sine-squared bridging function	–
S_{ref}	Reference area	m^2
S_{wet}	Wetted surface area	m^2
S_{plan}	Planform area	m^2
S_b	Base cross-sectional area	m^2
X_{LE}	Leading Edge position from nose	m
Λ_{fillet}	Wing-body fillet sweep angle	deg
θ_{local}	Local surface inclination angle	deg
θ_{max}	Shock detachment limit angle	deg
Re_L	Reynolds number based on length	–
Kn	Knudsen number	–
M	Mach Number	–
β	Ballistic Coefficient	kg/m^2

(continued on next page)

(continued from previous page)

Symbol	**Parameter**	**Unit**
L/D	Lift-to-Drag Ratio	–
h, H	Altitude	m
D	Drag	N
L	Lift	N
q	Dynamic Pressure	Pa
θ	Thrust direction/Pitch	deg
α	Angle of Attack	deg
r	Radial distance from Earth's center	m
R_E	Mean Earth radius	m
θ_{inertial}	Inertial longitude angle	rad
v, V	Velocity magnitude	m/s
M	Mach number	–
γ	Flight-path angle	rad
t	Time	s
$g(h)$	Gravitational acceleration	m/s^2
ρ	Atmospheric density	kg/m^3
p	Atmospheric pressure	Pa
T_{atm}	Atmospheric temperature	K
$\dot{q}_{\text{conv}}$	Convective heat flux (stagnation point)	W/m^2
Q	Total integrated heat load	J/m^2
ρ_e	Density at boundary-layer edge	kg/m^3
μ_e	Dynamic viscosity at BL edge	Pa·s
Pr	Prandtl number	–
c_p	Specific heat (const. pressure)	J/(kg·K)
T_{ad}	Adiabatic wall temperature	K
T_w	Wall temperature	K
ε	Surface emissivity	–
σ	Stefan-Boltzmann constant	$\text{W/(m}^2\text{K}^4\text{)}$
R_n	Capsule nose radius	m
L_{TPS}	TPS thickness	m
ρ_{TPS}	TPS material density	kg/m^3
k	TPS thermal conductivity	W/(m·K)
T_{back}	TPS back-face temperature	K
h_{int}	Internal heat-transfer coeff.	$\text{W/(m}^2\text{K)}$
m_{TPS}	Total TPS mass	kg
V_{term}	Terminal descent velocity	m/s
t_{dep}	Parachute deployment time	s
t_f	Parachute filling time	s
b	Inflation exponent	–
h_{drogue}	Drogue deployment altitude	m
h_{main}	Main deployment altitude	m
n, g_{max}	Load factors	–
R_{final}	Achieved downrange	m
R_{target}	Target downrange	m

Contents

List of Figures

List of Tables

Chapter 1

Introduction

The growing Space Economy has enhanced the development of technological solutions, not only to make space more accessible but also to address needs that once would be considered pure fantasy. Suborbital transportation and Space Tourism are among the latter. In the defense sector, tangible interest was manifested with the *RocketCargo* program of U.S. Air Force Research Laboratory, issuing in 2022 a $102 million contract to SpaceX (and later other players) to develop a P2PD system for military equipments [1]. In this context, the *HyperLander* solution aims at fulfilling the requirements of a military crewed P2PD mission while addressing additional needs considered extremely valuable for this specific context. In order to do so, a preliminary concept design for a *first-ever* crewed airborne launcher was developed, capable of reaching an apogee of 200 km with a speed approximating orbital insertion $v_f = 7.75$ km/s. Being this an element of true novelty in the Space Launch sector, during the modeling of each system attention was focused on simplicity and validation of the obtained results, in order to obtain a first solid design guess to be *vertically* investigated in further design iterations. The design process begins with the identification and trade-off analysis of suitable alternatives to accomplish the assigned mission, to later proceed with a multidisciplinary design loop involving *Payload*, *Trajectory*, *Propulsion*, *Layout*, *Aeronautics* analysis that were complemented with *Structures*, *Risk & Reliability* and *Guidance and Control Analysis*.

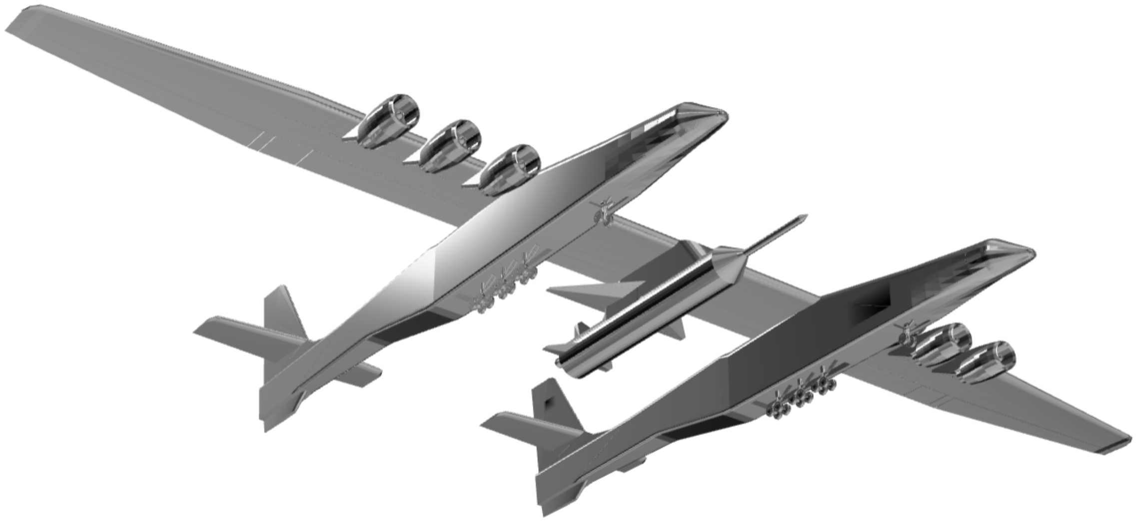

Figure 1.1: HyperLander LV fully integrated with Scaled Composites Stratolaunch "Roc".

Chapter 2

Mission Requirements

This section chapter presents the requirements of the mission the design process addresses. In App. M functional analysis and system's requirements allocation are further deepened.

- **R0**: Design Reference Mission
    - Antipodal trajectory
    - 6 passengers
    - Accuracy of 20 km
- **R1**: LV Design
    - One or more stages
    - Expendable
    - High TRL or AD2 risk rate less than 40%
- **R2**: Re-entry
    - Assume perfect ballistic trajectory
    - 50% success rate
- **R3**: Capsule Design
    - Shape & Size
    - Weight & Center of Mass
    - Parachute
- **R4**: Programmatic Requirements
    - Human spaceflight
    - Ground impact casualty risk $\leq 10^{-4}$
    - Compatibility with launch site
    - Military equipment
- **RM**: Military Requirements
    - Covert Launch
    - Operational readiness
    - Operational Flexibility

RM represents additional requirements, not directly expressed by the customer but considered essential for the nature of the mission. An investigation on Horizontal Launch Vehicles for military use conducted by the DARPA agency [2], highlights greater interests in Programmatic Requirements and Mission Perfomance in defense applications with respect to NASA. More precisely, it was highlighted that the industry would trade a less expensive launcher with a solution meeting the listed requirements, such as an airborne launcher. Here below they are expanded and contextualized in the assigned mission:

- **Covert Launch**: as launchpad activity cannot be hidden from satellites, the mission would be easily traceable. The implications for a crewed mission would make risk in most applications unacceptable as the counterpart might have time to intercept the capsule. Being able to prepare the launch inside a hangar would address this issue.

- **Operational Readiness**: differently from space exploration, military missions are to be considered a tool in a more complex context rather than the context itself, the former being as critical as unpredictable. The mission performance has to be evaluated also on reliability on operational readiness. Whilst a human rated spaceflight constraints propellant choice to cryogenic or semi-cryogenic solutions, time related to fueling would still be an issue, yet an airborne launch would guarantee weather and launch queues issues avoidance.

- **Operational Flexibilty**: as long as the fueling infrastructure is available at ground, an airborne (horizontal) launcher could takeoff from any compliant runaway. Moreover, the carrier could release the launcher from the best locations, both to minimize ground causality risk and to exploit sweeter latitudes. Moreover, if launch is constrained to a specific asset on ground (i.e., launch pad), the latter would become a strategic objective to deprive from launching capability.

Chapter 3

Market Survey & Preliminary analysis

As manned airborne launch has never been performed before, with rare exceptions for high altitude vessels capable of reaching the Kàrman line (X-15[3], SpaceShipTwo[4]) , the proposed design had no existing or historical competitors to begin with. Therefore, at this stage, rather than a baseline selection a preliminary *horizontal* analysis on existing solutions for relevant systems was conducted.

3.1 Launch Vehicle Architectures

With the goal of exploiting the high re-usability, derived from the operational flexibility of horizontal take off launchers, in the last 40 years many attempts were made to develop this technology. In order to address the listed requirements, the investigation started by exploring these concepts well documented in the review [5]. In general, as also concluded in [2], the development of most advanced concepts such as SSTO or hypersonic TSTO are strongly limited by the available propulsion technology. Moreover, hypersonic stage separation carries intrinsic technical challenges, while as stated by the ASTROX investigation, documented in [5], such TSTO architecture would end up being heavier than the largest supersonic aircraft ever built [1]. The DARPA investigation [2], whose figure of merit are aligned with the *HyperLander* mission requirements, concluded that to mitigate risk in development, in a military context where less expensive solutions are willingly traded for more performing ones, a subsonic airborne launcher integrated on existing airframe would find its fit. Inspired by this work, it was chosen as baseline for the *HypeLander* concept. The Pegasus XL was then chosen as baseline to estimate wing contributes both in terms of structures and aerodynamics. Moreover, it resulted being extremely useful in validating obtained results. Yet, both size and propulsion had to be defined resorting to other solutions.

3.2 Compliant Payloads

As illustrated in Tab. 3.1 the preliminary investigation considered the possibility of a gliding capsule as it would reduce the Δv_{design} thanks to a lift to drag ratio grater than 1[6] . Yet, being not required and requiring an investigation beyond the scope of this work, this option was discarded. Starting from the presented data, the capsule was designed considering the lower mission duration with respect to the missions for which the presented options were designed for (Ch. 5).

3.3 Preliminary Trade-off

To identify the Launch Vehicle initial mass M_0, propulsion system, structural mass and evaluate alternatives for the carrier, a trade off analysis was performed based on available data in literature and based on what could be directly deduced from the mission requirements. For the latter, final conditions, payload and release conditions were considered definitive.

---

[1] to bring a ≈4.5 t to LEO

Table 3.1: Comparison of crewed space capsules

Capsule / Vehicle	**Volume (m^3)**	**Crew**	**Type**	**Dry Mass (t)**
Crew Dragon [7]	9.3	7	Ballistic	9.5
Starliner [8]	11	7	Ballistic	13
Orion [9]	9	4–6	Ballistic	26 (full) / 10 (CM)
Soyuz-MS [10]	4	3	Ballistic	$\simeq 3$
New Shepard [11]	15	6	Ballistic	8
Dream Chaser [12]	16	7	Glider	9
X–38 [13]	11.8	7	Glider	10

Final Conditions: to reach the globe's antipode a trajectory reaching an apogee of 200 km with a speed approximating orbital insertion of 7.75 km/s was defined [2]. These choices were made to keep the flight suborbital while maximizing the downrange. In fact, this suborbital orbit has its perigee, by definition antipodal, at 100 km of altitude, at which the flight would be considered atmospheric and thereby setting the re-entry point. More available in the descent section (Ch. 7).

Payload: Payload and LAS weight were estimated as detailed in Ch. 5.

Release conditions: Initially, the Stratolaunch was selected due to its higher payload mass margin and simplified integration. However, the Boeing 747-400 was also evaluated, following [2] recommendations. Release parameters were defined to ensure compatibility with both carriers, specifically adhering to the Stratolaunch flight envelope (Sec. 8.1), which represents the most restrictive case. The $\Delta v_{\text{latitude}}$ contribution is likewise derived from this analysis.

Table 3.2: Δv Budget. Gravity losses are conservatively estimated by scaling reference ground-launch TSTO data [14] by a factor of $\approx \frac{5}{6}$, deriving from the ratio between the current air-launch ignition altitude and the reference Stage 1 burnout altitude. Detailed derivation is provided in Ch. 7.

Negative Contribution	**Value**	**Reference**
Δv_{grav}	13.7%	[14]
Δv_{drag}	322 m/s	[15, 16]
Positive Contribution	**Value**	**Reference**
$\Delta v_{\text{latitude}}$	450 m/s	Sec. 8.1
$\Delta v_{\text{release}}$	170 m/s	Sec. 8.1
h_{release}	11 400 m	Sec. 8.1
$\Delta v_{\text{first stage}}$	40%	[14]
Δv_{design}	$\simeq 8.635$ km/s	–

The trade-off analysis was conducted as shown in Fig. 3.1. $M_0, M_{\text{prop1}}, M_{\text{prop2}}$ were computed for $\varepsilon_{S2} = [0.08, 0.1, 0.12]$ and $\varepsilon_{S1} \in [0.08, 0.15]$, with $I_{sp} \in [330, 400]\ s$. In this early phase, same specific impulse was considered for first and second stage. Given the issues that would result from payload integration with the carrier, and given the provided tight margin for propulsion system design, the Boeing 747-400 option was definitely discarded. Additionally LCH_4 was chosen as propellant, as its characteristic performances would ensure a relatively low M_0 without resorting to LH_2.

3.3.1 Assumptions for Structural Indexes

To assume the structural indexes on which the design loop would be based on, a rough and conservative approach was followed as structure optimization is not objective of this concept design. First, to estimate the impact on the structural weight of the first stage a comparison with the Pegasus' ε_{S1}

---

[2] As detailed in Ch. 7, it was not necessary to match the exact orbital speed (7754.5 m/s) to reach the antipode, nominal value of 7.75 km/s was thereby chosen.

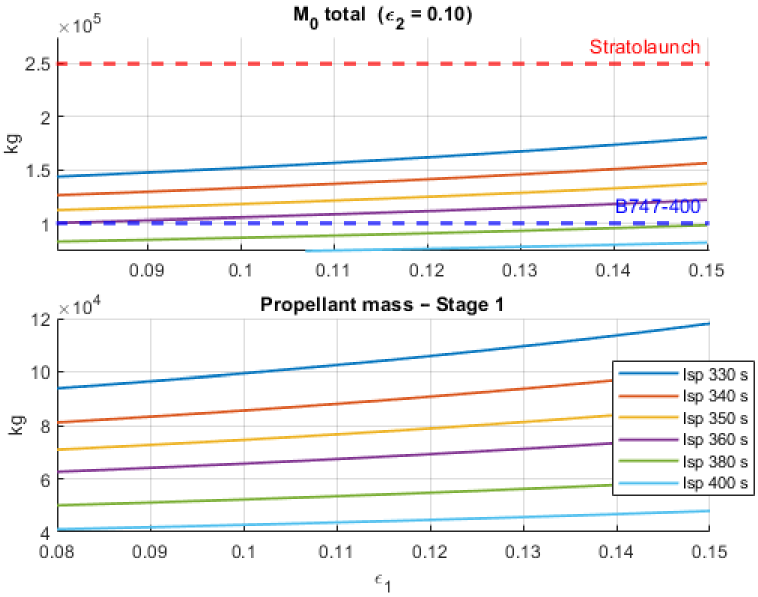

Figure 3.1: Trade-off with ε_{S2} fixed at 0.1.

computed from [17] was made with the data available in [18]. It was deduced that the Pegasus' first stage had a structural index $\simeq 40\%$ grater than a high performance solid propellant stage. Moreover, from the analysis in [19][3] and the propellant mass provided from the trade-off analysis as shown in Fig. 3.1, it was possible to estimate what would be the stages' structural index based on the propellant mass. This method was validated with Starship's structural index deduced from [20], that was predicted with an error of $\approx 10\%$. Moving on, the previously deduced *wing-factor* was applied on the first stage. Then, for both stages a conservative factor of safety was applied to take into account non optimality, simplifications made in the tradeoff analysis, epistemic uncertainties at this level of design and on the data considered. Result were then rounded by excess.

	Estimated from [18],[19]	**Wing F-S factor**	**Safety factor**	**Resulting coefficients**
ε_{S1}	$\simeq 0.0698$	1.4	1.3	$\simeq 0.13$
ε_{S2}	$\simeq 0.0766$	0	1.3	$\simeq 0.10$

Table 3.3: Structural mass fractions and resulting coefficients

An exhaustive description of the procedure is available in App. A.

---

[3] The analysis provides relation between propellant mass and structural index (considering the entire dry mass), with optimization tools and empirical corrections

Chapter 4

Goals in Design & Design Loop

The lack of historical competitors and intrinsic challenges of the proposed system make this work truly pioneering; thereby, many answers to questions arised during the design process couldn't be answered if not by vertically investigating the matter. Such investigations wouldn't be justified without a solid first design that at least ensures a margin of feasibility of the overall design. The design goal of the present work is to navigate through uncertainty with simple, conservative and, where possible, validated choices, especially in the most critical design areas, to provide the above mentioned design precursor together with lessons learnt and to be applied in further iterations. This section provides an overview on the design workflow and the final results of the design.

4.1 Design Areas

A representation of the design areas involved in the design process is represented in Fig. 4.1; disciplines and systems are here grouped in macro areas and relations between them highlighted.

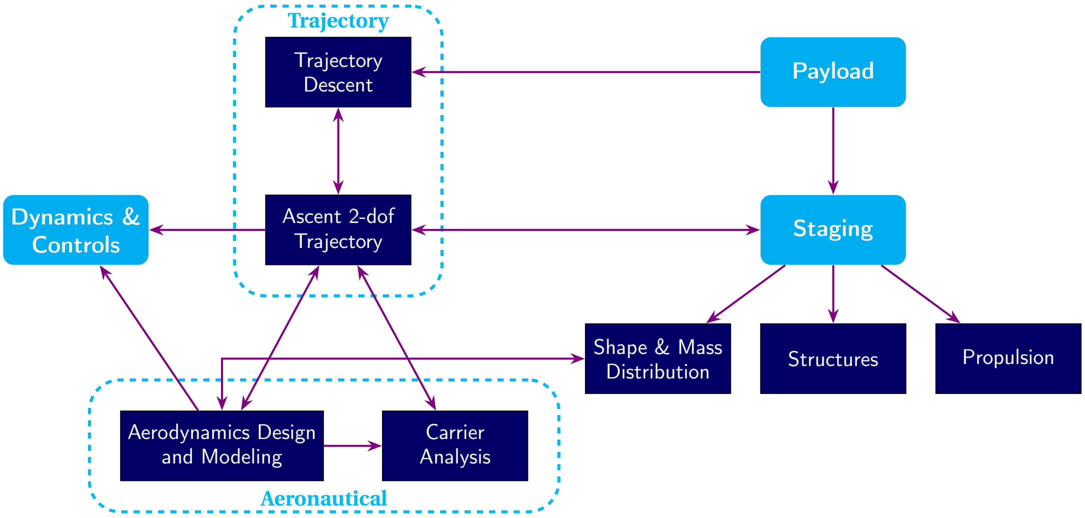

Figure 4.1: Design areas and discipline coupling.

4.2 Design Process

In compliance with the goal and philosophy of this concept design, the design process was divided into two stages: a **Core Design Loop**, involving limited systems and a downstream **Design Verification**, involving the remaining. Obviously starting from the preliminary analysis in Ch. 3.

The **Core Design Loop** involved *Ascent Trajectory Analysis*, *Propulsion System Analysis*, *Layout & Mass Distribution Analysis* and *Aerodynamic modeling*.

Before beginning, $I_{\mathrm{sp},\,1}$, $I_{\mathrm{sp},\,2}$ were provided based on the choice of propellant and with appropriate modeling as described in Ch. 6. Then, starting from the data deducible directly from the requirements and the guesses for structural indexes (as discussed in Ch. 3), a layout and mass distribution was guessed based on the most recent $\Delta v_{\mathrm{design}}$ guess. This would provide the necessary data to model aerodynamics. Successively an overshoot on the $\Delta v_{\mathrm{design}}$ was performed, overestimating the losses, and layout recomputed. Then, an inner loop with ascent optimization on first and second stage burning times would begin, and at each iteration realistic losses were computed; therefore, the layout would be updated. The inner loop would be finished when a feasible configuration with compliant M_0 was found. On this layout, new aerodynamic data would be provided and final adjustments on initial T/W were performed by observing new outputs from ascent optimization (e.g. g-loads). The losses overshoot at the inner loop initiation resulted necessary to help convergence on feasible solutions, that were updated by hand at each iteration.

Once full compliance was obtained, optimal staging was applied on the resulting Δv_{design}; then, layout and aerodynamics were updated and a final trajectory was produced. Interestingly, the energy partition obtained from the inner loop gave results similar to optimal staging for the same Δv_{design}, making this last step the softer. Anytime a change in modeling in any of the involved disciplines (or worse, in the ones considered as boundary conditions) was performed, this process had to start from what was considered the latest valid step.

The downstream **Design Verification** involved *Descent Trajectory Analysis*, *Structural Analysis*, *GNC Analysis* and *Risk & Reliability Analysis* and was focused on assessing whether the obtained results were compliant with system's and mission's requirements,

4.3 Results

Table 4.1: Mission Mass, Propulsion, and Performance Summary of the LV Stages

Parameter	**Stage 1 (Booster)**	**Stage 2 (Upper Stage)**
Gross mass at ignition	$m_{0,1} = 114\,266\,\text{kg}$ [a]	$m_{0,2} = 29\,725\,\text{kg}$ [b]
Propellant mass	$m_{\text{prop},1} = 72\,554\,\text{kg}$	$m_{\text{prop},2} = 22\,691\,\text{kg}$
Dry mass (structures)	$m_{\text{dry},1} = 10\,841\,\text{kg}$	$m_{\text{dry},2} = 2521\,\text{kg}$
Structural Ratio	$\varepsilon_1 = 0.13$	$\varepsilon_2 = 0.10$
Propulsion system	2 × Raptor 2 "Lite" Air	1 × Raptor 2 "Lite" Vacuum
Thrust (stage total)	$F_{1,11.4\,\text{km}} = 2353.2\,\text{kN}$ [c]	$F_{2,\text{vac}} = 379.0\,\text{kN}$
Specific impulse	$I_{\text{sp},1} = 343.17\,\text{s}$ [c]	$I_{\text{sp},2} = 368.50\,\text{s}$
ΔV capability	$\Delta V_1 = 3391.44\,\text{m}\,\text{s}^{-1}$	$\Delta V_2 = 5208.56\,\text{m}\,\text{s}^{-1}$
Thrust-to-weight ratio at ignition	$(T/W)_1 \approx 2.10$	$(T/W)_2 \approx 1.30$

[a] Launch vehicle only, evaluated at Stage 1 ignition.

[b] Upper stage plus capsule at Stage 2 ignition; Launch Abort System already jettisoned.

[c] Evaluated at air-launch conditions ($\approx 11.4\,\text{km}$ altitude); $g_0 = 9.806\,65\,\text{m}\,\text{s}^{-2}$.

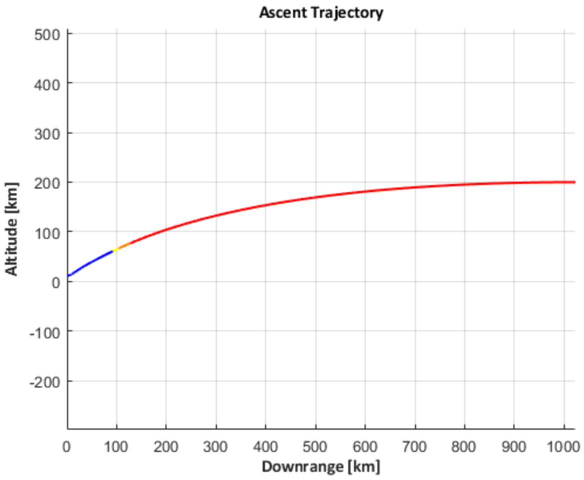

Figure 4.2: Nominal ascent trajectory. First stage in blue, stage separation in yellow, second stage ignition in orange and second stage in red.

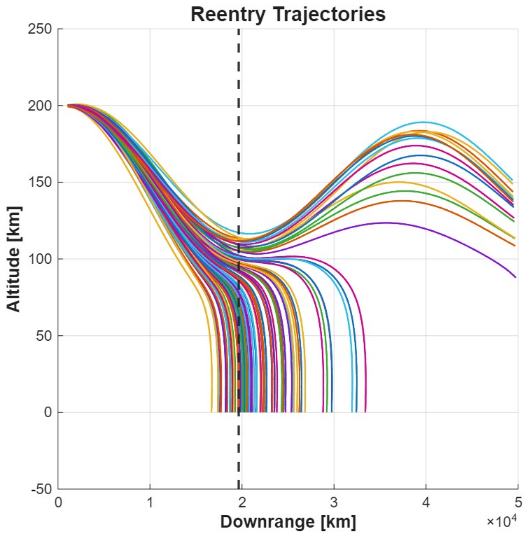

Figure 4.3: Reentry propagation given uncertainty in ascent trajectory. Vertical line defines target landing point. Trajectories exceeding target are assumed to be controlled leading to a 62% success rate (see Ch. 10).

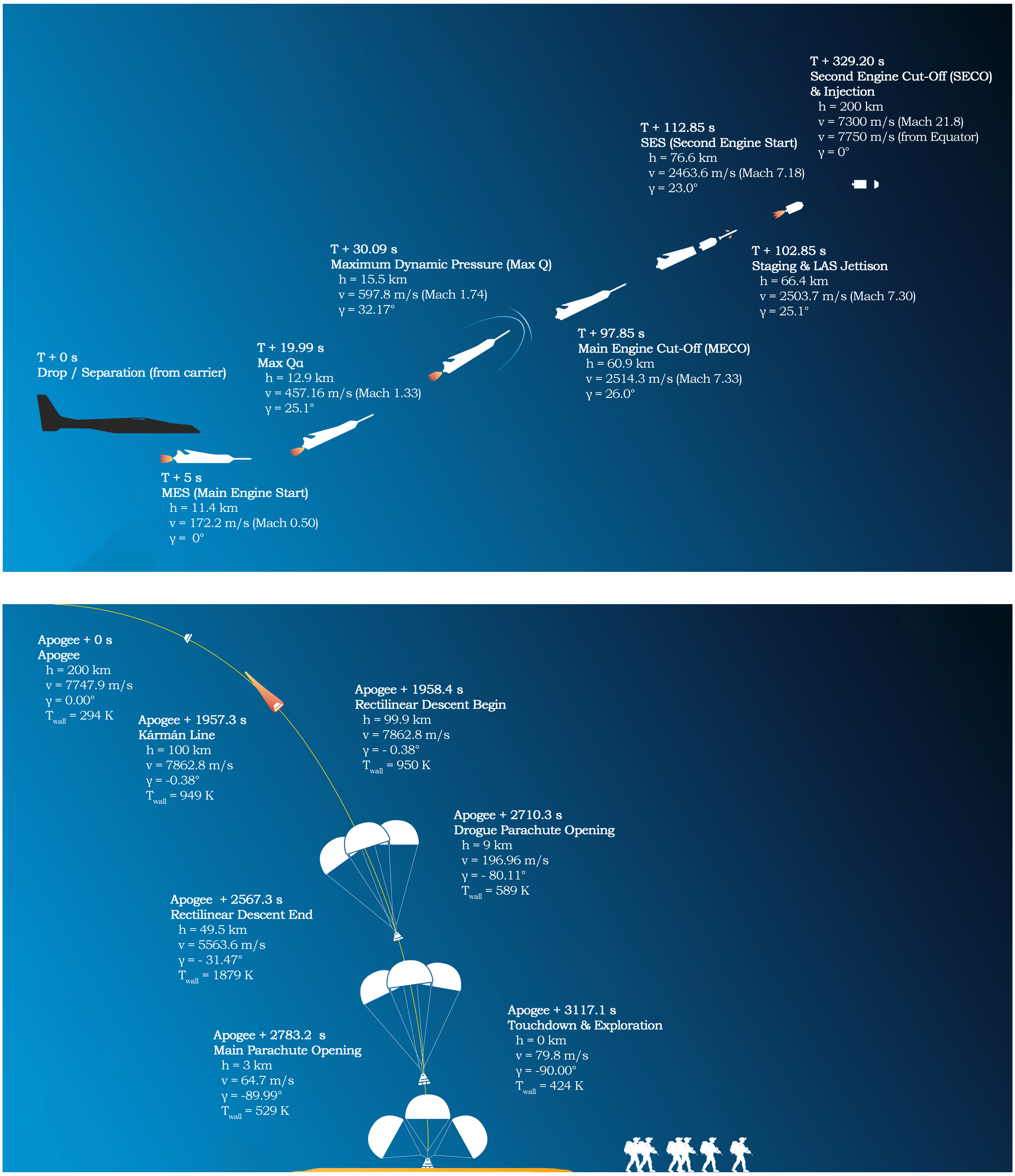

Figure 4.4: Key Points of the Ascent Phase and Landing Sequence.

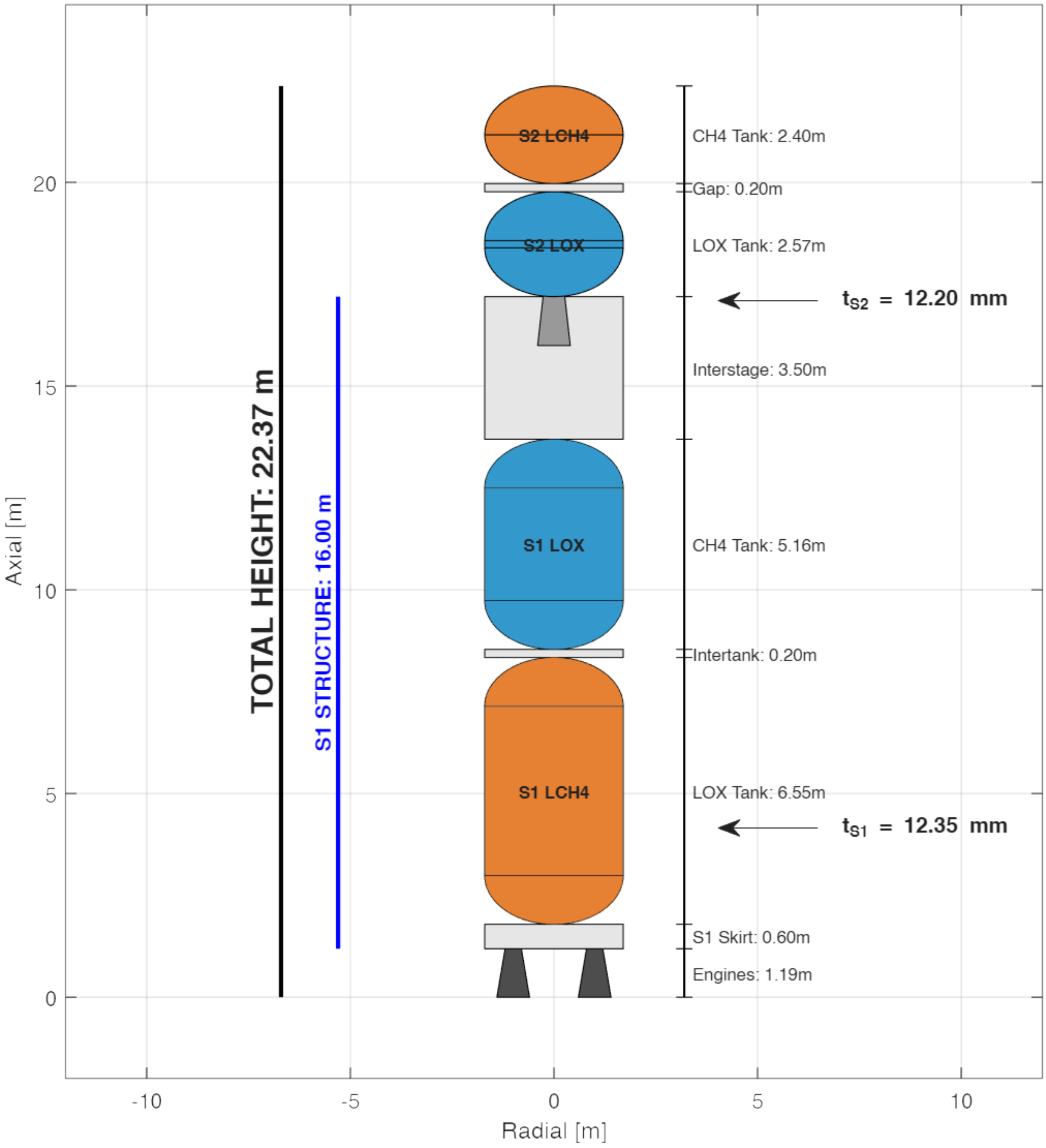

Figure 4.5: Final configuration blueprint of the HyperLander vehicle. The layout illustrates the internal arrangement of LOX and LCH_4 tanks, the interstage section, and the integrated structural dimensions derived from the reverse-sizing methodology.

Chapter 5

Payload

5.1 Payload Design Goal: The "Sirius" Capsule

The primary objective of the payload subsystem is to dimension a crewed spacecraft capable of accommodating six passengers ($N_p = 6$) for a "quasi-LEO taxi" mission profile with a duration of less than 24 hours. The design is constrained by the operational limitations of the Stratolaunch air-launch platform and human-rating requirements, that are defined as follows:

- **Gross Launch Mass (GLM):** The total mass of the capsule including the Launch Abort System (LAS) must satisfy $m_{\text{GLM}} \leq 6$ t to keep the rocket lift-off mass the lowest (see Ch. 8);
- **Geometric Constraints:** The maximum outer diameter is limited to $d \leq 3.8\,\text{m}$ to remain compatible with a Pegasus XL-class fairing envelope [21];
- **Safety Standards:** The system must feature an integral Launch Abort System compliant with NASA-STD-3001 requirements [22];
- **Human Factors:** Acceleration loads during abort scenarios must not exceed $8g$ for sustained duration ($t \leq 6\,\text{s}$), with peak emergency loads limited to $12g$ for $t \leq 0.5\,\text{s}$ [22, 23].

The chosen baseline is the 6-crew configuration of the Orion *Crew Exploration Vehicle* from NASA's *Exploration Systems Architecture Study* (ESAS) [9]. The spacecraft is designated *Sirius*, inspired by the brightest star in the night sky and the faithful companion of Orion in Greek mythology.

5.2 Habitable Volume Analysis & Structural Mass Estimation

5.2.1 Volumetric Sizing Strategy

The pressurized volume V_{press} is determined through analysis of historical specific volumes (v_{spec}) for comparable crewed spacecraft. While the Orion CEV offers a spacious $3.25\,\text{m}^3/\text{pax}$ for extended missions [9], and the Soyuz TMA provides a constrained $1.33\,\text{m}^3/\text{pax}$ [10], the short mission duration permits an intermediate optimization (see App. B for further details).

The selected specific volume represents a 24% improvement over Soyuz for allowing backpacks stowage while maintaining reasonable structural efficiency. The total pressurized volume is:

$$V_{\text{press}} = N_p \cdot v_{\text{spec}} = 6 \times 1.65 = 9.9\,\text{m}^3 \tag{5.1}$$

Suitable for this kind of space mission, according to [24].

5.2.2 Geometric Configuration

The geometric sizing utilizes Sforza's empirical correlations [24]. Assuming a cylindrical packing efficiency factor $\eta = 0.45$ (representative of truncated cone geometries) and fixing the base diameter $d = 3.4\,\text{m}$ ($< 3.8\,\text{m}$ requirement), the volume parameter and the pressurized module length are:

$$\text{Id}^2 = \frac{V_{\text{press}}}{\eta} = \frac{9.9}{0.45} = 22.0\,\text{m}^3 \quad \Longrightarrow \quad \ell_{\text{press}} = \frac{\text{Id}^2}{d^2} = \frac{22.0}{(3.4)^2} \approx 1.90\,\text{m} \tag{5.2}$$

The external geometry employs a truncated cone configuration with sidewall angle $\theta \approx 30°$ (derived from Apollo/Orion heritage) [9], resulting in a top diameter ≈ 1.20 m.

5.2.3 Structural Mass Estimation

The dry mass m_{dry} is estimated using Sforza’s correlation (Eq. 10.1, [24]), modified with a factor of 0.84865 interpolated from the latest designs [7–13] to account for recent advancements [24]:

$$m_{\text{dry}} = 470 \times 0.84865 \times (\text{Id}^2)^{2/3} \approx 3132\,\text{kg} \tag{5.3}$$

The wet mass ($m_{\text{cap, wet}}$) includes crew and consumables, as stated in Tab. 5.1.

Table 5.1: Sirius Mass Budget (starting from Crewed ISS CEV CM’s [Table 5-4, [9]])

Component	**Mass [kg]**	**% of Dry Mass**	**Notes**
Structure	720	23%	Primary structure, pressure vessel, micrometeoroid/debris shielding.
Protection	99.4	3.2%	Thermal protection system (TPS) (see App. C).
Propulsion	157	5%	Reaction Control System (RCS, thrusters + tanks).
Power & Control	313	10%	Batteries, power management, flight software, guidance algorithms.
Avionics	350	11.2%	Computers, communication systems, sensors, cabling [14], including Stage 2’s (See Ch. 6).
Environment	438	14%	Life support systems (ECLSS), air revitalization, water/waste management.
Parachutes	310.2	9.9%	Main and backup parachutes (see App. F).
Other & Growth	744.4	23.7%	Interior outfitting, seats, displays, lighting, stowage, parachute opening system.
Dry Mass (Total)	**3 132**	**100%**	Total capsule dry mass.
Crew mass	$6 \times 140\,\text{kg}$		Full Launch Entry Suits (LES) add 42.6 kg per crew member (29 kg for personal parachute and survival systems) [25].
Consumables (Cargo)	$3 \times 180\,\text{kg}$		Backpacks for 72h-exploration mission.
Capsule Wet Mass	**4 512**		$m_{\text{cap, wet}} = m_{\text{dry}} + m_{\text{crew}} + m_{\text{cargo}}$, similar to Soyuz-TMA DM [10].

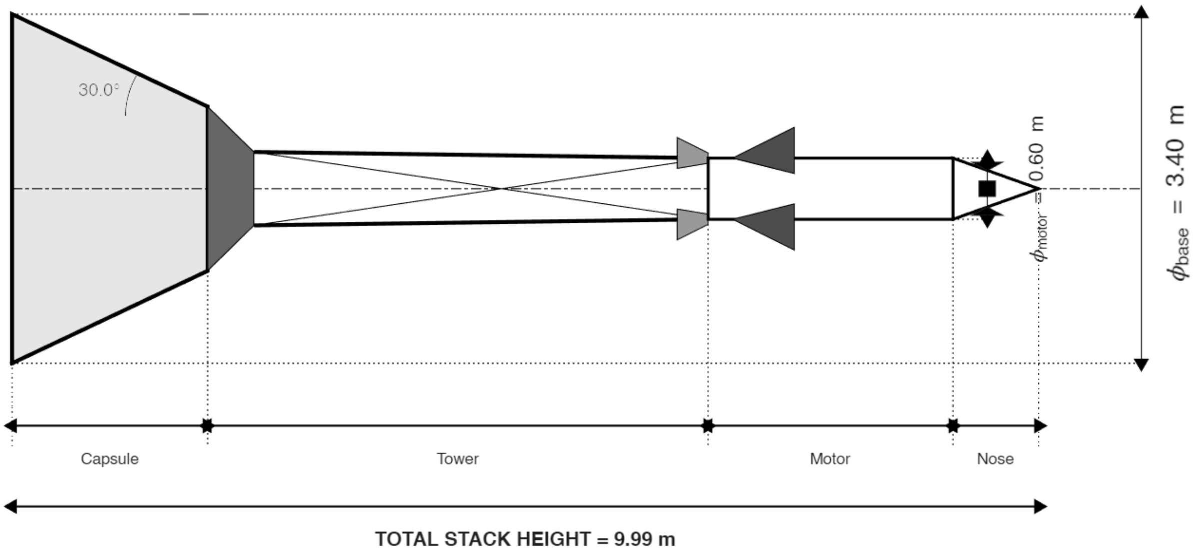

Figure 5.1: Scaled technical drawing of Sirius spacecraft generated by the sizing algorithm, showing capsule, tower, and abort motor integration (AR = 4.0).

5.3 Launch Abort System (LAS) Design

5.3.1 Propulsion System Architecture

The Sirius LAS is designed with $a_{\max} \leq 8\,g_0$ for worst-case scenarios. To meet acceleration constraints while ensuring adequate separation, the LAS solid rocket motor employs a *regressive grain profile*. The thrust profile decreases linearly to prevent excessive g-loads as propellant depletes:

$$T(t) = T_{\max}\left(1 - \psi\frac{t}{t_{\text{burn}}}\right) \quad \text{for } 0 \leq t \leq t_{\text{burn}} \tag{5.4}$$

where $T_{\max} = \text{GLM} \times (F/W)_0 \times g_0$. The numerically optimized LAS sizing parameters are in Tab. 5.2.

Table 5.2: LAS Sizing Parameters

Parameter	Value	Notes
Initial Thrust-to-Weight	$(F/W)_0 = 7.5$	Sea-level thrust
Burn time	$t_{\text{burn}} = 6.0\,\text{s}$	From NASA-STD-3001
Specific impulse	$I_{\text{sp}} = 249\,\text{s}$	Standard HTPB solid propellant
Structural ratio	$\varepsilon_{\text{LAS}} = 0.12$	Advanced carbon-composite casing
Thrust regression	$\psi = 0.20$	From NASA MLAS [26]

5.3.2 Mass Budget Closure

The Gross Launch Mass (GLM) is the sum of wet capsule mass and LAS mass. Using Sforza's methodology (Eq. 11.27 from [24]), the propellant fraction ζ is:

$$\zeta = \frac{(F/W)_0 \times t_{\text{burn}}}{I_{\text{sp}}} = \frac{7.5 \times 6.0}{249} = 0.181 \tag{5.5}$$

Solving for mass closure from the total LAS mass fraction (including structure) gives:

$$f_{\text{LAS}} = \zeta(1 + \varepsilon_{\text{LAS}}) = 0.181 \times 1.12 = 0.203 \quad \Longrightarrow \quad \text{GLM} = \frac{m_{\text{wet}}}{1 - f_{\text{LAS}}} = \frac{4\,512}{1 - 0.203} = 5657\,\text{kg} \tag{5.6}$$

Table 5.3: Sirius Final Mass Configuration

Component	Mass [kg]	Fraction [%]
Capsule wet mass ($m_{\text{cap, wet}}$)	4 512	79.8
LAS total mass (m_{LAS})	1 145	20.2
– Propellant	1 022	18.1
– Structure	123	2.2
Gross Launch Mass (GLM)	**5 657**	**100.0**

5.3.3 Performance Summary

Due to the unique dynamics of the carrier, LAS performance was validated in two cases:

- **Pad abort:** Peak velocity = $184.5\,\text{m}\,\text{s}^{-1}$ (Mach 0.54), altitude gain = 1182.2 m @ $t = 10\,\text{s}$
- **Airborne abort:** Peak velocity = $379.3\,\text{m}\,\text{s}^{-1}$, benefiting from $v_0 = 172.2\,\text{m}\,\text{s}^{-1}$ initial condition
- **Ballistic coefficient:** $\beta = 3.07\,\text{kPa}$ (favorable for controlled descent)

For the full LAS motor dimensions, structural integration and aerodynamics and dynamic and kinematic simulation results see App. B.

Chapter 6

Propulsion, Staging & Structures

6.1 Introduction & Methodological Framework

This chapter presents the integrated design workflow for the propulsion system, stage configuration, and primary structure of the HyperLander air-launched launch vehicle. The process follows a sequential, requirement-driven methodology:

1. **Mission Requirements & Mission-Driven Mass Allocation** – Trajectory analysis (Chapter 7) defines the total $\Delta V = 8600\,\mathrm{m/s} = 3391.44\,\mathrm{m/s}$ (S1) $+ 5208.56\,\mathrm{m/s}$ (S2), initial thrust-to-weight ratios ($T/W_1 = 2.10$, $T/W_2 = 1.30$) and the maximum allowable dry mass for each stage;
2. **Propellant & Cycle Selection** – Leading to LOX/LCH_4 and Full-Flow Staged Combustion;
3. **Engine Geometric Scaling & Thermodynamic Nozzle Design** – Raptor 2 engines are scaled to meet T/W requirements and nozzle geometries are optimized using NASA CEA and standard equations for propulsion systems (App. D, Sec. 1);
4. **Stage Mass & Geometry Sizing** – Inverse Tsiolkovsky equation determines propellant masses and tank dimensions (App. D, Sec. 2);
5. **Top-Down Thickness Derivation** – With the chosen structural indices [14], structural mass is distributed across the vehicle's surface area to determine a uniform equivalent thickness;
6. **Multi-Mode Verification** – Derived thickness is rigorously verified against yield, buckling, and shear failure modes with human-rated safety factors (SF = 1.4) [27] (App.es C & E).

The underlying calculations are implemented in a modular toolchain, performing: 1. Engine Scaling & Performance Simulation; 2. Combustion Thermodynamics and Nozzle Design (for Stage 1 and Stage 2); 3. Mass & Geometry Sizing; 4. Structural Verification.

6.2 Propulsion

The propulsion system has four primary roles:

- Provide the total mission ΔV required to reach the required altitude from launch conditions;
- Maintain the required thrust-to-weight ratios for controllability, trajectory shaping, and for keeping high human-rating standards from the carrier release conditions;
- Support the overall system objective of high mission feasibility, not only pure performance.

6.2.1 Propellant & Propulsion Cycle Trade-Off Analysis

A structured propulsion trade-off was conducted at system level, evaluating multiple dimensions simultaneously. Three cryogenic propellant combinations were compared (Tab. 6.1), and LOX/LCH_4 was selected as the optimal compromise between I_{sp}, tank-volume compatibility with the carrier, clean combustion, and future technological developments.

A known drawback of this choice is its fully cryogenic nature, which introduces constraints related to propellant handling, conditioning, and fueling time, with potential implications for mission scheduling and responsiveness. However, as discussed in Section 2, the present system architecture prioritizes overall mission readiness and integration with the air-launch operational concept. Within this context, the benefits provided by the selected propellant combination are considered to outweigh the disadvantages associated with cryogenic fueling, which are therefore not treated as primary drivers in the present analysis.

Table 6.1: Propellant Trade-Off Summary [14, 24, 28, 29]

	LOX/LH$_2$	**LOX/RP-1**	**LOX/LCH$_4$**
Vacuum I_{sp} (s)	440–450	300–320	330–380
Density (kg/m^3, equiv.)	Very low	High	Medium
Tank Volume Impact	Very high	Low	Moderate
Operational Complexity	Very high	Moderate	Moderate–Low

Three propulsion cycles were qualitatively compared (Gas-Generator, Expander, and Full Flow Staged Combustion), since the whole LV was sized keeping in mind configurations starting from Merlin 1D+ (RP-1/LOX, GG) [30], BE-3U (LH$_2$/LOX, Expander) [31] and Prometheus (RP-1/LOX, GG) [32]. Full-Flow Staged Combustion (FFSC) was kept as the reference architecture, inherited from the Raptor family, because it maximizes chamber pressure without thermal over-stressing, yields higher I_{sp} at given nozzle dimensions, and scales favorably in thrust while maintaining efficiency without lowering the TRL due to introduction to major modifications to the original engine.

6.2.2 Propulsion Architecture

The HyperLander launcher employs a two-stage LOX/LCH$_4$ propulsion architecture, with both stages powered by Raptor-class engines derived from SpaceX's Raptor 2. The engines used are not full-scale Raptor 2 units; a geometric scaling process was applied to Raptor 2 Sea-Level (SL) and Vacuum (Vac) data to obtain "Lite" engines with thrust levels adapted to the air-launched mass range and to the mission T/W requirements. The main stage-level propulsion parameters are synthesized, together with other parameters, in Tab. 4.1.

6.2.3 Engine Scaling, Nozzle Design & Technology Readiness and Feasibility

The scaling factor λ for each engine is determined from the required thrust and reference thrust:

$$\lambda = \frac{F_{\text{req}}}{F_{\text{ref}}} \tag{6.1}$$

where F_{req} is the thrust required to meet the target T/W ratio at stage ignition, and F_{ref} is the reference thrust of the baseline Raptor 2 engine (Sea-Level or Vacuum). For this reason:

$$F_{\text{req,S1}} = \left(\frac{T}{W}\right)_{\text{S1}} \cdot m_{0,1} \cdot g_0 \qquad F_{\text{req,S2}} = \left(\frac{T}{W}\right)_{\text{S2}} \cdot m_{0,2} \cdot g_0 \tag{6.2}$$

The nozzle geometries were obtained via an iterative combination of geometric scaling and thermodynamic design using NASA CEA, ensuring that the scaled engines are physically consistent with the expected chamber conditions and optimized expansion ratios from original Raptor's datasheet [33]. The thermodynamic design validates the geometric scaling: the comparison between purely geometric scaling and CEA-based sizing shows thrust discrepancies smaller than 0.1% and exit diameter differences of only a few millimeters, confirming the consistency of the Raptor "Lite".

The geometric and performance characteristics of the scaled engines are summarized in Tab. 6.2, and the detailed thermodynamic equations are provided in App. D, Sec. 1.

Table 6.2: Geometric and performance characteristics of the Raptor 2 Lite rocket engines

Parameter	**Raptor 2 "Lite" Air (S1)**	**Raptor 2 "Lite" Vacuum (S2)**	**Reference**
Vacuum Thrust	1191.1 kN	379.00 kN	Rescaling
Throat Radius	$R_{t,1} = 0.0819\,\text{m}$	$R_{t,2} = 0.0455\,\text{m}$	Rescaling
Exit Radius	$R_{e,1} = 0.4631\,\text{m}$	$R_{e,2} = 0.4546\,\text{m}$	Rescaling
Expansion Ratio	$\varepsilon_1 = 32$	$\varepsilon_2 = 100$	[33]
Nozzle Length (Parabolic)	$L_1 = 1.1869\,\text{m}$	$L_2 = 1.2161\,\text{m}$	Rescaling
Thrust Coefficient	$C_{F,1} = 1.8628$	$C_{F,2} = 1.9455$	Rescaling
Engine Dry Mass	859 kg	273 kg	Rescaling
Scaling Factors (Vacuum)	$\lambda_{1,\,\text{vac}} = 0.5270$	$\lambda_{2,\,\text{vac}} = 0.1599$	Rescaling

A remarkable fact is that the propulsion is validated not only by performance, but by its Technology Readiness Level (TRL) and feasibility. The reference engine family, the Raptor 2, has demonstrated thrust class > 2000 kN and chamber pressures > 300 bar, and is part of an operational LOX/LCH$_4$ infrastructure already in existence. According to NASA's guidelines [34], this base architecture is considered to have **TRL 8–9**. In the geometric rescaling process, which led to lower lower thermal loads, no new materials or combustion regimes were introduced, so a **TRL 6–7** is estimated.

6.3 Staging

The staging is driven by the mission ΔV requirement ($8600\,\text{m}\,\text{s}^{-1}$) and the selected propulsion. The ΔV is split between the two stages as $\Delta V_1 \approx 3391\,\text{m}\,\text{s}^{-1}$ (Stage 1) and $\Delta V_2 \approx 5209\,\text{m}\,\text{s}^{-1}$ (Stage 2). Using the inverse Tsiolkovsky equation (App. D, Sec. 2), the resulting stage masses are computed (See Tab. 4.1). The payload for Stage 1 is the total mass of Stage 2 plus the LAS; the LAS is jettisoned at staging, so Stage 2 ignites with only the capsule as payload.

The tank volumes are calculated from m_{prop}, MR, and $\rho_{\text{LOX, LCH}_4}$, including a 5% ullage factor for isotensoid domes with a $\sqrt{2}:1$ elliptical ratio (App. D). This geometry equalizes hoop stresses between cylinders and domes, enabling uniform wall thickness and removing stress concentrations.

The overall vehicle geometry is constrained by carrier-aircraft compatibility (maximum diameter of 3.40 m) and aerodynamic stability (length-to-diameter ratio of 4.7). The final tank lengths and overall vehicle dimensions yield a total vehicle length of 23.38 m and a slenderness ratio $L/D \approx 6.9$.

6.4 Structures

6.4.1 Design Philosophy & Methodological Framework

Being exposed to significant bending moments during the critical pull-up maneuver (App. E), the structural design of air-launched LVs presents unique challenges distinct from conventional ground-launched systems, which are primarily optimized for axial compression. Traditional structural sizing employs iterative loops that guess thicknesses and verify mass constraints—an inefficient approach for air-launched vehicles where mass constraints are paramount. In line with the design goals, this work develops a *reverse-sizing methodology* that starting from the mass budget computes the available shell thickness, computes the stresses deriving from the load analysis and finally verifies if structures can withstand the latter in the most critical conditions.

With the assumptions made in Ch. 7, 2-DOF flight data was projected onto a 3-DOF model to perform the load and structural analysis. This analysis was performed only on Stage 1 as discussed later in this section. In line with these assumptions, control surfaces are assumed to set the center of pressure position (neglecting the alteration in aerodynamic forces resultants), in order to obtain the dynamic equilibrium a real vessel would have with the rotation imposed in the 2-DOF model.

Regarding the distributions of loads, the following additional assumptions were made, leading to the result in Fig. E.6. First, being the wing the main lifting body and the center of pressure originally close to its longitudinal position, the normal-resultant force was concentrated in the position of the C_p. Second, axial-resultant was uniformly distributed along the vehicle. Third, although the interstage's cylindrical shell is considered to be thick as the first stage, its contribute to the position of the center of mass was neglected, having no propellant within. Finally, the rocket was modeled as a beam with concentrated masses (and moments of inertia) in the Stage 1, Stage 2, Sirius capsule, and LAS. Here, axial, normal and angular accelerations were applied to evaluate the inertial contribute to the internal actions, solving for equilibrium. Therefore, stresses were computed as acting on a cylindrical shell whose thickness includes tank and outer shell derived from the available structural mass as detailed in App. E.

As detailed in App. E, several load conditions were considered: 1. *Max-Q*; *Max-Qα*; 2. *Maximum Axial Acceleration*; 3. *Maximum Angular Acceleration*; 4.*Loaded Transportation*. Also, for the most bending-critical condition (Max Qα), a conservative wind contribute [1] was applied in an additional load analysis [14].

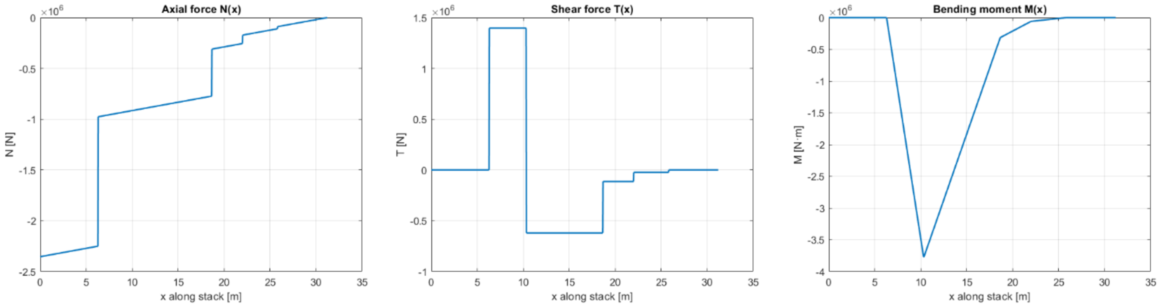

Figure 6.1: From left to right, Axial, Shear, & Moment Internal Actions - Max Qα + Wind Gust

To simplify this preliminary analysis, Stage 1 employs an *integrated monocoque architecture* where the interstage is not a separate bolted assembly but an extension of the propellant-tank cylinder. This eliminates redundant structural elements and enhances load-path continuity, contributing approximately 15% mass savings compared to traditional bolted designs.

6.4.2 Load Cases & Verification Approach

The structural verification utilizes the absolute worst-case loading conditions extracted from the flight envelope. While the **Max ϑ acceleration** represents a critical state for the Thrust Vector Control (TVC) authority and dynamic stability, the **Max $Q\alpha$ + Wind** condition is the **structural design driver**. This case generates the peak aerodynamic bending moments and shear forces that govern the shell thickness required to prevent elastic buckling. Due to this, verification is performed against the following envelope maximums (more details in Tab. E.1 & 6.3). The structural geometry was reconstructed to match the ΔV-based staging calculations, yielding dimensions in Fig. 4.5.

6.4.3 Thickness Derivation & Material Selection

The equivalent uniform shell thickness is derived from the available structural mass using:

$$t = \frac{M_{\text{shell}}}{\rho_{\text{Al-Li}} \cdot A_{\text{total}} \cdot k_{\text{smear}}} \qquad \text{(see App. E)} \tag{6.3}$$

Yelding the results contained in Tab. 6.5. Please note that the chosen material, Al-Li 2195, was

---

[1] 76 m/s, maximum intensity of gust at the *Max-Qα* altitude ≈ 40 kft[14]

Table 6.3: Final Maximum Values from Loads Analysis adopted in Structural Design

Load Type	Value	Source
Bending Moment	5.63×10^6 Nm	Max $Q\alpha$ + Wind
Shear Force	1.40×10^6 N	Max $Q\alpha$ + Wind
Axial Compression	2.35×10^6 N	Max Q
Operating tank pressure	320 kPa	[35]

selected for its cryogenic compatibility with liquid methane, high strength-to-weight ratio, and proven performance in aerospace applications (see App. C for further details).

6.4.4 Verification Results & Safety Margins

The derived thickness was verified against yield, buckling, and shear failure modes using analytical models leading to the final Stage 1 stresses and safety factors, as detailed in App. E.

Table 6.4: Structural Verification Results: Stress Analysis and Safety Margins (Stage 1)

Failure Mode	**Applied Stress** [MPa]	**Critical Stress** [MPa]	**Safety Factor**	**Status**
Axial Compression (Buckling)	$\sigma_{\text{comp}} = 46.00$	$\sigma_{\text{cr}} = 122.60$	2.67	**PASS**
Axial Tension (Yielding)	$\sigma_{\text{tens}} = 54.40$	$\sigma_{y,\text{allow}} = 400.00$	7.35	**PASS**
Torsional/Shear Buckling	$\tau = 21.22$	$\tau_{\text{cr}} = 128.47$	6.05	**PASS**

Tab. 6.4 shows that all failure modes exhibit substantial safety margins exceeding NASA-STD-5001 requirements. Being Stage 1 the most stressed, as shown in Fig. 6.1 and derived Stage 2 thickness only slightly lower (12.35 mm for S1, 12.20 mm for S2), at this stage of design it is stated to be structurally safe. In fact, although maximum axial acceleration is higher in the second stage flight and bending loads from thrust vectoring not negligible, they are still expected to be lower than the loads considered in this analysis.

The final structural design parameters are summarized in Tab. 6.5; complete analytical derivations, equation sets, and verification workflows are documented in App. E.

Table 6.5: Final Structural Design Parameters

Parameter	**Stage 1**	**Stage 2**	**Justification**
Material	Al-Li 2195	Al-Li 2195	Cryogenic capability
Structural index (ε)	0.13	0.10	Historical validation
Derived thickness	12.35 mm	12.20 mm	Mass-budget driven
Structural length	16.00 m	5.17 m	Includes integrated interstage
Ring spacing [14]	0.85 m	TBE	D/4 optimization
Dome ratio	$\sqrt{2}:1$	$\sqrt{2}:1$	Isotensoid optimization
Shell mass	6,556 kg	2,093 kg	From $\varepsilon \cdot M_{\text{prop}}$
Safety Factors	**Value**	**Requirement**	
Buckling (axial compression)	2.67	> 1.4 (from S1) [27]	91% above minimum
Yield (tension side)	7.35	> 1.0 (from S1) [27]	635% above minimum
Shear buckling	6.87	> 1.4 (from S1) [27]	390% above minimum

Chapter 7

Trajectory Analysis & Re-Entry

7.1 Ascent Phase

As described in Ch. 4 the identification of the ascent trajectory was a core discipline in the design process, as its result would not only affect the disciplines involved in the **Core Design Loop** but would also provide the data on which the downstream **Design Verification** would be based on. To address this complex problem with the available tools, a simple approach based on key modeling assumptions was persecuted, with a downstream validation to assess if the obtained results were acceptable or not. In perfect compliance with this concept design goals.

7.1.1 Model & Key Assumptions

Being the Pegasus XL the main source for validation and wanting to keep the aerodynamic layout as simple as possible, to avoid the rise of uncertainties that couldn't be addressed at this stage of design, key assumptions had to be made. In fact, as detailed in Ch. 8, the elevator necessary for aerodynamic trim would serve also as control surface for the first stage. On the Pegasus XL this demonstrated to be sufficient, therefore, addition of thrust vectoring would only add complexity, mass, and losses. Yet, with aerodynamics being by themselves non-trivial at the regimes of interest, a reasonable model of the control surfaces would be out of scope for the goal of this concept design. To address these issues, a 2-DOF dynamic model, solved for optimal thrust orientation $\vartheta(t)$ and burning times, was implemented, with the following considerations. First, being the thrust vector direction of the first stage constrained to the body axis (i.e., no thrust vectoring), the rotation of this vector could be used as a 3-DOF proxy for the body orientation of the rocket. Secondly, control surfaces are assumed to be able to reproduce the "imposed rotation", ϑ, and changes in the C_L and C_D aerodynamic coefficients are neglected. These assumptions would make the simplicity of the 2-DOF model "talk" with models and analysis that needed orientation and rotation. Lastly, for the $\simeq 30\ s$ of high altitude atmospheric flight of the second stage, this same link between 2-DOF and 3-DOF models was kept to better estimate aerodynamic coefficients. After the Kármán line, aerodynamic forces were neglected and thereby these assumptions were not needed anymore. It is important to underline that since the second stage is supposed to be equipped with thrust vectoring, the above mentioned assumptions would result less solid; the 3-DOF GNC feasibility analysis is meant to address this issue and static stability issue as detailed in Ch. 8. Finally, a cartesian flat Earth approximation was made for the ascent trajectory, being the downrange and apogee sufficiently small with respect to the Earth's radius [14]. This would introduce an error on the computed trajectory, yet in compliance with the design goals final results were considered acceptable.

7.1.2 Problem Setting

Trajectory was optimized using a direct single shooting approach, solving for optimal $\vartheta(t)$ and burning times of first and second stage. Stage separation and second stage ignition time were accounted for respectively 5 s and 10 s, to be considered reasonable according to available data on launchers [36, 37]. The tool used was built-in MATLAB function `fmincon` that performed a local optimization on a cost function defined as the sum of burnout times, first stage separation and

$$\begin{cases} v_x = \frac{dx}{dt} \\ v_y = \frac{dy}{dr} \\ a_x = \frac{T}{m(t)}\cos\big(\vartheta(t)\big) - \frac{D(q,M,\alpha)}{m}\cos\gamma - \frac{L(q,M,\alpha)}{m}\sin\big(\gamma(t)\big) \\ a_y = \frac{T}{m(t)}\sin\big(\vartheta(t)\big) - \frac{D(q,M,\alpha)}{m}\sin\gamma + \frac{L(q,M,\alpha)}{m}\cos\big(\gamma(t)\big) - g(y) \\ \alpha = \vartheta(t) - \gamma(t) \end{cases} \tag{7.1}$$

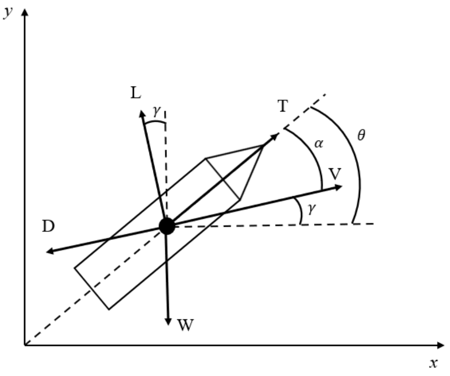

Figure 7.1: Dynamic model rapresentation.

second stage ignition, with non linear constraints defined on the target values as reported in Tab 7.1. Initial conditions were set according to the analysis in Sec. 8.1 and set to the ignition time of the first stage as in Tab 7.1. The excessive drag from a higher initial pitch angle would make the solver search for lower initial ϑ values. Yet, being the optimal solution local, a better solution was achieved by imposing an initial value. Moreover, a lower value is preferred as it shall be reached using controlled surfaces after the release as detailed in the Pegasus' flight data [16]. As a final note, computations were made in an inertial frame of reference, therefore the Earth's rotation contribute would be added to the final reached velocity as it is common practice [14].

v_{bo}	γ_{bo}	h_{bo}	ϑ_{bound}	t_{bound}
7.75 - 0.45 km/s	0°	200 km	[-20°; +90°]	$t_{design} \cdot [0.7; 1]$
v_0	γ_0	h_0	ϑ_0	-
170 m/s	0°	11.4 km	25°	-

Table 7.1: Boundary condition to the optimization problem.

7.1.3 Nominal Trajectory Considerations

In this section, results for nominal configurations are discussed, constituting the nominal trajectory of this design work, on which GNC [9], Uncertainty [10], Structural [6] analysis were later performed.

As detailed in App. L, trends similar to the Pegasus' flight data were obtained. In particular, approximate matches were found in: maximum $\gamma \simeq 34°$, peaks and profiles of aerodynamic coefficients, ascent trajectory profile, angular velocities and angular accelerations. The latter being less intense in this case, as shown in App. L, thereby supporting the control feasibility assumption. Yet, also differences were observed, probably linked to phenomena that could not be captured with this simplified analysis: the final first stage the Pegasus' aerodynamic coefficients slightly differ from the obtained ones, the same happens to α, as is reported [16] to stabilize at 0°, whilst in this case $\simeq 5°$ (see App. L). Another notable difference was found in max q, as it sits at around 32 kPa (see Fig. 7.3a) while in the Pegasus' surpasses 67 kPa according to [17, 38], and 48 kPa according to flight test data [16]. This difference is attributed mainly to a lower T/W ratio as Pegasus' is > 3 [17]. Difference in drag losses (see Ch. A), as detailed in Tab 7.2 as well, should attributed to this phenomena.

Finally a trade off analysis was conducted to evaluate the possibility of providing a $\gamma_0 > 0$. In Tab. 7.2 is reported a comparison with an initial $\gamma_0 = 20°$ trajectory. These results suggest that for a winged configuration an increase in the γ_0 does not provide substantial advantage; trading smaller drag losses with higher gravity losses. In a study on this specific matter [39], it was pointed out that a $\gamma_0 > 0$ in winged configurations would be less beneficial than in non winged, having its maximum contribute at $\gamma_0 \simeq 30°$. In fact, wings should be used when a sufficient pull-up cannot be provided by the carrier, as their presence is by nature penalizing due to mass and drag addition. In conclusion, to mitigate uncertainty on the carrier's capability to perform the pull-up maneuver, the non-zero flight path angle alternative was discarded.

	Δv_{drag}	Δv_{grav}	Δv_{steer}	$\Delta v_{\text{tot-loss}}$
$\gamma_0 = 0°$	268.77 m/s	821.99 m/s	59.85 m/s	1150.61 m/s
$\gamma_0 = 20°$	177.23 m/s	866.12 m/s	55.27 m/s	1098.62 m/s

Table 7.2: Pull-up performance comparison.

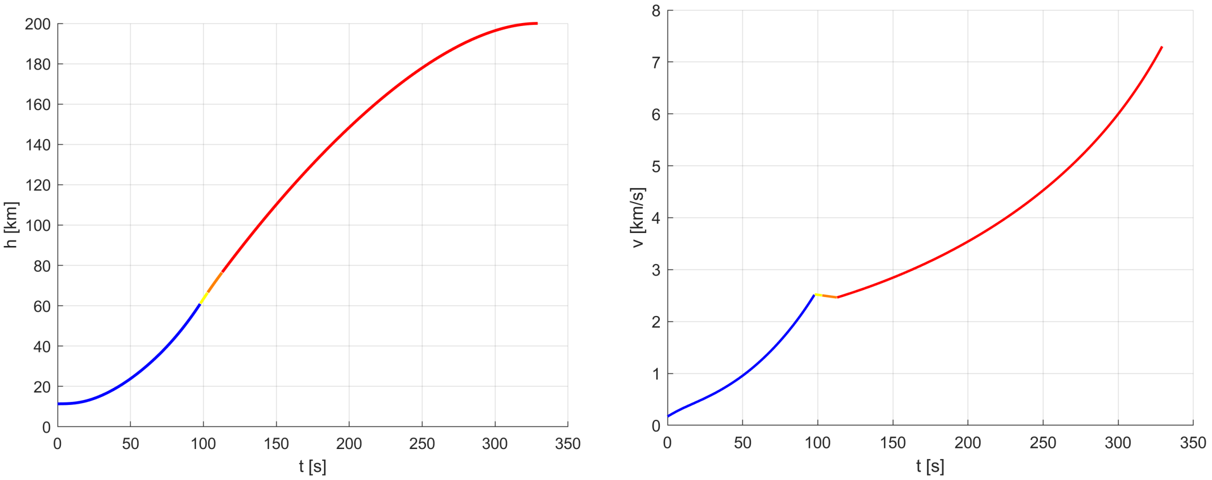

Figure 7.2: From left to right: altitude and speed module vs time.

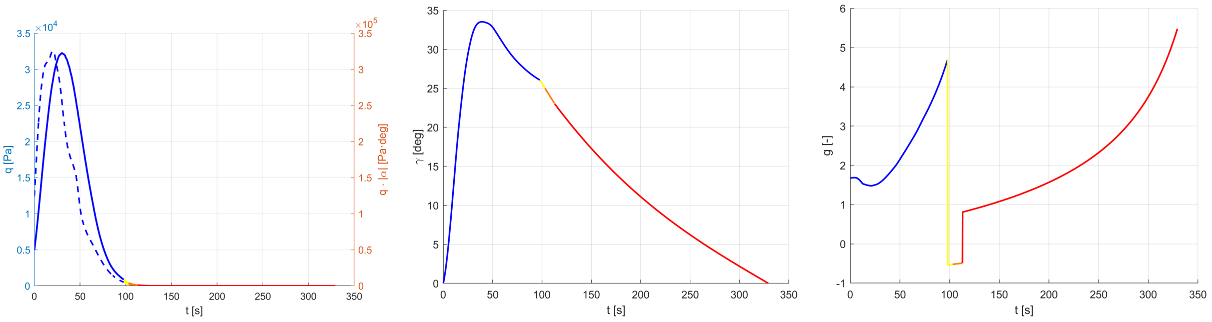

(a) $q(t)$ & $q(t) \cdot \alpha(t)$ in dashed line (b) $\gamma(t)$ (c) Axial g-load

Figure 7.3: Ascent attitude and flight path profiles. In blue first stage, in yellow coast for separation, in orange coast for second stage ignition and in red second stage

In compliance with the design goal, the output Δv_{design} was set to 8600 km/s providing an additional $\simeq 320$ m/s to account for uncertainties that would be addressed in further design iterations. Fig. 7.2 and 7.3 provide a representation of the obtained result for nominal trajectory. Finally, accelerations and their endurance were considered compliant with human rated flight [22].

7.1.4 Thermal Loads

Convective Heat Flux (Stagnation Point)

Convective heating at the capsule stagnation point during ascent is estimated using a model based on a convective heat-transfer coefficient coupled with the wall temperature. This formulation is applicable from the subsonic to moderate supersonic flow regimes characteristic of the ascent phase.

The model accounts for velocity, atmospheric properties, and wall temperature through an adiabatic wall temperature formulation and a Nusselt-number-based correlation, while rarefaction effects at high altitude are included via a Knudsen-number-based attenuation of the convective heat flux. The detailed mathematical formulation is provided in App. H.

As shown in Fig. 7.4, the stagnation-point temperature and convective heat flux reach a maximum during the early ascent and decrease rapidly with altitude. The predicted wall temperature remains below 725 K, confirming that convective heating during ascent is not a critical driver for TPS design.

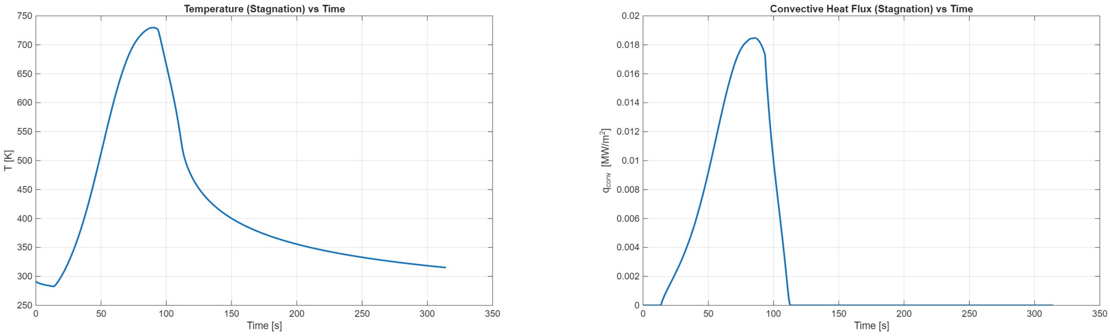

Figure 7.4: Stagnation-point thermal environment during ascent.

7.2 Capsule Descent and Atmospheric Re-entry

A classical blunt-body capsule configuration is adopted, exploiting aerodynamic drag for hypersonic deceleration and a multi-stage parachute system for controlled terminal descent. Trajectory is modeled on a 2-DOF, round Earth framework. The convective heat flux at the stagnation point is computed by implementing Eq. 7.2 [40]. Further details and TPS thermal response in App. F.

$$\dot{q}_{\text{conv}} = 0.57\,\mathrm{Pr}^{-0.6}\sqrt{\rho_e \mu_e}\sqrt{\left(\frac{dU_e}{dx}\right)_0} c_p (T_{\text{ad}} - T_w) \tag{7.2}$$

The capsule begins descent from h_{bo} with an initial inertial velocity of 7747.9 m/s and γ_{bo}. The discrepancy with v_{bo} is assumed to be addressed by the RCS on board, in this work not modeled. In fact, the descent initial velocity was toggled in order to cover the downrange from DRM carrier flight and ascent trajectory. Entrance in atmosphere is considered at the Karman line, with $\gamma_E \simeq -0.38°$.

Fig. 7.5 shows the altitude evolution as a function of ground range and time, highlighting the shallow entry corridor that enables progressive energy dissipation followed by a rapid descent below approximately 80 km where aerodynamic forces dominate.

7.2.1 Parachute System Selection and Performance

A two-stage parachute system consisting of a drogue and a main parachute is adopted. Both canopies are selected as circular slotted parachutes, offering a favorable balance between effective drag area and opening loads. [41] Detailed parachute dynamics and inflation modeling in App. F.

High-tenacity nylon is selected as canopy material, consistent with flight-proven systems such as Soyuz. [10] System-level redundancy is included through duplicated drogue and main parachutes, reflecting a conservative, crew-rated design philosophy. The main parachute is sized to achieve a terminal descent velocity of 8 m/s at sea level.

Fig. 7.5 shows the velocity evolution throughout the descent sequence, including the ballistic entry phase and the parachute-assisted terminal descent. Reefed inflation stages effectively mitigate

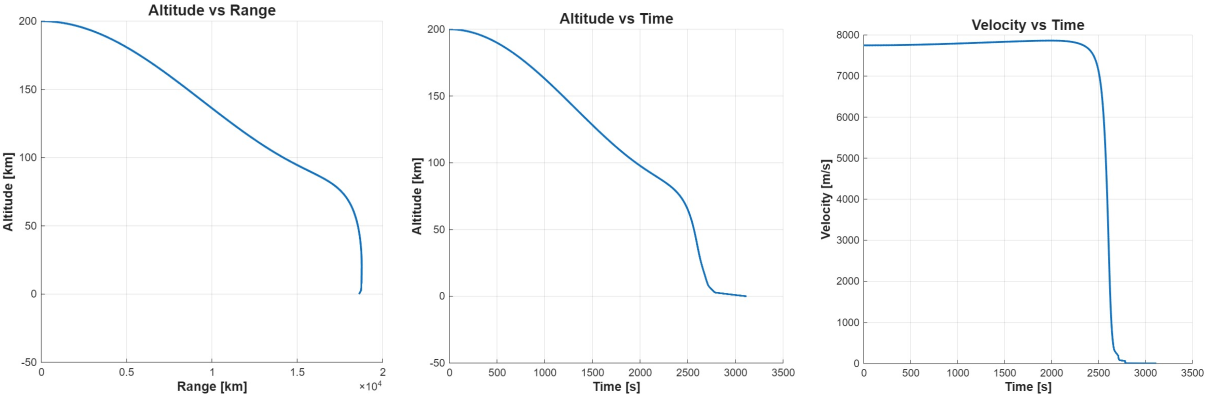

Figure 7.5: Descent profiles: altitude versus range (left), altitude versus time (center), and velocity versus time (right).

opening loads and ensure a smooth and controlled deployment. Soft-landing retro-rockets, as employed in Soyuz-class vehicles, are noted for completeness but are neglected in the trajectory integration due to their negligible influence on the overall descent profile [42]. More details in App. F.

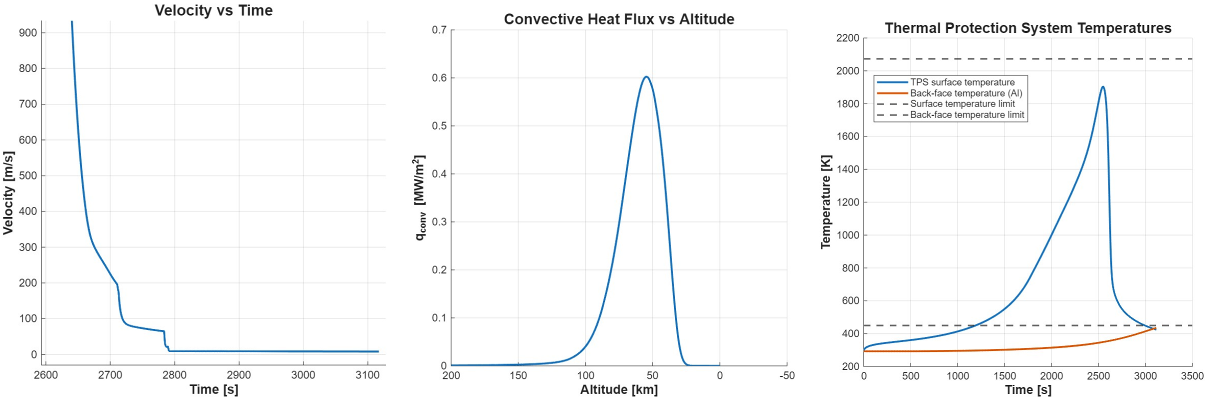

Figure 7.6: Re-entry and descent environment: velocity evolution including parachute deceleration (left), convective heat flux history (center), and thermal protection system response (right).

7.2.2 Thermal Loads and TPS Sizing Results

The trajectory-based aero-thermal analysis described in App. F yields a total integrated convective heat load of $Q = 154.3\,\mathrm{MJ/m^2}$, representative of long-range, high-energy atmospheric entry trajectories and constituting the primary driver for TPS sizing. Several non-ablative insulation materials were evaluated at preliminary design level. Among them, FRCI-12 provides the best trade-off between thermal performance and mass, satisfying both surface and back-face temperature constraints with the lowest total mass. The TPS thickness is selected accordingly, and the full sizing methodology is described in App. F. The selected TPS configuration is summarized in Tab. C.4. Fig. 7.6 shows the convective heat-flux evolution and the corresponding TPS thermal response, confirming that all temperature limits are respected throughout the descent.

7.2.3 Mechanical Loads and Crew Safety Assessment

The longitudinal deceleration experienced by the capsule is evaluated along the complete descent trajectory. The maximum predicted load factor is $g_{\max} = 8.13\,g$. This peak occurs during the high dynamic pressure phase of atmospheric re-entry and remains within accepted limits for short-duration crewed return profiles. The combined effects of shallow entry, aerodynamic braking, and reefed parachute deployment ensure that mechanical loads remain compatible with crew safety requirements as detailed in App. F.

Chapter 8

Aeronautical & Missile Aerodynamics

8.1 Carrier Analysis

The *HyperLander* mission implements a horizontal air-launch configuration, selecting the Stratolaunch (Roc) aircraft as the carrier. The design provides exceptional flexibility, with multiple potential airports and global eastward launch possibilities beyond this DRM as detailed in App. J.

The selected DRM launches from **Manila Airport, Philippines** towards the antipode near **Bom Morto, Brazil**. This leverages Manila's equatorial proximity for higher $\Delta v_{\text{latitude}}$. Detailed trajectory calculations [J] combined with flight envelope analysis yield the key parameters in Tab. 8.1.

Table 8.1: Carrier Analysis Key Parameters.

Total DRM Range	**Carrier covered distance**	$\mathbf{v_{max\text{-}carrier}}$	$\mathbf{h_{max\text{-}carrier}}$	$\Delta v_{\text{latitude}}$
$\simeq$ 20036 km	569.7 km	$\simeq$ 172 m/s	$\simeq$ 11948 m	$\simeq 450 m/s$

In compliance with design goals, the objective of this analysis was to define conservative limits to the flight envelope of the carrier, so that feasible ignition conditions could be derived. Modeling the release of the LV was considered beyond this work target and a 5 s time interval was considered based on the Pegasus' [43]. More precisely, the flight envelope was derived by scaling a known flight condition [44] on the payload that the airframe would carry on this mission. An additional 5% margin was introduced on maximum velocity leading the results in Tab. 8.1.

8.2 Aerodynamics

8.2.1 Aerodynamic Surface Sizing

The sizing of the aerodynamic surfaces has been done using a scaling approach based on the mass ratio, with the main constraint of maintaining the reference Wing Loading (W/S). This design choice enables the scaled launcher to have the same Lift-to-Weight ratio as the Pegasus XL at similar flight conditions. The mass ratio μ is defined as:

$$\mu = \frac{M_{\text{HyperLander}}}{M_{\text{Pegasus XL}}} \tag{8.1}$$

The aerodynamic surface scales linearly with the mass ratio. The linear scaling factor Ω (applied to chords and spans) is computed as the square root of the mass ratio ($\Omega = \sqrt{\mu}$).

Geometric Definitions

Reference geometric sizing of Pegasus XL's wings were found in the User's Guide Manual [45], tail fins dimensions were estimated based on the analysis made in [46], leading to the results shown in Tab. 8.2.

Table 8.2: Geometric parameters: Comparison between Pegasus XL (Ref) and Scaled surfaces.

	Main Wing		**Fin (each)**	
Parameter	**Ref**	**Scaled**	**Ref**	**Scaled**
Scaling Factor (λ)		2.223		
Mass Ratio (μ)		4.942		
Root Chord [m]	3.69	8.22	1.39	3.11
Tip Chord [m]	0.35	0.76	0.45	1.00
Semi-Span [m]	–	–	0.85	1.89
Full Span [m]	6.69	14.89	–	–
Planform Area [m^2]	13.56	67.02	0.79	3.90

Due to the scaling process, the values of Aspect Ratio ($AR = 3.30$), Taper Ratio ($\lambda_{\text{taper}} = 0.09$), Sweep angle ($\Lambda$ = 45°) and thickness ratio (t/c = 0.06) did not change from the reference aerodynamic surface configuration.

Configuration

Taking as reference Pegasus XL's wings configuration, the wing surface (X_{LE} = 17.16 m from the nose tip) has been mounted on top of a saddle. Its configuration also includes a wing-body fillet. In order to replicate its active aerodynamic function, a slightly bigger fillet, characterized by sweep angle (Λ_{fillet}) = 75°, ramp angle (θ) = 7.13° and total length (L) = 2.00 m, has been designed. Further details on these elements can be found in App. G. The fillet (2 m) and part of the wing tip (1.5 m) occupy the whole interstage; this was made according to two design choices: the interstage has the same internal structure of the first stage (enabling it to sustain part of the aerodynamic forces) and the separation from the two stages is done exclusively between the first stage and the interstage itself. For simplicity, the tail fins have been placed on the same plane of the wings with a third vertical one (0°, 90°, 180°) differently from the reference Pegasus fin configuration (90°, 210°, 330°) [2]. Elevators necessary for for trim and control of the launcher are included in the fin structure.

Aerodynamic Analysis

The aerodynamic performance and stability across the whole ascent trajectory has been studied adopting a multi-fidelity strategy. The analysis was divided into two different regimes based on the Mach number. For simplicity, a side-mounted wing configuration was employed for this analysis [2].

Table 8.3: Synthesized Aerodynamic Methodology and Applied Corrections.

Regime	**Method**	**Formula**	**Comment**
Subsonic to Low-Hyp. 0.6 < M < 4.5	**USAF Missile DATCOM [47–49]**	—	Standard high-fidelity engineering tool for preliminary rocket design.
Hypersonic 5 < M < 10	**Mod. Newtonian Theory [50]**	$C_p = C_{p_{\max}} \sin^2(\theta)$	Base inviscid solver based on pressure distribution.
Hybrid Corrections applied to to the Modified Newtonian Theory Solver			
Body Lift	Allen-Perkins/ Jorgensen [51, 52]	$C_{N_{\text{body}}} = \eta \cdot C_{d,c} \cdot \frac{S_{\text{plan}}}{S_{\text{ref}}} \cdot \sin^2(\alpha)$	Essential to capture non-linear lift generated by the long cylindrical fuselage.
Wing Lift	Linear Theory [53]	$C_{L\alpha} = \frac{4}{\sqrt{M^2-1}}$	Compensates Newtonian underestimation of wing lift contribute.
Viscous Drag	Van Driest II [54]	$C_{D,f} = C_f \frac{S_{\text{wet}}}{S_{\text{ref}}}$	Adds dissipative skin friction effects neglected by the inviscid impact theory.
Base Drag	Hoerner [55]	$C_{D,\text{base}} \approx \frac{1}{M^2}$	Accounts for base suction/pressure drop.

Results Analysis – The coefficient trends are consistent with the physics across all flight regimes. Interpolated results and further details can be found in App. G. The interpolation has been done after the computation of the trajectory. One of the aims of the design iterations will be to integrate the interpolated result in the trajectory analysis in order to obtain more coherent and realistic results. A preliminary comparison with the implied interpolated trajectory can be found in App. L.

8.2.2 Second Stage Aerodynamic Modeling

The aerodynamic analysis of the second stage differs from the one of the first stage due to the different flight conditions and absence of lifting surfaces. The extremely rarefied atmosphere that characterizes its operational altitude range (85-200 km) justifies the choice to switch to a Pure Modified Newtonian Solver avoiding most corrections. In these conditions the aerodynamics of the remaining assembly of the launcher, are dominated by the impact pressure on the surfaces [50].

Drag Corrections – The Newtonian solver accurately predicts the Wave Drag ($C_{\text{D, wave}}$), but empirical corrections were still necessary to account for residual marginal effects.

- **Base Drag:** This term naturally decays to zero at high Mach numbers, consistent with the extreme rarefied condition of the atmosphere;
- **Friction Drag:** After the launcher crosses the Kármán Line the Van Driest method becomes invalid. To prevent nonphysical results this term has been forced to zero above 100 km.

Results Analysis – The results shown in App G are compliant with the physics of our analyzed Mach range and mission profile. The Lift Coefficient shows negligible sensitivity to the Mach Number consistently with the Mach Number Independence Principle [50]. The Drag Coefficient shows the same trend after Mach 10 (point conservatively selected as the regime at which the Kármán Line is crossed).

8.2.3 Static Margin

Linking the 2-DOF trajectory data with the 3-DOF model as explained in Ch. 7, it was possible to have an insight on the static stability margin of the vessel as shown in Fig. 8.1.

The reference system has its origin (X = 0) at the base of the vessel, with the positive axis pointing towards the nose. In this reference frame the condition for static stability requires the X_{cg} to be located above X_{cp}. The analysis reveals a region of slight static instability during the first 8 s of flight. This enables the actuated tail fins to start the pitch-up maneuver with minimal resistance, enhancing maneuverability. Propellant depletion progressively shifts the launcher towards a statically stable configuration. Despite manifesting static instability in the upper atmopshere, the second stage is controlled via TVC, as detailed in Ch. 9.

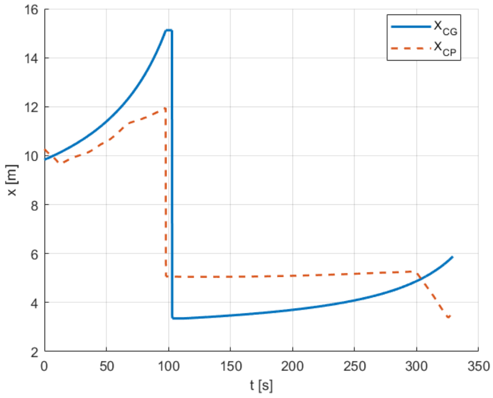

Figure 8.1: Static Margin

8.2.4 Capsule Aerodynamic Modeling

The *Sirius* capsule descent trajectory starts from an altitude of approximately 200 km to reach sea level. Since the physics of the airflow varies from Free Molecular Flow in the upper atmosphere to Continuum Fluid Mechanics in the lower atmosphere [50], a multi-regime approach was adopted. The analysis assumes a ballistic reentry profile with a constant angle of attack $\alpha = 180°$ (heat shield normal to the flow vector) with focus on the Drag Coefficient.

Table 8.4: Multi-region Drag Coefficient (C_D) modeling strategy across altitude regimes.

Altitude	Regime	Modeling Strategy
200–140 km	**Free Molecular Flow** ($Kn > 10$)	Constant C_D based on Orion hypersonic rarefied analysis [56] $C_D \approx 2.2$
140–100 km	**Transition**	Bridging function based on a smooth sine-squared interpolation between Molecular and Newtonian values $C_D = w C_{D_{\mathrm{mol}}} + (1-w) C_{D_{\mathrm{newt}}}$
100–50 km	**Continuum Fluid**	Panel Method based on Modified Newtonian Theory.
50–40 km	**Blending Zone**	Weighted interpolation applied to prevent discontinuities.
< 40 km	**Supersonic to Subsonic**	Experimental data from Orion Aerodynamic Database [57].

Results Analysis

The profile of the Drag Coefficient obtained from the multi-regions approach shows a reasonable agreement with the Aerodynamic Database of the Orion capsule. The transonic peak, the plateau at high Mach numbers and the transition to the Free Molecular Flow regime are consistent with the characteristic behaviour of blunt bodies in similar conditions, as shown in the Orion capsule analysis [56, 57]. Graph and further details can be found in App. G.

Chapter 9

Guidance & Control

As observed in Ch. 7 and in Ch. 8, the 2-DOF model issues and static instability issues of the second stage require a deeper analysis to meet the design goals. In this section the mentioned issues are addressed by providing a simple control analysis of this critical phase of the mission.

9.1 3-DOF Modeling

The vehicle dynamics are modeled using a cartesian 3-DOF formulation, including inertial translational motion and rotational motion about the out-of-plane axis. Thrust Vector Control (TVC), aerodynamic forces, and gravity are incorporated following standard aerospace vehicle dynamics formulations [58, 59].

The system state vector is defined as

$$z = [x\ y\ v_x\ v_y\ \vartheta\ q]^T.$$

$$\begin{cases} \dot{v}_x = \dfrac{1}{m}\Big(T\cos(\vartheta+\delta) - D\cos(\gamma) - L\sin(\gamma)\Big) \\ \dot{v}_y = \dfrac{1}{m}\Big(T\sin(\vartheta+\delta) - D\sin(\gamma) + L\cos(\gamma)\Big) - g \\ \dot{q} = \dfrac{1}{I_{\text{cg}}}\Big(M_{\text{aero}} - T\,x_{\text{cg}}\sin(\delta)\Big) \\ \dot{\vartheta} = q \end{cases} \tag{9.1}$$

The model resembles the one described in Ch. 7, with addition of rotational dynamics. δ represents the inclination of the thrust vector with respect to the body axis, being positive counterclockwise, M_{aero} represents the aerodynamic moment computed from models in Ch. 8 as L, D, and it is positive counterclockwise. x_{cg} represents the distance from base of the center of mass to which the thrust arm is approximated in this analysis. Aerodynamic effects are neglected above the sensible atmosphere ($h \geq 100$ km). The vehicle mass and inertia properties are modeled as time-varying to account for propellant consumption and staging events, as provided in App. K.

9.2 Control System Design

During the second stage, trajectory tracking is achieved using thrust vector control (TVC) by regulating the vehicle pitch angle to follow a reference profile obtained from a 2-DOF trajectory optimization. A proportional–integral–derivative (PID) controller is used to generate the thrust vector deflection command, with gains $K_P = 0.07$, $K_I = 0.05$, and $K_D = 2.5$.

A relatively large derivative gain provides additional damping to suppress initial oscillations caused by uncertainty in the pitch rate $q(0)$. The TVC command is saturated to ensure physically realizable limits and is applied only during the second stage burn.

9.3 Simulation Results

Nonlinear simulation results for the second stage are presented to evaluate trajectory tracking performance by comparing the controlled response with the optimized reference in terms of velocity, altitude, pitch angle, and thrust vector deflection.

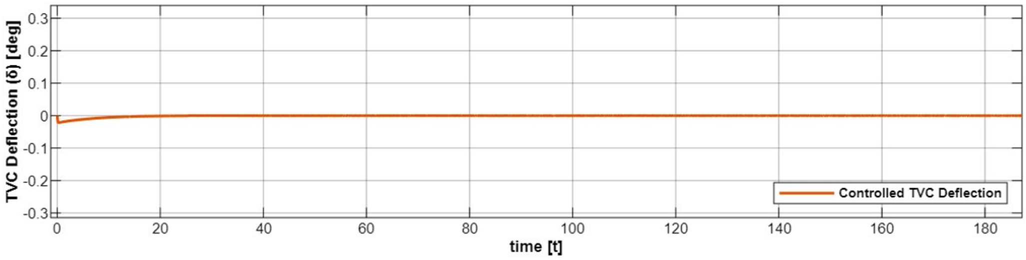

Figure 9.1: Commanded thrust vector deflection during the second stage.

Fig. 9.1 shows the commanded thrust vector deflection angle. An initial transient due to uncertainty in the initial pitch rate and derivative action is observed (as coming from 2-DOF model in 7), after which small thrust vector deflections are sufficient to maintain trajectory tracking. This proves limited control effort.

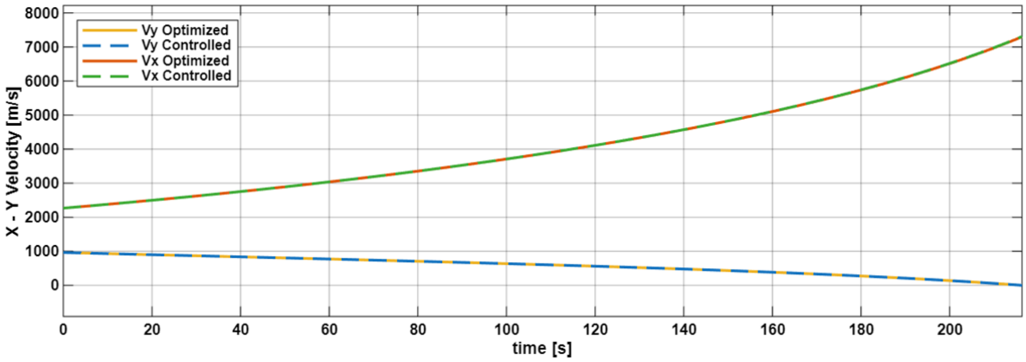

Figure 9.2: Optimized and controlled horizontal and vertical velocity components.

Fig. 9.2 shows the velocity tracking by looking at its components: the optimized final velocity of 7300 m/s is closely matched by the controlled response, which reaches 7307.4 m/s, corresponding to an absolute deviation of 7.4 m/s (0.101%).

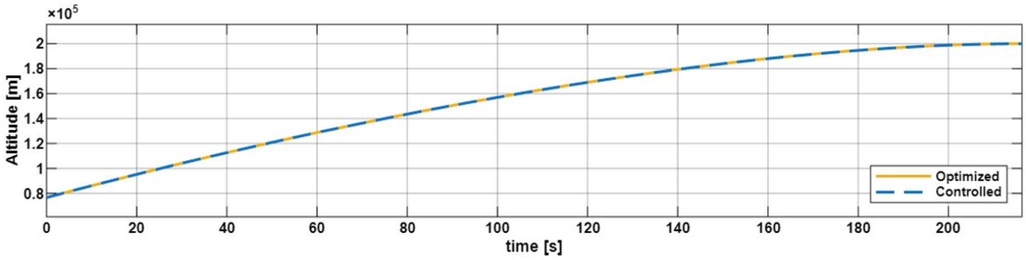

Figure 9.3: Optimized and controlled altitude during the second stage.

As illustrated in Fig. 9.3, the controlled trajectory reaches an altitude of 199886 m compared to the optimized value of 200000 m, resulting in an absolute deviation of 114 m (0.057%).

Chapter 10

Risk, Reliability and Safety

10.1 Casualty Risk

Public risk associated with capsule re-entry and landing is regulated by the Federal Aviation Administration through the **Expected Casualty (EC)** criterion, which limits the expected number of public casualties per mission to $EC < 10^{-4}$ in accordance with 14 CFR § 450.101 [60]. This criterion constrains overall public risk as a function of landing footprint, casualty area, and population density, rather than directly imposing a vehicle failure probability limit. The detailed formulation of the EC criterion and the assumptions adopted in its application are provided in App. I.

For the re-entry scenario considered, assuming a capsule mass of approximately 6.5 tonnes, an effective casualty area of about 290 m^2, and a representative population density of 6.1 people/km^2 at the nominal landing site, the EC criterion yields a maximum allowable re-entry failure probability of approximately **5.65%**, which represents a regulatory upper bound rather than a design objective.

Historical Soyuz descent-module flight data provide a representative benchmark for blunt-body capsule systems. Since the last fatal re-entry accident in 1971, more than 140 crewed Soyuz re-entries have been completed without catastrophic failure [61, 62]. A conservative statistical estimate places the catastrophic failure probability below 2.1% at 95% confidence, indicating that the EC-derived limit is conservative relative to demonstrated operational heritage.

10.2 Uncertainty Analysis and Landing Accuracy

Uncertainty analysis is performed to assess the robustness of ascent and descent trajectories with respect to dispersions in specific impulse, thrust, and vehicle mass, following established aerospace practice [63]. These uncertainties are propagated using a **Latin Hypercube Sampling (LHS)** approach, which provides efficient coverage of the input space with reduced variance compared to **standard Monte Carlo methods** [64, 65]. The uncertainty modelling framework and sampling strategy are described in detail in App. I.

The resulting ensemble of ascent trajectories exhibits an **asymmetric dispersion biased toward reduced altitude and downrange**, a physically expected outcome of fixed open-loop guidance combined with nonlinear dynamics.

Each ascent trajectory is subsequently propagated through the descent phase using the same numerical re-entry and landing models as the nominal case. Landing accuracy is evaluated by combining independent dispersion sources associated with entry-state uncertainty, atmospheric density variability, parachute system performance, and wind drift during subsonic descent using a **root-sum-square** formulation. The complete mathematical development of the dispersion model and the numerical sensitivities are provided in Appendix I. Entry-state sensitivity and wind drift dominate the total dispersion, yielding a landing accuracy on the order of a few kilometers (6.29 km).

The majority of descent trajectories (approximately 62%) reach or exceed the target downrange and can be corrected to the nominal landing site through controlled deceleration. The full set of simulated trajectories and statistical results supporting this conclusion are presented in App. I.

Chapter 11

Conclusions & Future Developments

The design goals reached as the output of this preliminary design process was a feasible concept addressing all the presented requirements with a success rate of **62%**. Yet, it has to be underlined that this design holds on strong assumptions which shall be relaxed in next design iterations with further vertical investigations.

First, this design cycle should be repeated with smoothed/interpolated aerodynamic coefficients, as suggested in Ch. 8, and with a payload adapter accounted in the overall length and mass.

Second, a nominal optimal trajectory shall be defined using a 3-DOF model; to pursue this aim, a more advanced aerodynamic modeling would be required, especially for elevators controls. These analyses would lead to a more precise loads analysis and thereby to allow a more detailed structural optimization, inserting this subject actively into the design loop.

Furthermore, control systems could be investigated on a wider scale, understanding also the capsule flight, to finally verify if the cases that hold higher energy in the uncertainty spectrum, can be successfully handled as assumed in this analysis.

Nevertheless, in this more complex investigation, release conditions shall be deepened, too. To do so, data from the Stratolaunch constructor (i.e. Scaled Composites) may be provided.

Finally, involving a dedicated capsule manufacturer is essential, given the requirement for a tailor-made design and the system's significant impact on the overall launch vehicle (LV) architecture.

Bibliography

1. Air & Space Forces Magazine. *AFRL Taps Rocket Lab for Space Cargo Experiment* Article describing AFRL collaboration with Rocket Lab for responsive space cargo and point-to-point launch concepts. `https://www.airandspaceforces.com/afrl-taps-rocket-lab-for-space-cargo-experiment/` (2025).
2. Wilhite, A. W. & Bartolotta, P. A. *Report of the Horizontal Launch Study* NASA Technical Reports Server (NTRS). Document ID: 20110015353. Report No.: DFRC-E-DAA-TN3568. Jointly sponsored by DARPA and NASA. Public use permitted. Available online via NTRS. June 2011.
3. Evans, M. *The X-15 Rocket Plane: Flying the First Wings into Space — Flight Log* Accessed 19 December 2025. Mach 25 Media (2020). `http://www.mach25media.com/Resources/X15FlightLog.pdf`.
4. Spaceflight Now. *Virgin Galactic's Rocket Plane Climbs Closer to Space* Article reporting on Virgin Galactic SpaceShipTwo flight test progress toward suborbital spaceflight. `https://spaceflightnow.com/2018/07/27/virgin-galactics-rocket-plane-climbs-closer-to-space/` (2025).
5. Rui, X. *et al.* A Survey on the Conceptual Design of Hypersonic Aircraft Powered by RBCC Engine. *Proceedings of the Institution of Mechanical Engineers, Part C: Journal of Mechanical Engineering Science* **237,** 4213–4245 (2023).
6. Krevor, Z., Howard, R., Mosher, T. & Scott, K. *Dream Chaser Commercial Crewed Spacecraft Overview* in *Proceedings of the 17th AIAA International Space Planes and Hypersonic Systems and Technologies Conference* (2011). `https://arc.aiaa.org/doi/abs/10.2514/6.2011-2245`.
7. Space Exploration Technologies Corp. (SpaceX). *Dragon – SpaceX* Accessed 19 December 2025. `https://www.spacex.com/vehicles/dragon`.
8. The Boeing Company. *CST-100 Starliner – Boeing* Accessed 19 December 2025. Boeing. `https://www.boeing.com/space/starliner`.
9. NASA. *NASA Exploration Systems Architecture Study – Crew Exploration Vehicle* tech. rep. (National Aeronautics and Space Administration, May 2005). `https://nss.org/wp-content/uploads/2017/07/NASA-exploration-systems-architecture-study-2005-05-Crew-Exploration-Vehicle.pdf` (2025).
10. European Space Agency. *Soyuz Launch Vehicle: The most reliable means of space travel* ESA (2011). `https://wsn.spaceflight.esa.int/docs/Factsheets/35%5C%20Soyuz%5C%20LR.pdf` (2025).
11. Pearlman, R. Z. *Shepard vs New Shepard: How astronaut daughter's Blue Origin launch stacks up* Accessed 19 December 2025. Space.com. `https://www.space.com/blue-origin-ns19-shepard-churchley-flight-compare`.
12. Astronautix / David Darling. *Dream Chaser – Astronautix* Accessed 19 December 2025. `http://www.astronautix.com/d/dreamchaser.html`.
13. National Aeronautics and Space Administration (NASA). *Crew Return Vehicle* Accessed 19 December 2025. `https://en.wikipedia.org/wiki/Crew_Return_Vehicle`.
14. Edberg, D. L. & Costa, W. E. *Design of Rockets and Space Launch Vehicles* 2nd ed. ISBN: 978-1-62410-641-5 (American Institute of Aeronautics and Astronautics, 2022).
15. Mosier, M., Harris, G., Richards, B., Rovner, D. & Carroll, B. *Pegasus First Mission – Flight Results* in *Annual AIAA/Utah State University Conference on Small Satellites* Aug. 27–30, 1990. NASA Accession Number: 91A27396 (Logan, UT, United States, Aug. 1990). `https://digitalcommons.usu.edu/smallsat/1990/all1990/76/`.

16. Noffz, G. K., Curry, R. E., Haering Edward A., J. & Kolodziej, P. *Aerothermal Test Results from the First Flight of the Pegasus Air-Launched Space Booster* NASA Technical Memorandum. NTRS Document ID: 19920002083. Report No.: NASA-TM-4330; H-1672; NAS 1.15:4330. Public distribution. Oct. 1991.
17. Northrop Grumman. *Pegasus User's Guide* Northrop Grumman (2020). `https://cdn.northropgrumman.com/-/media/wp-content/uploads/Pegasus-User-Guide-1.pdf` (2025).
18. Kibbey, T. *Small Launch Vehicle Sizing Analysis with Solid Rocket Examples* in *Combustion Subcommittee (CS)* June 3–7, 2019. NASA Document ID: 20190027424. Contract: 80MSFC18C0011 (Dayton, OH, United States, June 2019). `https://ntrs.nasa.gov/api/citations/20190027424/downloads/20190027424.pdf`.
19. Dominguez Calabuig, G. J. & Wilken, J. *Pre-conceptual Staging Trade-offs of Reusable Launch Vehicles* in *Proceedings of the 9th European Conference for Aeronautics and Space Sciences (EUCASS)* (June 2022). `https://www.researchgate.net/publication/361610412_Pre-conceptual_staging_trade-offs_of_reusable_launch_vehicles`.
20. Westphal, B. & Maiwald, V. *Critical Analysis and Review of Current Mars Mission Scenarios for SpaceX Starship* Paper discussing feasibility of Mars mission scenarios using Starship. 2022. `https://www.researchgate.net/publication/363753314_Critical_Analysis_and_Review_of_Current_Mars_Mission_Scenarios_for_SpaceX_Starship`.
21. Northrop Grumman. *Pegasus Launch Vehicle* `https://www.northropgrumman.com/what-we-do/space/launch-vehicles/pegasus` (2025).
22. NASA. *NASA Space Flight Human-System Standard Volume 1: Crew Health* NASA-STD-3001, Volume 1, Revision B (Jan. 2022). `https://standards.nasa.gov/standard/nasa/nasa-std-3001`.
23. NASA. *NASA Space Flight Human-System Standard, Volume 2: Human Factors, Habitability, and Environmental Health* NASA-STD-3001, Volume 2, Revision C (Feb. 2023). `https://standards.nasa.gov/standard/NASA/NASA-STD-3001_VOL_2` (2025).
24. Sforza, P. M. *Manned Spacecraft Design Principles* ISBN: 978-0-12-804425-4 (Butterworth-Heinemann, Oxford, UK, 2016).
25. Thomas, K. S. & McMann, H. J. *US Spacesuits* 1st ed. ISBN: 978-0-387-73979-3. `https://doi.org/10.1007/978-0-387-73980-9` (Springer-Praxis, Chichester, UK, 2006).
26. Gilbert, M. G. *The Max Launch Abort System – Concept, Flight Test, and Evolution* tech. rep. NF1676L-19585 (NASA Langley Research Center, 2015). `https://ntrs.nasa.gov/citations/20150000590` (2025).
27. NASA. *Structural Design and Test Factors of Safety for Spaceflight Hardware* NASA-STD-5001B (June 2022). `https://standards.nasa.gov/standard/NASA/NASA-STD-5001` (2025).
28. Sutton, G. P. & Biblarz, O. *Rocket Propulsion Elements* 9th ed. (Wiley, Hoboken, NJ, 2017).
29. United Launch Alliance. *Atlas V Launch Services User's Guide* United Launch Alliance (Mar. 2010). `https://www.ulalaunch.com/docs/default-source/rockets/atlasvusersguide2010.pdf` (2025).
30. NASA Safety and Mission Assurance. *Space Launch Report: Falcon 9 Data Sheet* NASA. `https://sma.nasa.gov/LaunchVehicle/assets/space-launch-report-falcon-9-data-sheet.pdf` (2025).
31. Colangelo, A. *Blue Origin Confirms BE-3U Uses Expander Cycle* Blue Origin announcement of BE-3U expander cycle engine with over 700 seconds test time. Main Engine Cut Off. `https://mainenginecutoff.com/blog/2018/08/be-3u-expander-cycle` (2025).
32. Baiocco, P., Bonhage, A., Tartaglia, A. & Sippel, M. *Prometheus, a European Low Cost and Reusable Rocket Engine* in *71st International Astronautical Congress (IAC)* (Virtual Event, Oct. 2020). `https://elib.dlr.de/142199/1/IAC20-D2.4.1.pdf` (2025).
33. Herberhold, M., Bussler, L., Sippel, M., Stappert, S. & Bernal Casado, J. Comparison of SpaceX's Starship with winged heavy-lift launcher options for Europe. *CEAS Space Journal.* `https://doi.org/10.1007/s12567-025-00625-8` (2025) (Jan. 2025).

34. Manning, C. G. *Technology Readiness Levels* TRL scale from 1 (basic research) to 9 (flight proven technology). National Aeronautics and Space Administration. `https://www.nasa.gov/directorates/somd/space-communications-navigation-program/technology-readiness-levels/` (2025).
35. Humble, R. W., Henry, G. N. & Larson, W. J. *Space Propulsion Analysis and Design* Revised First Edition. Page 230: Pressure vessel design and analysis for propellant tanks. ISBN: 978-0-07-031320-0 (McGraw-Hill, Sept. 1995).
36. Space Exploration Technologies Corp. *Falcon Payload Users Guide* Accessed: 2025-12-19. Space Exploration Technologies Corp. (May 2025). `https://www.spacex.com/assets/media/falcon-users-guide-2025-05-09.pdf`.
37. United Launch Alliance. *Vulcan Centaur User's Guide* United Launch Alliance (2023). `https://www.ulalaunch.com/docs/default-source/rockets/2023_vulcan_user_guide.pdf` (2025).
38. *Rocket and Spacecraft Propulsion: Principles, Practice and New Developments* 3rd ed. (ed Turner, M. J. L.) (Springer, Berlin, Heidelberg, 2009).
39. Sarigul-Klijn, N., Sarigul-Klijn, M. & Noel, C. Air-Launching Earth to Orbit: Effects of Launch Conditions and Vehicle Aerodynamics. *Journal of Spacecraft and Rockets* **42,** 569–575 (2005).
40. Fay, J. A. & Riddell, F. R. Theory of Stagnation Point Heat Transfer in Dissociated Air. *Journal of the Aeronautical Sciences* **25,** 73–85 (1958).
41. Mooij, E. *Re-entry Systems* 2024th. ISBN-10: 3031621735. ISBN: 978-3031621734 (Springer-Verlag GmbH, Cham, Switzerland, 2024).
42. Harvey, B. *Soyuz Landing Sequence* `https://www.russianspaceweb.com/soyuz-landing.html`. 2007.
43. Orbital Sciences Corporation. *Pegasus User's Guide* Release 7.0 Pegasus launch vehicle user guide (2010). `https://www.georing.biz/usefull/Pegasus_UG.pdf`.
44. Corda, S., Longo, C. & Krevor, Z. *Stratolaunch Air-Launched Hypersonic Testbed* in *AIAA SPACE and Astronautics Forum and Exposition* (Orlando, FL, Sept. 2018). `https://www.researchgate.net/publication/327675880_Stratolaunch_Air-Launched_Hypersonic_Testbed`.
45. Orbital Sciences Corporation. *Pegasus User's Guide, Release 6.0* (2007). `http://www.orbital.com` (2025).
46. Rhode, M. N., Engelund, W. C. & Mendenhall, M. R. *Experimental Aerodynamic Characteristics of the Pegasus Air-Launched Booster and Comparisons with Predicted and Flight Results* in *AIAA 13th Applied Aerodynamics Conference* (1995). `https://doi.org/10.2514/6.1995-1830` (2025).
47. Williams, J. E. & Vukelich, S. R. *The USAF Stability and Control Digital DATCOM. Volume I, Users Manual* Technical Report AFFDL-TR-79-3032. Final Report for Period August 1977 – November 1978. AD Number: ADA086557 (Air Force Flight Dynamics Laboratory, Air Force Wright Aeronautical Laboratories, Air Force Systems Command, Wright-Patterson Air Force Base, OH, Apr. 1979). `https://apps.dtic.mil/sti/pdfs/ADA086557.pdf`.
48. Williams, J. E. & Vukelich, S. R. *The USAF Stability and Control Digital DATCOM. Volume II, Implementation of Datcom Methods* Technical Report AFFDL-TR-79-3032. Final Report for Period August 1977 – November 1978. AD Number: ADA086558 (Air Force Flight Dynamics Laboratory, Air Force Wright Aeronautical Laboratories, Air Force Systems Command, Wright-Patterson Air Force Base, OH, Apr. 1979). `https://apps.dtic.mil/sti/pdfs/ADA086558.pdf`.
49. Williams, J. E. & Vukelich, S. R. *The USAF Stability and Control Digital DATCOM. Volume III, Plot Module* Technical Report AFFDL-TR-79-3032. Final Report for Period August 1977 – November 1978. AD Number: ADA086559 (Air Force Flight Dynamics Laboratory, Air Force Wright Aeronautical Laboratories, Air Force Systems Command, Wright-Patterson Air Force Base, OH, Apr. 1979). `https://apps.dtic.mil/sti/pdfs/ADA086559.pdf`.

50. Anderson, J. D. *Hypersonic and High-Temperature Gas Dynamics* chap. 3 (Hypersonic Inviscid Flow: Newtonian Theory). ISBN: 978-1-56347-780-5 (AIAA Education Series, 2006).
51. Allen, H. J. & Perkins, E. W. *A Study of Effects of Viscosity on Flow over Slender Inclined Bodies of Revolution* tech. rep. Report 1048 (National Advisory Committee for Aeronautics (NACA), 1951). `https://ntrs.nasa.gov/citations/19930090962` (2025).
52. Jorgensen, L. H. *Prediction of Static Aerodynamic Characteristics for Slender Bodies Alone and with Lifting Surfaces to Very High Angles of Attack* tech. rep. NASA TN D-7329 (NASA, 1973). `https://ntrs.nasa.gov/citations/19730019124` (2025).
53. Nielsen, J. N. *Missile Aerodynamics* ISBN: 978-0070465138. `https://archive.org/details/missileaerodynam0000niel` (2025) (McGraw-Hill, New York, 1960).
54. Van Driest, E. R. Turbulent Boundary Layer in Compressible Fluids. *Journal of the Aeronautical Sciences* **18,** 145–160. `https://doi.org/10.2514/8.1903` (2025) (1951).
55. Hoerner, S. F. *Fluid-Dynamic Drag: Practical Information on Aerodynamic Drag and Hydrodynamic Resistance* `https://archive.org/details/FluidDynamicDrag` (2025) (Hoerner Fluid Dynamics, Bakersfield, CA, 1965).
56. Moss, J. N., Boyles, K. A. & Greene, F. A. *Orion Aerodynamics for Hypersonic Free Molecular to Continuum Conditions* in *14th AIAA/AHI International Space Planes and Hypersonic Systems and Technologies Conference* AIAA Paper 2006-8081 (Canberra, Australia, 2006).
57. Bibb, K. L., Walker, E. L., Brauckmann, G. J. & Robinson, P. E. *Development of the Orion Crew Module Static Aerodynamic Database, Part II: Supersonic/Subsonic* in *29th AIAA Applied Aerodynamics Conference* AIAA Paper 2011-3507 (Honolulu, HI, 2011).
58. Zipfel, P. *Modeling and Simulation of Aerospace Vehicle Dynamics* 3rd ed. ISBN: 978-1563474569 (American Institute of Aeronautics and Astronautics, 2014).
59. Etkin, B. & Reid, L. D. *Dynamics of Flight: Stability and Control* 3rd ed. ISBN: 978-0-471-03418-6 (John Wiley & Sons, 1996).
60. Federal Aviation Administration. *Launch and Reentry Licensing Requirements* `https://www.ecfr.gov/current/title-14/chapter-IV/subchapter-C/part-450`. 14 CFR Part 450. 2023.
61. Lutomski, M. G. *Estimating the Reliability of a Soyuz Spacecraft Mission* tech. rep. NASA/TP-2010-216272 (NASA Johnson Space Center, 2010). `https://ntrs.nasa.gov/api/citations/20100014848/downloads/20100014848.pdf`.
62. Sgobba, T. in *Space Safety Regulations and Standards* (Elsevier, 2018).
63. *Space Mission Analysis and Design* 3rd ed. (eds Wertz, J. R. & Larson, W. J.) See Ch. 17 *Space Propulsion Systems* on Isp, thrust, and mass fraction driving trajectory sizing (Microcosm Press and Kluwer Academic Publishers, 1999).
64. McKay, M. D., Beckman, R. J. & Conover, W. J. A Comparison of Three Methods for Selecting Values of Input Variables in the Analysis of Output from a Computer Code. *Technometrics* **21,** 239–245 (1979).
65. Helton, J. C. & Davis, F. J. Latin Hypercube Sampling and the Propagation of Uncertainty in Analyses of Complex Systems. *Reliability Engineering & System Safety* **81,** 23–69 (2003).
66. Kibbey, T. P. *Small Launch Vehicle Sizing Analysis with Solid Rocket Examples* tech. rep. M19-7395 (NASA Marshall Space Flight Center, 2019). `https://ntrs.nasa.gov/api/citations/20190027424/downloads/20190027424.pdf`.
67. Dominguez Calabuig, G. J. & Wilken, J. *Pre-conceptual Staging Trade-offs of Reusable Launch Vehicles* in *9th European Conference for Aeronautics and Space Sciences (EUCASS) 2022* (2022). `https://elib.dlr.de/187097/`.
68. Sforza, P. *Commercial Airplane Design Principles* ISBN: 9780124199538. `https://books.google.it/books?id=exZIngEACAAJ` (Elsevier Science, 2014).
69. NASA. *NASA's Exploration Systems Architecture Study* tech. rep. (National Aeronautics and Space Administration, Nov. 2005). `https://nss.org/nasa-s-exploration-systems-architecture-study/` (2025).

70. Jones, D. S. *The Orion Pad Abort 1 (PA-1) Flight Test: A Propulsion Success* tech. rep. 20140017388 (NASA Technical Reports Server, 2014). `https://ntrs.nasa.gov/citations/20140017388` (2025).
71. Stillwater, R. A. & Merritt, D. S. *Orion Pad Abort 1 Flight Test: Simulation Predictions Versus Flight Data* tech. rep. 20110014236 (NASA Johnson Space Center, 2011). `https://ntrs.nasa.gov/citations/20110014236` (2025).
72. Jones, D. S. *Propulsion Overview of the Orion Pad Abort 1 (PA-1) Flight-Test Vehicle* tech. rep. 20170011295 (NASA Marshall Space Flight Center, 2013). `https://ntrs.nasa.gov/citations/20170011295` (2025).
73. Medina, E. A. & Stachowiak, S. J. *Orion Pad Abort 1 GN&C Design and Development* tech. rep. 20100005357 (NASA Johnson Space Center, 2010). `https://ntrs.nasa.gov/citations/20100005357` (2025).
74. McGowan, D. M. *Overview of the Orion Pad Abort 1 Launch Abort System* tech. rep. 20200010505 (NASA Langley Research Center, 2020). `https://ntrs.nasa.gov/citations/20200010505` (2025).
75. Jones, D. S. *Orion Launch Abort System (LAS) Propulsion on Pad Abort 1 (PA-1)* tech. rep. 20150002697 (NASA Marshall Space Flight Center, 2015). `https://ntrs.nasa.gov/citations/20150002697` (2025).
76. NASA. *NASA Procedural Requirements NPR 8705.2C, Chapter 2: Human-Rating Requirements for Space Systems* NPR 8705.2C (Apr. 2017). `https://nodis3.gsfc.nasa.gov/displayDir.cfm?Internal_ID=N_PR_8705_002C_&page_name=Chapter2` (2025).
77. NASA. *Human Rating Requirements for Space Systems* NASA-STD-8719.29 (2022). `https://standards.nasa.gov/standard/nasa/nasa-std-871929` (2025).
78. NASA. *Commercial Crew Program Essentials* National Aeronautics and Space Administration. `https://www.nasa.gov/humans-in-space/commercial-space/commercial-crew-program/commercial-crew-program-essentials/` (2025).
79. Volz, M. P., Chen, P. S., Gorti, S. & Salvail, P. *Development of Aluminum-Lithium 2195 Gores by the Stretch Forming Process* tech. rep. 20140011717. Mechanical properties of 2195-T8 gores at room temperature and LN2 conditions (NASA Marshall Space Flight Center, 2014). `https://ntrs.nasa.gov/api/citations/20140011717/downloads/20140011717.pdf` (2025).
80. NASA. *Space Shuttle External Tank Lightweight* tech. rep. 113020 (National Aeronautics and Space Administration, 2015). `https://www.nasa.gov/wp-content/uploads/2016/08/113020main_shuttle_lightweight.pdf` (2025).
81. Volz, M. P. *Aluminum 2195 T8 Gore Development for Space Launch System Core and Upper Stage* tech. rep. 20160008018. Development of stretch-forming process for Al-Li 2195 gores up to 0.75 inch thickness for SLS cryogenic tanks. Mechanical properties exceed STM 11-A1-LM specifications (NASA Marshall Space Flight Center, 2016). `https://ntrs.nasa.gov/api/citations/20160008018/downloads/20160008018.pdf` (2025).
82. MakeItFrom.com. *2195 (2195-T8) Aluminum* Standard mechanical properties: E = 69 GPa, Yield = 560 MPa, UTS = 590 MPa, Poisson = 0.33, Density = 2700 kg/m^3. `https://www.makeitfrom.com/material-properties/2195-2195-T8-Aluminum` (2025).
83. Wang, T. *et al.* Influence of Cryogenic Temperatures on the Mechanical Properties and Microstructure of 2195-T8 Alloy. *Metals* **13,** 740 (2023).
84. Aeronautics, N. & Administration, S. *Reinforced Carbon-Carbon (RCC) Panels* NASA Facts. Available online: `https://web.archive.org/web/20230208040456/https://www3.nasa.gov/centers/kennedy/pdf/167435main_RCCpanels08.pdf`. 2006.
85. Aeronautics, N. & Administration, S. *Reinforced Carbon-Carbon (RCC) Panels* NASA Facts. FS-2004-01-001-KSC (Rev. 2006). Available: `https://www3.nasa.gov/centers/kennedy/pdf/167435main_RCCpanels08.pdf`. 2006.

86. Li, X., Wen, K., Lin, B. & Xiong, B. Effect of Heat Treatment on the Microstructure and Mechanical Properties of Al–Cu–Li Alloy. *Journal of Iron and Steel Research International* **30,** 1345–1356 (2023).
87. Feng, H. *et al.* Effects of aging treatment on the mechanical properties and corrosion resistance of an Al-Cu-Mg-Li alloy. *Materials Today Communications* **35,** 105487. ISSN: 2352-4928. `https://www.sciencedirect.com/science/article/pii/S2352492823001770` (2023).
88. Indian Institute of Technology Madras. *Welding and Weldability Studies on 2195 Al–Cu–Li Alloy* tech. rep. Technical Report (IIT Madras, 2019).
89. Zhang, X., Liu, Y. & Liu, Z. Microstructure, Mechanical and Fracture Properties of Friction Stir Welded 2195 Al–Li Alloy Joints. *Chinese Journal of Aeronautics* **37,** 1–15 (2024).
90. Wang, H., Chen, Y. & Zhao, J. Microstructure Evolution of 2195 Al–Li Alloy Friction Stir Welded Joint and Performance Enhancement. *Journal of Materials Research and Technology* **25,** 3120–3132 (2023).
91. Liu, Y., Zhang, X. & Wang, Q. Thickness Effect on Fracture Toughness of 2195 Al–Li Alloy Friction Stir Welded Joints. *Materials* **17,** 3639 (2024).
92. National Aeronautics and Space Administration. *Orbiter Thermal Protection System, Thermal Materials* tech. rep. Archived from the original on 2023-02-12 (NASA Kennedy Space Center, 2006), 3. `https://web.archive.org/web/20230212114346/https://www.nasa.gov/centers/kennedy/pdf/167473main_TPS-06rev.pdf` (2008).
93. Goldstein, H. E. *Fibrous Ceramic Insulation* in *Advanced Materials Technology* Presented at the Advanced Materials Technology Seminar, Hampton, VA (National Aeronautics and Space Administration, Nov. 1982), 1–15. `https://ntrs.nasa.gov/api/citations/19830003890/downloads/19830003890.pdf`.
94. Lee, M. Y., Hofer, J. H., Bronowski, D. R. & Hardy, R. D. *Mechanical Properties of Thermal Protection System Materials* tech. rep. SAND2005-3173 (Sandia National Laboratories, Albuquerque, NM, June 2005). `https://www.osti.gov/servlets/purl/923159`.
95. Curry, D. M. *Thermal Protection Systems Manned Spacecraft Flight Experience* tech. rep. N93-12449. NASA Technical Reports Server (NTRS) Accession No. N93-12449 (NASA Johnson Space Center, 1992). `https://files01.core.ac.uk/download/pdf/42810795.pdf`.
96. Gordon, S. & McBride, B. J. *Computer Program for Calculation of Complex Chemical Equilibrium Compositions and Applications* tech. rep. NASA Reference Publication 1311. Web Interface: `https://www.grc.nasa.gov/www/CEAWeb/` (NASA Glenn Research Center, 1994). `https://ntrs.nasa.gov/citations/19950013764`.
97. Corda, S., Longo, C. & Krevor, Z. *Stratolaunch Air-Launched Hypersonic Testbed* in *22nd AIAA International Space Planes and Hypersonics Systems and Technologies Conference* (American Institute of Aeronautics and Astronautics, Orlando, FL, USA, 2018).
98. Weingarten, V. I., Seide, P. & Peterson, J. P. *Buckling of Thin-Walled Circular Cylinders* tech. rep. NASA-SP-8007. Design practices for predicting buckling of stiffened and unstiffened circular cylindrical shells (National Aeronautics and Space Administration, Aug. 1968). `https://ntrs.nasa.gov/api/citations/19690013955/downloads/19690013955.pdf` (2025).
99. Gerard, G. & Becker, H. *Handbook of Structural Stability Part III: Buckling of Curved Plates and Shells* tech. rep. NACA-TN-3783. Review of theories and test data on buckling of curved plates and shells under various loadings (National Advisory Committee for Aeronautics, Aug. 1957). `https://ntrs.nasa.gov/api/citations/19930084510/downloads/19930084510.pdf` (2025).
100. Guglieri, G. *Validation of a Simulation Model for a Planetary Entry Capsule* tech. rep. 03.3067 (European Space Agency (ESA), 2003).
101. Carandente, V., Savino, R., Iacovazzo, M. & Boffa, C. Aerothermal Analysis of a Sample-Return Reentry Capsule. *Fluid Dynamics & Materials Processing* **9** (2013).

102. Rajendrasing, R., Girka, Y., Zaharenko, V., Mallikarjuna, V. & Boopathiraja, A. Aerodynamics and Thermal Features of Reentry Spacecraft with Blunt Body Capsule. *Aviation and Space Technology and Technology* **2** (2015).
103. Pratap, M., Agrawal, A. K. & Kumar, S. Design and Selection Criteria of Main Parachute for Re-entry Space Payload. *Defence Science Journal* **69** (2019).
104. Pratap, M. & Agrawal, A. K. Flight Dynamics Modelling of Parachute Based Deceleration Systems. *Fluid Dynamics & Materials Processing* **9** (2013).
105. Zak, A. *The Soviet Manned Space Program* (Krieger Publishing, 1980).
106. Knacke, T. W. *From Space on a Parachute: A History of the Parachute in the Space Age* tech. rep. NASA TM-75577 (NASA, 1978).
107. NASA. *NASA Exploration Systems Architecture Study: Crew Exploration Vehicle* tech. rep. (National Aeronautics and Space Administration, 2005).
108. Raymer, D. P. *Aircraft Design: A Conceptual Approach* 6th. ISBN: 978-1-62410-490-9. `https://arc.aiaa.org/doi/book/10.2514/4.104909` (2025) (AIAA Education Series, 2018).
109. Anderson, J. D. *Fundamentals of Aerodynamics* 6th. ISBN: 978-1259129919. `https://www.mheducation.com/highered/product/fundamentals-aerodynamics-anderson/M9781259129919.html` (2025) (McGraw-Hill Education, 2016).
110. U.S. Committee on Extension to the Standard Atmosphere. *U.S. Standard Atmosphere, 1976* Sponsored by National oceanic and Atmospheric Administration (NOAA), NASA, and the United States Air Force (U.S. Government Printing Office, Washington, D.C., 1976).
111. Federal Aviation Administration, Office of Commercial Space Transportation. *System Safety Handbook, Volume 2: Operational Safety* (2011). `https://www.faa.gov/about/office_org/headquarters_offices/ast/media/AST_Safety_Handbook_Vol2.pdf`.
112. National Aeronautics and Space Administration. *Range Safety Requirements* NASA-STD-8719.14A (2020). `https://standards.nasa.gov/standard/nasa/nasa-std-871914a`.
113. Hanley, J. A. & Lippman-Hand, A. If Nothing Goes Wrong, Is Everything All Right? Interpreting Zero Numerators. *JAMA* **249,** 1743–1745 (1983).
114. Van Hooser, K. P. & Bradley, D. P. *Space Shuttle Main Engine—The Relentless Pursuit of Improvement* in *AIAA SPACE 2011 Conference & Exposition* Details thrust/Isp control, reliability improvements, and their impact on ascent performance (2011).
115. Plumer, E. & Elliott, D. *Probabilistic Mass Growth Uncertainties* in *NASA Cost Analysis Technical Interchange Meeting (CATIM)* Historical mass growth distributions and decay modeling across lifecycle milestones (2013).
116. National Aeronautics and Space Administration. *Mass Uncertainty and Application for Space Systems* in *Society of Allied Weight Engineers (SAWE) Annual Conference* Terminology and application of mass growth allowance (MGA) and remaining mass uncertainty (St. Louis, MO, 2013).
117. Bryson, A. E. & Ho, Y.-C. *Applied Optimal Control* (Taylor & Francis, New York, 1975).
118. Betts, J. T. *Practical Methods for Optimal Control and Estimation Using Nonlinear Programming* 2nd ed. (SIAM, Philadelphia, 2010).
119. Battin, R. H. *An Introduction to the Mathematics and Methods of Astrodynamics* (AIAA, Reston, VA, 1999).
120. Helton, J. C. Uncertainty and Sensitivity Analysis in the Context of Performance Assessment for Radioactive Waste Disposal. *Reliability Engineering & System Safety* **95,** 1332–1350 (2010).
121. Aerospace Testing International. *Stratolaunch Roc reaches new heights during flight tests* `https://www.aerospacetestinginternational.com/news/flight-testing/stratolaunch-roc-reaches-new-heights-during-flight-tests.html` (2025).
122. Stratolaunch Systems Corporation. *Stratolaunch Carrier Aircraft Completes Sixth Flight Test* `https://www.stratolaunch.com/news/stratolaunch-carrier-aircraft-completes-sixth-flight-test/` (2025).

123. Stratolaunch Systems Corporation. *Stratolaunch Completes First Flight with Talon-A Separation Vehicle* `https://www.stratolaunch.com/news/stratolaunch-completes-first-flight-with-talon-a-separation-vehicle/` (2025).
124. Stratolaunch Systems Corporation. *Stratolaunch Completes Historic First Flight of Aircraft* `https://www.stratolaunch.com/news/stratolaunch-completes-historic-first-flight-of-aircraft/` (2025).
125. Stratolaunch Systems Corporation. *Stratolaunch Completes Second Test Flight – Gives First Glimpse of Hypersonic Testbed Program* Press release distributed via PR Newswire. `https://www.prnewswire.com/news-releases/stratolaunch-completes-second-test-flight-301280814.html` (2025).
126. The Boeing Company. *Boeing 747-400 Reference Information* Accessed: 2025-12-21. `https://simviation.com/rinfo747.htm`.
127. Franklin, G. F., Powell, J. D. & Emami-Naeini, A. *Feedback Control of Dynamic Systems* 7th ed. ISBN: 978-0-13-349659-8 (Pearson, 2015).

Appendix A

Preliminary Analysis Details

In this appendix, details regarding the preliminary trade-off analysis are made explicit.

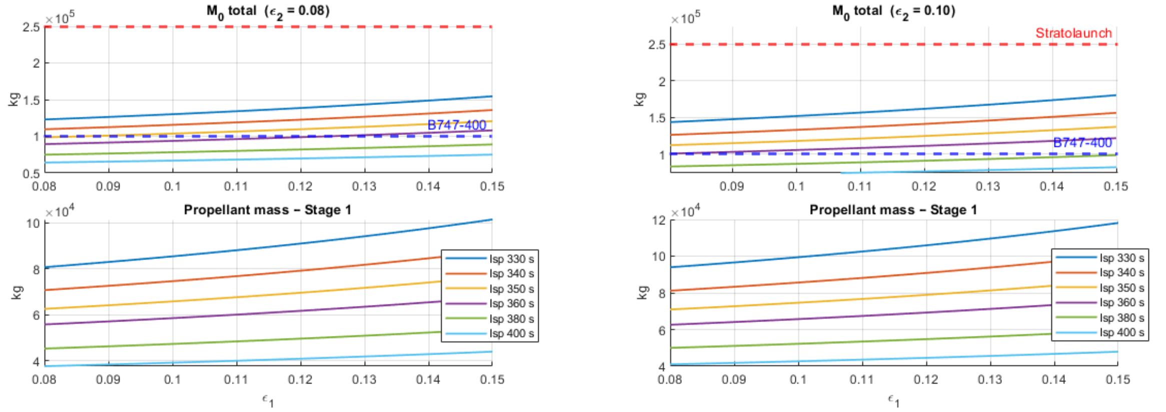

(a) Second-stage structural mass fraction $\varepsilon_{S2} = 0.08$.

(b) Second-stage structural mass fraction $\varepsilon_{S2} = 0.10$.

Figure A.1: Analysis of different second-stage structural mass fractions.

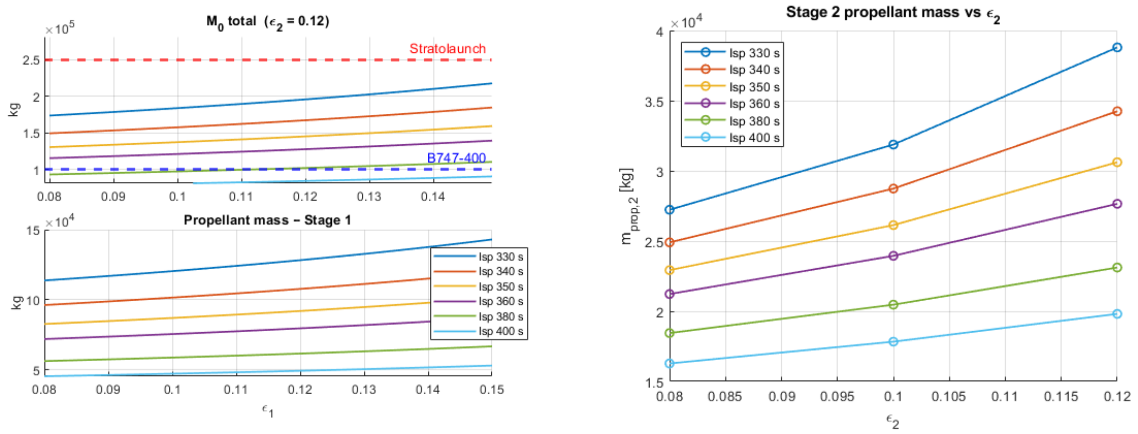

(a) Second-stage structural mass fraction $\varepsilon_{S2} = 0.12$.

(b) Second-stage propellant mass as function of ε_{S2}.

Figure A.2: Further analysis of structural mass fraction and resulting propellant requirements.

From these graphs a rough estimation of expected ranges in propellant mass in the first and second stage could be derived:

- First stage: $M_{\text{prop},1} \in [60, 80]$ t
- Second stage: $M_{\text{prop},2} \in [20, 30]$ t

Tab.A.1 summarizes the structural and mass properties of the Pegasus launch vehicle stages, as extracted from the Pegasus User Guide and related sizing studies.

[redacted]

cle [18]. Vertical axis: payload mass fraction ϕ.

[redacted]

(b) Propellant mass trend from [19]. Vertical axis: fuel mass fraction f.

Figure A.3: Comparative analysis of structural performance and propellant trends.

$$\varepsilon = \frac{M_s}{M_s + M_p} = \frac{f}{f+1} = 1 - \phi \tag{A.1}$$

$$f = \frac{M_s}{M_p} = \frac{\varepsilon}{1-\varepsilon} \tag{A.2}$$

$$\phi = \frac{M_p}{M_s + M_p} = 1 - \varepsilon \tag{A.3}$$

Stage	ε	ϕ	M_{prop} [kg]
Stage 1	≈ 0.084	≈ 0.916	15 014
Stage 2	≈ 0.096	≈ 0.904	3 925
Stage 3	≈ 0.140	≈ 0.860	770

Table A.1: Structural and propellant mass data for the Pegasus launch vehicle [17].

According to the analysis presented in [66], Pegasus's first stage is positioned between an equivalent high-performance configuration with $\gamma \approx 0.94$ and a low-performance configuration with $\gamma \approx 0.89$, corresponding to structural indexes $\varepsilon \approx 0.06$ and $\varepsilon \approx 0.11$, respectively.

A comparative semi-empirical analysis presented in [67] provides correlations between structural index (denoted as f in the reference) and propellant mass for launch vehicle stages covering a wide range of propellant combinations and recovery architectures (expendable, VTVL, horizontal landing).According to [20], the inert mass of the SpaceX Starship (methalox, VTVL) is expected to be approximately 125 t with a propellant mass of about 1 500 t, yielding a structural index $\varepsilon \approx 0.0769$.

In the semi-empirical chart, the corresponding structural parameter is $f \approx 0.083$, while the asymptotic value for Starship, given the propellant mass, would be $f \approx 0.07$, implying an underestimation of approximately 10% when relying on the asymptotic trend. This margin would be taken into account with the factor of safety. Given the expected mass ranges, data in Tab A.2 was derived.

	f	ε
Stage 1	≈ 0.075	≈ 0.0698
Stage 2	≈ 0.083	≈ 0.0766

Table A.2: Structural Indexes mentioned in 3

Appendix B

Payload Design Details

Reference Spacecraft Specific Volumes

The spacecraft specific volumes taken into consideration in this work are synthetized in Tab. B.1.

Table B.1: Reference Spacecraft Specific Volumes

Spacecraft	Specific Volume	Reference
Soyuz TMA	$1.33\,\mathrm{m^3/pax}$	[10]
ESAS ISS 6-crew Orion CEV	$3.25\,\mathrm{m^3/pax}$	[9]
Commercial aircraft (econ.)	$1.40\,\mathrm{m^3/pax}$	[68]
Sirius (selected)	$1.65\,\mathrm{m^3/pax}$	This work

Human-Rating Acceleration Requirements

The Sirius spacecraft design is governed by crew survivability criteria derived from NASA-STD-3001 and ESAS 2005 architecture [22–24, 26, 69–78]. Acceleration limits for dynamic flight phases are:

$$a_{\mathrm{limit}}(t) = \begin{cases} \leq 5\,g_0 & \text{Nominal ascent (sustained)} \\ \leq 8\,g_0 & \text{Abort operations } (t \leq 6\,\mathrm{s}) \\ \leq 12\,g_0 & \text{Emergency peak } (t \leq 0.5\,\mathrm{s}) \end{cases} \tag{B.1}$$

While historical systems like Apollo's Launch Escape System exhibited peaks exceeding $15\,g_0$, modern standards target significantly lower loads to accommodate deconditioned crew members [70].

LAS Motor Dimensions, Structural Integration & Aerodynamics

The abort motor sizing is derived from propellant volume requirements using standard solid propellants:

- **Propellant:** Hydroxyl-Terminated PolyButadiene (HTPB) [28]
- **Density:** $\rho_{\mathrm{prop}} = 1760\,\mathrm{kg\,m^{-3}}$ [28]
- **Volumetric loading:** 85% of motor internal volume [28]
- **Casing overhead:** Total motor volume = 1.2× propellant volume [28]

With a high aspect ratio for aerodynamic efficiency during ascent (AR = 4.0) [24], SRM radius is:

$$r_{\mathrm{motor}} = \sqrt[3]{\frac{V_{\mathrm{motor}}}{2\pi \cdot \mathrm{AR}}} = \sqrt[3]{\frac{1.022 \times 1.2/1.760}{2\pi \times 4.0}} \approx 0.298\,\mathrm{m} \tag{B.2}$$

This yields to a motor diameter $d_{\text{motor}} \approx 0.596\,\text{m}$ and a motor length $\ell_{\text{motor}} = \text{AR} \times d_{\text{motor}} \approx 2.382\,\text{m}$.

The supporting structures scale proportionally to capsule diameter ($D_{\text{cap}} = 3.4\,\text{m}$):

- **Adapter section:** $H_{\text{adapter}} = 0.450\,\text{m}$ (structural interface);
- **Jettison tower (truss):** $H_{\text{tower}} = 1.3 \times D_{\text{cap}} = 4.420\,\text{m}$;
- **Nose cone:** $H_{\text{nose}} = 0.35 \times \ell_{\text{motor}} = 0.834\,\text{m}$.

The complete "tower-equipped capsule" configuration represents a blunt body with drag coefficient $C_D \approx 1.6$ and a ballistic abort profile ($L/D \approx 0$) [70]. The ballistic coefficient is therefore [24]:

$$\beta = \frac{5.87}{C_D}\left(\frac{\ell}{d}\right)^{2/3} = \frac{5.87}{1.6}\left(\frac{1.90}{3.40}\right)^{2/3} \approx 3.07\,\text{kPa} \tag{B.3}$$

The full payload sizing is sketched in Fig. 5.1 and Tab. B.2.

Table B.2: Sirius LAS Detailed Geometry

Component	**Dimension**	**Value [m]**
Capsule		
Base diameter (D_{cap})	Requirement	3.400
Top diameter (D_{top})	Geometry ($\vartheta = 30°$)	1.20
Height (H_{cap})	Volume optimization	1.903
Sidewall angle (ϑ)	Orion heritage	30°
Launch Abort System		
Adapter height	Structural interface	0.450
Tower truss height	$1.30 \times D_{\text{cap}}$	4.420
Abort motor length	AR = 4.0 scaling	2.382
Abort motor diameter	Volumetric sizing	0.596
Nose cone length	$0.35 \times \ell_{\text{motor}}$	0.834
Total LAS height		**8.086**
Total stack height		**9.989**

Abort Performance Analysis

Due to the unique dynamics of the air-launch platform, LAS performance was validated in two limiting cases:

Scenario A: Pad Abort ($H = 0\,\text{km}$, $M = 0$) – Aerodynamic drag is negligible and:

$$a_{\text{sens}}(t) \approx T(t)/m(t) \tag{B.4}$$

Simulation results (Fig. B.1) confirm a peak load of 7.51g, compliant with the $8g$ constraint. The vehicle reaches a maximum velocity of $184.5\,\text{m}\,\text{s}^{-1}$ and 1182.2 m altitude gain within 10 seconds, providing adequate separation distance for safe parachute deployment.

Scenario B: Airborne Abort ($H \approx 11.4\,\text{km}$, $M \approx 0.50$) – Upon ignition from carrier aircraft speed the capsule enters a high-dynamic-pressure regime. Drag force rises quadratically, acting as damper:

$$a_{\text{net}}(t) = \frac{T(t) - \frac{1}{2}\rho v^2 S C_D - mg\sin\gamma}{m(t)} \tag{B.5}$$

With $C_D \approx 1.6$, aerodynamic loading attenuates peak acceleration to approximately **6.53** g_0. However, the initial horizontal momentum enables the vehicle to reach a higher terminal velocity of $379.3\,\mathrm{m\,s^{-1}}$, demonstrating effective energy conversion from horizontal to vertical motion.

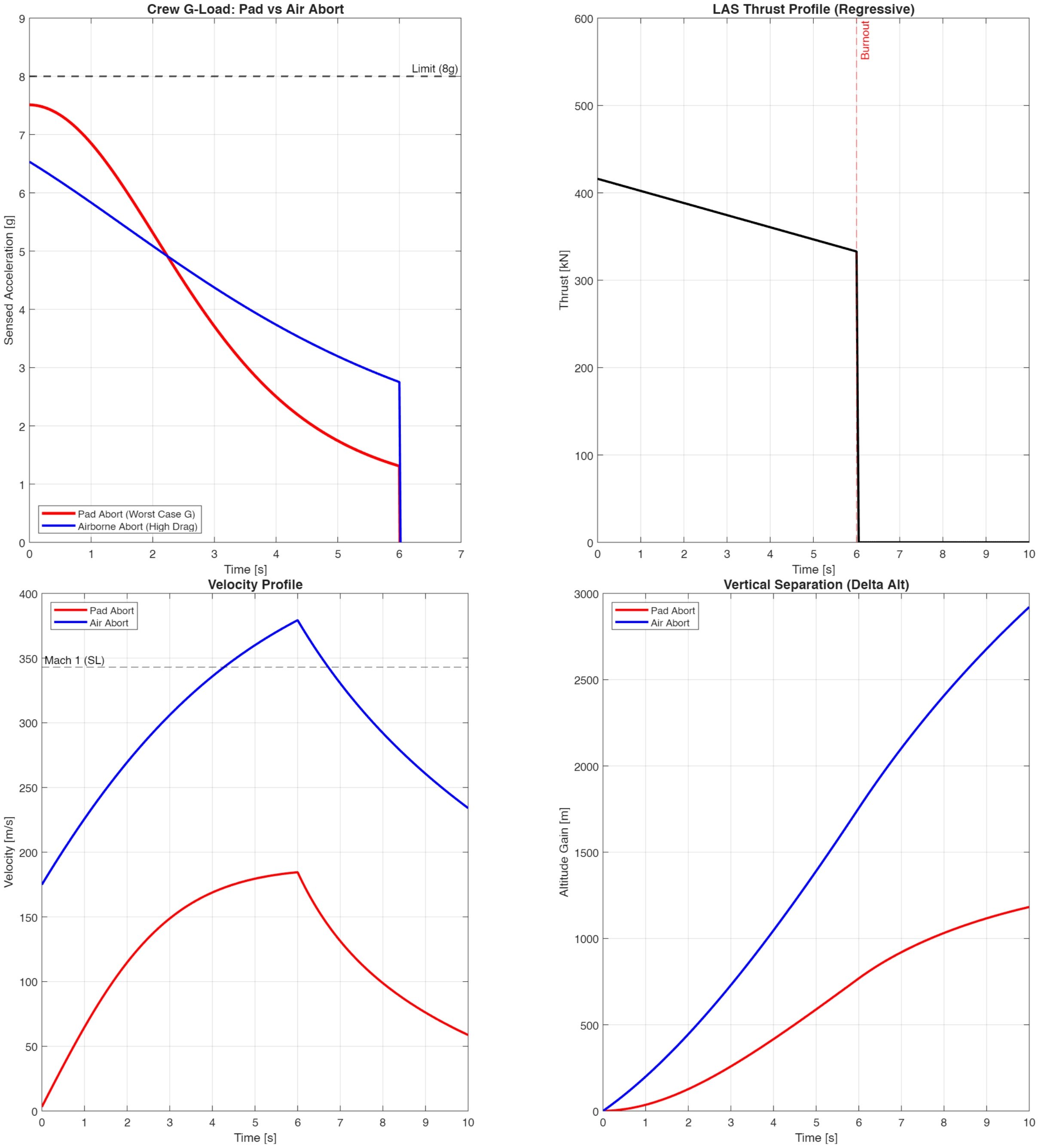

Figure B.1: Sirius LAS performance comparison between pad and airborne abort.

Looking at Fig. B.1, it can be seen that regressive thrust profile ($\psi = 0.20$) with $I_{sp} = 249\,\mathrm{s}$ maintains crew acceleration within human-rated limits. Also note that the air-launch scenario benefits from initial kinetic energy, enabling higher final velocity despite lower thrust-to-drag ratio. Instead, in pad abort scenario, the vehicle must overcome both gravitational drag and build velocity from zero.

Kinematic Performance Summary

Looking at the final values from Tab. B.3 and Fig. B.1, Sirius LAS achieves modern human-rating standards while maintaining heritage solid-propellant technology (TRL 8–9), ensuring high reliability and operational simplicity. The kinematic analysis confirms adequate separation performance in both worst-case (pad) and nominal (airborne) scenarios, with velocity profiles consistent with thrust-to-weight ratio and drag characteristics:

- **Pad abort:** Peak velocity $= 184.5\,\mathrm{m\,s^{-1}}$ (Mach 0.54), altitude gain $= 1182.2\,\mathrm{m}$ @ $t = 10\,\mathrm{s}$
- **Airborne abort:** Peak velocity $= 379.3\,\mathrm{m\,s^{-1}}$, benefiting from $v_0 = 172.2\,\mathrm{m\,s^{-1}}$ initial condition
- **Ballistic coefficient:** $\beta = 3.07\,\mathrm{kPa}$ (favorable for controlled descent)

Table B.3: LAS Performance vs. Historical Systems [24]

System	**Max g-load**	$(F/W)_0$	$t_{\mathbf{burn}}$ **[s]**	$v_{\mathbf{max}}$ **[m/s]**
Apollo LES	~ 15	14	5	~ 185 (pad)
Orion LAS	< 7	8	6	~ 195 (pad)
Sirius LAS	**7.51** (pad)	**7.5**	**6.0**	**379.3 (air)**

Appendix C

Material Properties Database

Aluminum-Lithium Alloy 2195

Aluminum-Lithium (Al-Li) Alloy 2195 is a third-generation, high-performance aerospace material selected for the primary structure of the HyperLander launch vehicle. Its development, led by NASA [79], was driven by the need for materials with a superior strength-to-weight ratio and excellent cryogenic properties for applications like the Space Shuttle's Super Lightweight External Tank [80] and the Space Launch System [81]. Compared to traditional tank alloys like 2219, 2195 offers a significant reduction in density (approximately 5% lower) coupled with markedly higher strength, directly enabling lighter and more capable launch vehicle structures. [79]

This appendix consolidates the mechanical, thermal, and processing data critical for the design, analysis, and manufacture of the vehicle's cryogenic tanks and primary airframe.

Mechanical Properties

The mechanical properties of Al-Li 2195 are highly dependent on its thermomechanical processing (temper) and the service temperature. The alloy is typically used in the T8 temper (solution heat-treated, cold worked, and artificially aged), which optimizes its strength. [79, 82]

Ambient Temperature Properties (at 298 K)

The following table summarizes the key mechanical properties for 2195-T8 at room temperature.

Table C.1: Mechanical properties of 2195-T8 at ambient temperature [82].

Property	Value	Unit
Density (ρ)	2.70 – 2.72	g/cm^3
Young's Modulus (E)	69 – 75	GPa
Yield Strength ($\sigma_{0.2}$)	500 – 560	MPa
Ultimate Tensile Strength (σ_u)	560 – 590	MPa
Elongation at Break	6.0 – 9.3	%
Shear Strength	~350	MPa
Shear Modulus	~26	GPa
Poisson's Ratio (ν)	0.33	–
Fracture Toughness (K_{IC}) (for base material in T-L orientation)	30 – 31	MPa$\sqrt{m}$

Cryogenic Temperature Properties (20 K – 77 K)

Al–Cu–Li alloy 2195-T8 demonstrates excellent mechanical performance at cryogenic temperatures, critical for LOX (~90 K) and LCH$_4$ (~90 K) tanks. Yield and ultimate tensile strength increase with decreasing temperature, with a pronounced rate of strengthening below ~133 K [83].

Unlike many structural alloys, 2195-T8 retains appreciable ductility even as strength rises, though fracture modes become less ductile at lower temperatures. The strengthening is attributed to suppressed dislocation cross-slipping and higher dislocation density [83]. At 20 K, ultimate tensile strength approaches 860 MPa [83].

Elevated Temperature Limits

The alloy retains useful mechanical properties at moderately elevated temperatures.

- **Maximum Service Temperature**: Approximately **210°C** for mechanical applications.
- **Thermal Stability**: Prolonged exposure to temperatures significantly above 150°C can lead to over-aging and degradation of mechanical properties.

Since the peak ascent temperatures are referring to the stagnation points, in a further development of the project these will be covered using the same approach used on the Space Shuttle, implementing long flight-proven Reinforced Carbon–Carbon tiles (RCC) [84, 85].

Fatigue and Fracture Toughness

Al–Cu–Li alloy 2195 exhibits significantly improved fatigue performance compared to legacy aerospace aluminum alloys, due to refined precipitate distributions and enhanced microstructural stability [86]. In T8 tempers, plane-strain fracture toughness depends strongly on thermomechanical processing and aging, with excessive T1 (Al_2CuLi) precipitation at sub-grain boundaries reducing toughness [87].

For welded joints, solid-state processes like friction stir welding generally preserve fatigue and fracture behavior close to the base material, unlike conventional fusion welding [86–88].

Weldability and Joint Efficiency

Fusion welding of Al–Li alloys, including 2195, is prone to hot cracking, porosity, and lithium loss, making it unsuitable for high-performance aerospace structures. Solid-state **Friction Stir Welding (FSW)** is therefore the industry-standard joining method [88, 89].

FSW joints in 2195 achieve high joint efficiency (85–95% of base material strength) and improved fatigue performance relative to fusion welds. Dynamic recrystallization in the weld nugget produces a fine, equiaxed grain structure that better preserves the alloy microstructure [90].

Fracture toughness (K_q) of FSW joints is thickness-dependent; plane-strain K_{IC} values require thick specimens, so predictive approaches are used to estimate toughness from thinner plate tests [91].

Physical and Thermal Properties & Chemical Composition

Table C.2: Physical and thermal properties of 2195. [82]

Property	Value	Unit	Notes
Coefficient of Thermal Expansion (α)	23	μm/m·K	From ~20°C. Critical for thermal stress analysis.
Thermal Conductivity (k)	130	W/m·K	At 25°C.
Specific Heat Capacity (c_p)	900	J/kg·K	At 25°C.
Melting Range	550 – 660	°C	Solidus to Liquidus.
Electrical Conductivity	20 – 34	% IACS	Varies with temper.

Table C.3: Nominal chemical composition of alloy 2195 (weight %). [82]

Al	Cu	Li	Mg	Ag	Zr	Fe (max)	Si (max)	Other
Bal.	3.7–4.3	0.8–1.2	0.25–0.8	0.25–0.6	0.08–0.16	0.15	0.12	Mn, Zn, Ti

- **Li**: Reduces density and increases modulus.
- **Cu & Li**: Primary strengthening via T_1 (Al_2CuLi) precipitation.
- **Mg & Ag**: Critical co-additions that promote uniform nucleation of T_1 precipitates [81].
- **Zr**: Forms Al_3Zr dispersoids to control grain structure and inhibit recrystallization.

Thermal Protection System

Based on the predicted aero-thermal environment and the resulting heat-load and temperature constraints from Sec. F, a non-ablative Thermal Protection System based on FRCI-12 was selected for the capsule forebody. This material provides an optimal trade-off between thermal performance and mass at preliminary design level, offering low density, low thermal conductivity, and high allowable surface temperature. The resulting configuration and associated mass breakdown are summarized in Tab. C.4.

Table C.4: Final TPS Design Summary.

Parameter	Symbol	Value
TPS Material	–	FRCI-12
TPS Thickness	t_{TPS}	0.057 m
TPS Areal density	σ_{TPS}	10.94 kg/m^2
TPS Mass (forebody)	m_{TPS}	99.4 kg

Tab. C.5 summarizes the properties considered. While LI-900 offers the lowest thermal conductivity, its low mechanical strength makes it susceptible to handling damage and acoustic loads. Conversely, LI-2200 offers high strength but imposes a significant mass penalty.

Table C.5: TPS Material Trade-Off (Properties at ambient conditions) [92–95].

Property	LI-900	FRCI-12	LI-2200
Density [kg/m^3]	~ 144	~ 192	~ 352
Composition	99.9% Silica	78% Silica, 22% Nextel	99.9% Silica
Thermal Cond. k [W/m·K]	0.046	0.056	0.060
Tensile Strength [MPa]	0.17	0.62	0.55
Max Use Temp. [°C]	1260	1260	1260

Therefore FRCI-12 was selected as the baseline material because it provides an optimal compromise:

- **Mass Efficiency:** It is approximately 45% lighter than LI-2200 while maintaining superior tensile strength due to the aluminoborosilicate (Nextel) fiber reinforcement.
- **Thermal Performance:** Although its thermal conductivity is slightly higher than LI-900 ($\sim$ 10%), the mass penalty required to increase thickness (t_{TPS}) to compensate is negligible compared to the structural reinforcement required if LI-900 were used.

Appendix D

Propulsion and Staging Design Details

Key Equations for Engine Scaling and Nozzle Design

The scaling factor λ for each engine variant is determined from the required thrust and reference thrust:

$$\lambda = \frac{F_{\text{req}}}{F_{\text{ref}}} \tag{D.1}$$

where F_{req} is the thrust required to meet the target T/W ratio at stage ignition, and F_{ref} is the reference thrust of the baseline Raptor 2 engine (Sea-Level or Vacuum).

For Stage 1, the required thrust is calculated as:

$$F_{\text{req,S1}} = \left(\frac{T}{W}\right)_{\text{S1}} \cdot m_{0,1} \cdot g_0 \tag{D.2}$$

where $m_{0,1}$ is the gross lift-off mass and $g_0 = 9.80665\ \text{m/s}^2$. For Stage 2:

$$F_{\text{req,S2}} = \left(\frac{T}{W}\right)_{\text{S2}} \cdot m_{0,2} \cdot g_0 \tag{D.3}$$

The throat area A_t is derived from the thrust equation:

$$A_t = \frac{F}{C_F \cdot p_c} \tag{D.4}$$

where C_F is the thrust coefficient, and p_c is the chamber pressure (300 bar for both stages). The thrust coefficient accounts for ideal expansion and ambient pressure effects:

$$C_F = C_{F,\text{ideal}} + \frac{(p_e - p_a)}{p_c} \cdot \varepsilon \tag{D.5}$$

where:

- $C_{F,\text{ideal}}$ is the ideal thrust coefficient;
- p_e is the static pressure at the nozzle exit;
- p_a is the ambient pressure;
- $\varepsilon = A_e/A_t$ is the expansion ratio.

The ideal thrust coefficient is given by:

$$C_{F,\text{ideal}} = \sqrt{\frac{2\gamma^2}{\gamma-1}\left(\frac{2}{\gamma+1}\right)^{\frac{\gamma+1}{\gamma-1}}\left[1-\left(\frac{p_e}{p_c}\right)^{\frac{\gamma-1}{\gamma}}\right]} \tag{D.6}$$

where γ is the ratio of specific heats (from CEA output).

The exit Mach number M_e is obtained by solving the area-Mach relation:

$$\frac{A_e}{A_t} = \frac{1}{M_e}\left[\frac{2}{\gamma+1}\left(1+\frac{\gamma-1}{2}M_e^2\right)\right]^{\frac{\gamma+1}{2(\gamma-1)}} \tag{D.7}$$

The static exit pressure p_e is then found from the isentropic relation:

$$\frac{p_e}{p_c} = \left(1+\frac{\gamma-1}{2}M_e^2\right)^{-\gamma/(\gamma-1)} \tag{D.8}$$

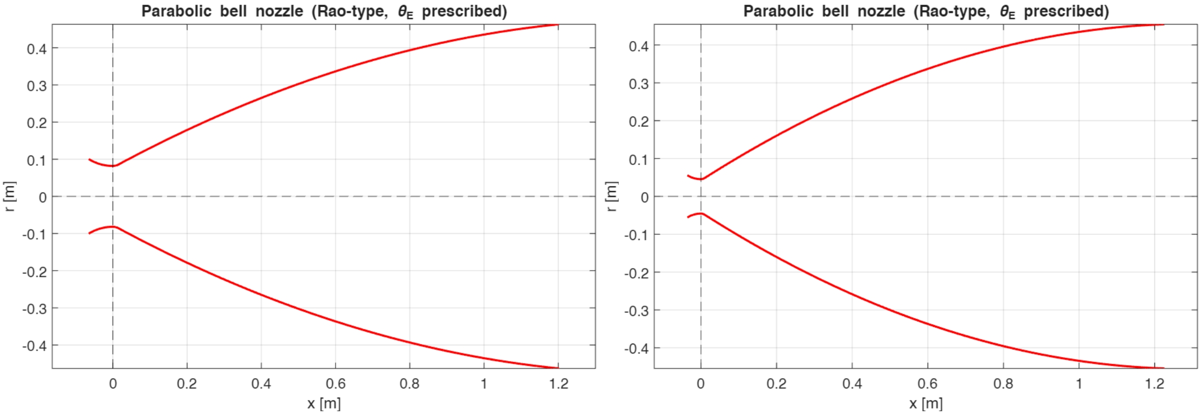

Figure D.1: From left to right, final Raptor 2 Lite Air and Vacuum nozzles.

NASA CEA Results for Ideal Performance

The NASA Chemical Equilibrium with Applications (CEA) code was used to compute the theoretical (ideal) performance of the LOX/LCH$_4$ full-flow staged-combustion cycle under the chamber pressure and mixture ratios adopted for the HyperLander engines. The CEA runs assume equilibrium expansion and do not account for real-gas losses, boundary-layer effects, or nozzle-wall friction. Consequently, the predicted specific-impulse values represent an upper bound for the given chamber conditions and expansion ratios. [96]

Two runs were performed, corresponding to the Stage 1 (air-launch optimized) and Stage 2 (vacuum optimized) nozzles. The input parameters and key outputs are summarized in Table D.1.

The CEA-derived ideal vacuum I_{sp} values are approximately 5.5 % (Stage 1) and 4.5 % (Stage 2) higher than the values adopted in the scaling and sizing calculations (Table 4.1), reflecting:

- **Real-gas and finite-rate chemistry losses** not captured by the equilibrium assumption;
- **Nozzle-wall friction and boundary-layer displacement** that reduce effective expansion;
- **Cooling-flow deductions** typical of full-flow staged-combustion engines;
- **Conservative design margins** required for human-rated missions.

Table D.1: NASA CEA ideal-performance results for HyperLander engines

Parameter	**Stage 1 (R2L "Air")**	**Stage 2 (R2L "Vacuum")**	**Unit**
Input			
Chamber pressure, p_c	300 [33]	300 [33]	bar
Mixture ratio, O/F	3.6 [33]	3.4 [33]	–
Expansion ratio, $\varepsilon = A_e/A_t$	32 [33]	100 [33]	–
Ambient pressure (exit)	0.22778 @ 11.4 km	0 @ > Kármán line	bar
Output			
Chamber temperature, T_c	3762.4	3741.6	K
Throat temperature, T_t	3570.7	3543.9	K
Exit temperature, T_e	2055.8	1461.2	K
Exit pressure, p_e	1.0392	0.22778	bar
Characteristic velocity, c^*	1850.9	1866.8	$\mathrm{m\,s^{-1}}$
Thrust coefficient, C_F (vacuum)	1.8310	1.9515	–
Ideal vacuum I_{sp}	**3594.3** (**366.4 s**)	**3784.7** (**385.9 s**)	$\mathbf{m\,s^{-1}}$

The adopted values ($I_{\mathrm{sp},1} = 343.17\,\mathrm{s}$, $I_{\mathrm{sp},2} = 368.50\,\mathrm{s}$) from [33] therefore include a realistic performance discount that aligns with heritage data for Raptor-class engines and ensures robust mission margins even in off-nominal conditions.

Key Equations for Stage Mass and Geometry Sizing

Inverse Tsiolkovsky for Stage Mass – The total wet mass of a stage (propellant + structure) required to deliver a given ΔV with a specified structural ratio ε is:

$$M_{\mathrm{stage}} = M_{\mathrm{pay}} \cdot \frac{\mathrm{MR}-1}{1-\varepsilon \mathrm{MR}}, \qquad \varepsilon = \frac{m_{\mathrm{dry}}}{m_{\mathrm{prop}} + m_{\mathrm{dry}}}, \qquad \mathrm{MR} = \exp\left(\frac{\Delta V}{I_{\mathrm{sp}} \cdot g_0}\right) \tag{D.9}$$

where M_{pay} is the payload mass for that stage, MR is the mass ratio, and ε is the structural ratio.

Propellant Mass Fractions – Given the mixture ratio $\mathrm{MR} = \dot{m}_{\mathrm{ox}}/\dot{m}_{\mathrm{fuel}}$, the mass fractions are:

$$f_{\mathrm{oxidizer}} = \frac{\mathrm{MR}}{\mathrm{MR}+1}, \quad f_{\mathrm{fuel}} = \frac{1}{\mathrm{MR}+1} \tag{D.10}$$

Tank Volume Calculation – Net propellant volumes (without ullage):

$$V_{\mathrm{ox,net}} = \frac{m_{\mathrm{prop}} \cdot f_{\mathrm{ox}}}{\rho_{\mathrm{ox}}}, \quad V_{\mathrm{fuel,net}} = \frac{m_{\mathrm{prop}} \cdot f_{\mathrm{fuel}}}{\rho_{\mathrm{fuel}}} \tag{D.11}$$

where $\rho_{\mathrm{LOX}} = 1149\ \mathrm{kg/m^3}$ and $\rho_{\mathrm{LCH_4}} = 421.1\ \mathrm{kg/m^3}$. Tank volumes include a 5% ullage factor [14]:

$$V_{\mathrm{tank}} = V_{\mathrm{net}} \times 1.05 \tag{D.12}$$

Tank Geometry – For isotensoid domes with elliptical ratio $\sqrt{2}:1$, providing optimal stress distribution for pressurized cylindrical vessels, [14] the dome height is:

$$H_{\mathrm{dome}} = \frac{R_{\mathrm{inner}}}{\sqrt{2}} = 1.20\,\mathrm{m} \tag{D.13}$$

considering the internal radius $R_{\mathrm{inner}} = 1.695$ m (coming from the structural stress analysis) given by $R_{\mathrm{inner}} = R_{\mathrm{outer}} - t_{\mathrm{wall}}$ is the internal radius. The volume of one dome is:

$$V_{\mathrm{dome}} = \frac{2}{3}\pi R_{\mathrm{inner}}^2 H_{\mathrm{dome}} = \frac{2}{3}\pi R_{\mathrm{inner}}^3 \frac{1}{\sqrt{2}} \tag{D.14}$$

The cylindrical and the total tank length required to accommodate the remaining volume is:

$$L_{\mathrm{cyl}} = \frac{V_{\mathrm{tank}} - 2V_{\mathrm{dome}}}{\pi R_{\mathrm{inner}}^2}, \qquad L_{\mathrm{tank}} = L_{\mathrm{cyl}} + 2H_{\mathrm{dome}} \quad \text{(including both domes)} \tag{D.15}$$

Appendix E

Workflow for Structural Stress Analysis

Load Analysis

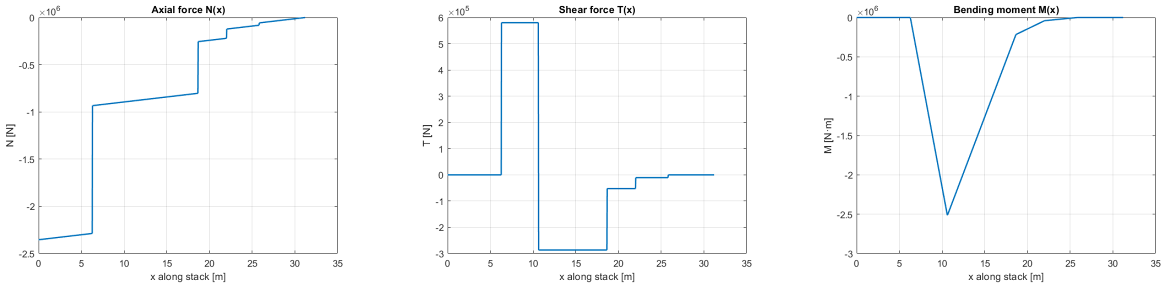

(a) Axial Action (b) Shear Action (c) Moment Action

Figure E.1: Internal Actions diagrams - *Max Q*

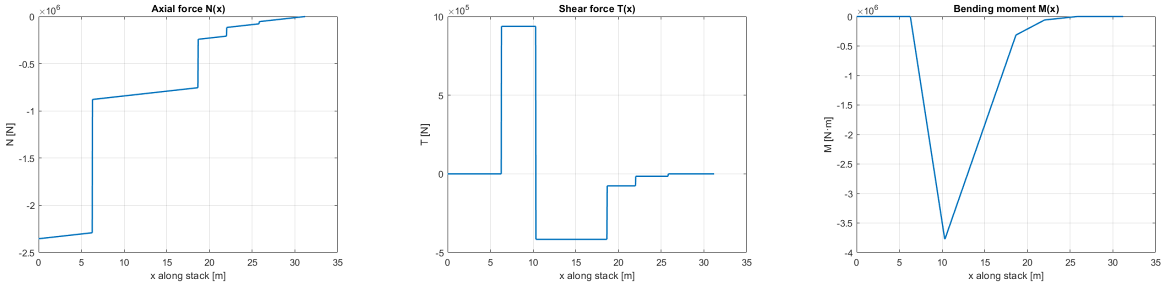

(a) Axial Action (b) Shear Action (c) Moment Action

Figure E.2: Internal Actions diagrams - *Max Qα*

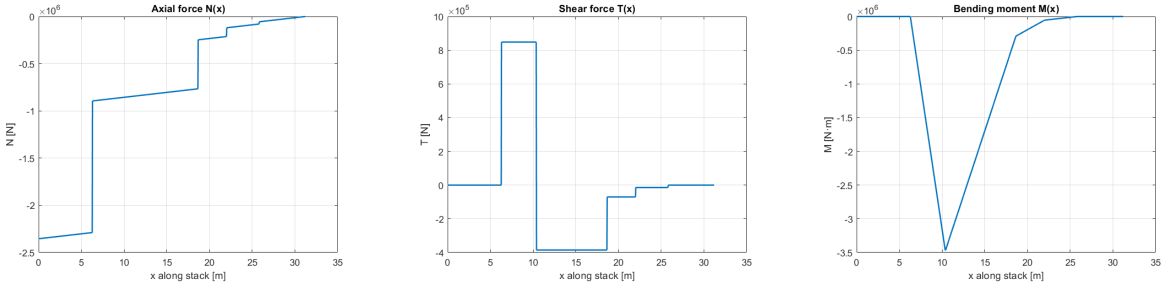

(a) Axial Action (b) Shear Action (c) Moment Action

Figure E.3: Internal Actions diagrams - *Maximum Angular Acceleration*

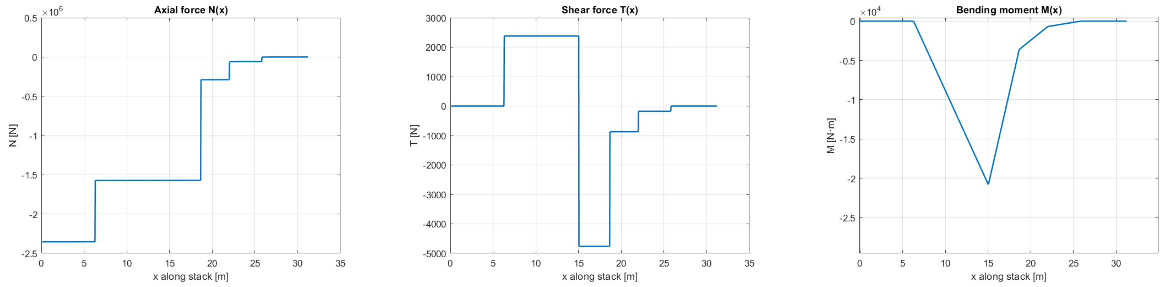

(a) Axial Action (b) Shear Action (c) Moment Action

Figure E.4: Internal Actions diagrams - *Maximum Axial Acceleration*

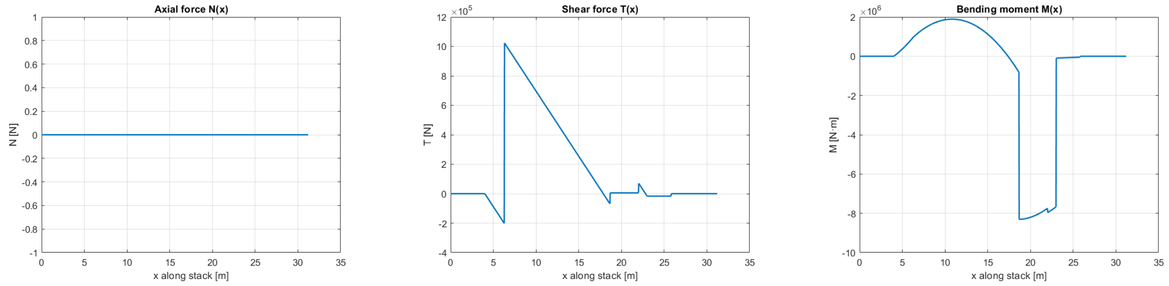

(a) Axial Action (b) Shear Action (c) Moment Action

Figure E.5: Internal Actions diagrams - *Loaded support*

Reference Load Cases for Structural Stress Analysis

The detailed data of the key load cases extracted from the flight profile loads analysis, used to drive the structural sizing, are summarized in Tab. E.1.

Table E.1: Brief Summary of Maximum Absolute Values from Internal Actions along x

Condition	Axial force	Shear force	Bending moment
Max Q (T+30.09 s) Maximum dynamic pressure condition	**2.35 MN**	580.16 kN	2.51 MN m
Max $Q\alpha$ (T+19.99 s) Peak aerodynamic angle-of-attack loading	**2.35 MN**	937.38 kN	3.77 MN m
Max $Q\alpha + 76$ m/s Wind Gust (T+19.99 s) Structural Design Driver	2.35 MN	**1.40 MN**	**5.63 MN m**
Max ϑ Acceleration (T+22.40 s) Critical dynamic control condition	**2.35 MN**	848.35 kN	3.47 MN m

Carrier Aircraft Loading – Another condition was considered, which was the captive carry phase with 1.5g normal load factor, This condition aims at understanding internal shear and bending loads due to transportation including a conservative 1.5g load factor. From literature [97] the length of the payload pylon was estimated being 19 m, and set 5 m from base on the LV. The pylon was then modeled with a uniformly distributed vertical force and moment, the latter necessary since the center of mass of the LV would not be aligned with the point where the shear resultant was applied (i.e., middle of the pylon).

The structural integrity of the HyperLander is verified against an *absolute maximum envelope*. Thereby, the shell thickness is tested on the **Max $Q\alpha$ + Wind** case, shown in bold on Tab. E.1, plus the design operating tanks pressure (320 kPa [35]).

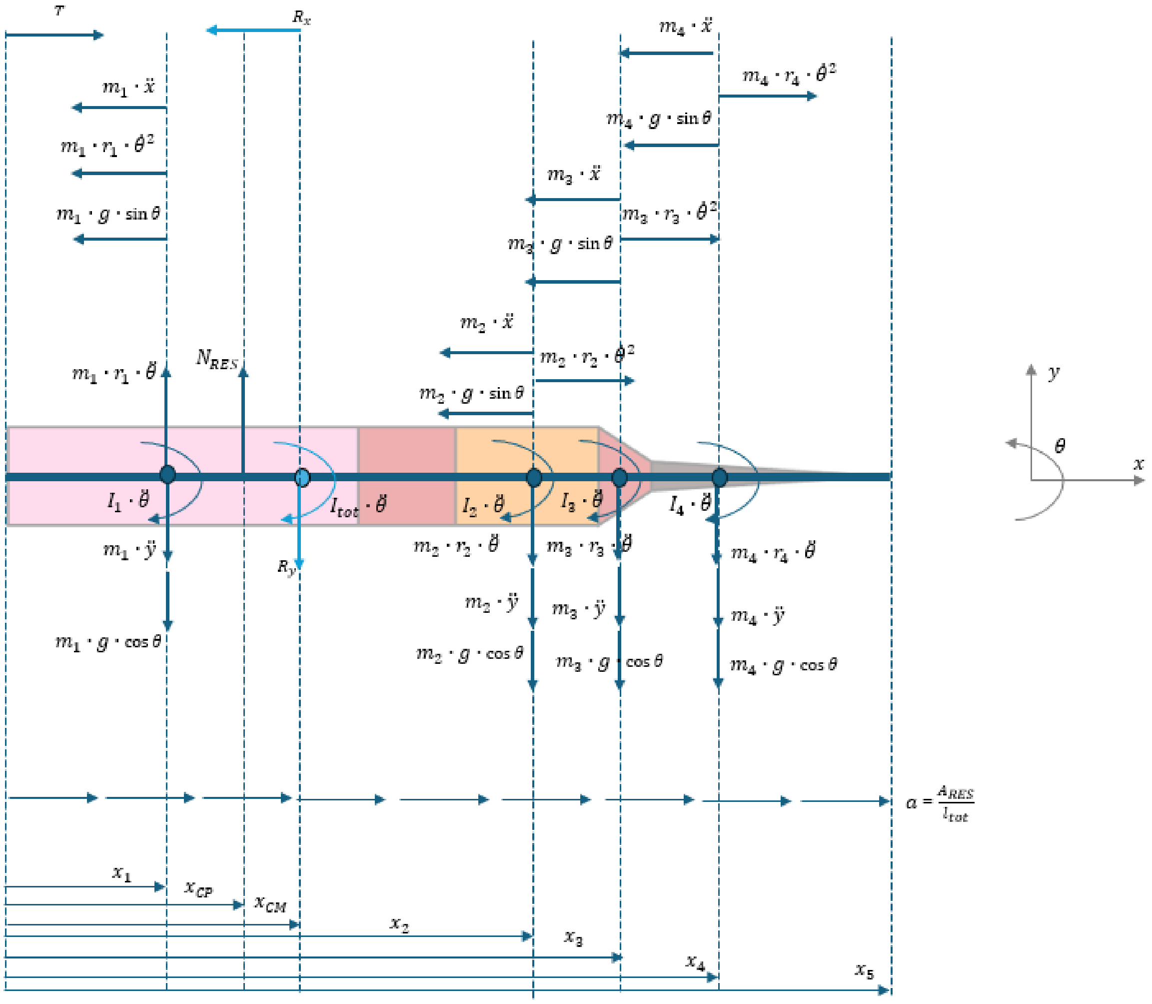

Figure E.6: HyperLander LV Beam model of the Loaded State (except the carrier loaded support).

Inertia Modeling

The LV is divided in four inertial segments: fisrt stage, second stage, capsule and LAS. Each segment is assigned a fixed longitudinal centroid $x_{G,i}$, position is measured from the base of the LV. For the stages center of gravity is set as the middle point, assuming a uniform mass distribution. As mentioned in 6 the inter-stage mass was modeled as part of the first stage's. Base lengths b_i are counted starting from the first stage's lower base. For the trapezoidal capsule, the centroid location is

$$x_{G,\mathrm{cap}} = x_{0-cap} + \frac{l_{\mathrm{cap}}}{3}\,\frac{b_3 + 2b_4}{b_3 + b_4}, \tag{E.1}$$

while for the triangular LAS:

$$x_{G,\mathrm{LAS}} = x_{0-LAS} + \frac{l_{\mathrm{LAS}}}{3}. \tag{E.2}$$

Global Center of Gravity

The instantaneous global center of gravity is computed as

$$X_{\mathrm{CG}} = \frac{\sum_i M_i x_{G,i}}{\sum_i M_i}. \tag{E.3}$$

Moments of Inertia About Segment CG

Stages are modeled as uniform plates, therefore:

$$I_{z,i} = \frac{M_i}{12}\left(l_i^2 + b_i^2\right). \tag{E.4}$$

For the capsule (isosceles trapezoid), the polar geometric inertia is

$$I_{z,G}^{\mathrm{cap}} = I_{x,G} + I_{y,G}, \tag{E.5}$$

with

$$I_{x,G} = \frac{l_{\mathrm{cap}}}{48}(b_3 + b_4)(b_3^2 + b_4^2), \tag{E.6}$$

$$I_{y,G} = \frac{l_{\mathrm{cap}}^3}{36}\,\frac{b_3^2 + 4b_3 b_4 + b_4^2}{b_3 + b_4}. \tag{E.7}$$

The corresponding mass inertia is obtained via area scaling supposing uniform mass distribution:

$$I_{\mathrm{cap}} = M_{\mathrm{cap}}\frac{I_{z,G}^{\mathrm{cap}}}{A_{\mathrm{cap}}}. \tag{E.8}$$

The Launch Escape System (LAS) is modeled as a uniform isosceles triangular plate, with base b_4 and height l_{LAS} oriented along the longitudinal x axis.

The geometric area of the triangle is

$$A_{\mathrm{LAS}} = \frac{1}{2} b_4 l_{\mathrm{LAS}}. \tag{E.9}$$

The centroidal second moments of area are

$$I_{x,G}^{\mathrm{LAS}} = \frac{b_4\, l_{\mathrm{LAS}}^3}{36}, \tag{E.10}$$

$$I_{y,G}^{\mathrm{LAS}} = \frac{b_4^3\, l_{\mathrm{LAS}}}{48}. \tag{E.11}$$

The polar moment of area about the centroid is therefore

$$I_{z,G}^{\mathrm{LAS}} = I_{x,G}^{\mathrm{LAS}} + I_{y,G}^{\mathrm{LAS}}. \tag{E.12}$$

Assuming uniform mass distribution, the mass moment of inertia about the centroid is obtained by area scaling:

$$I_{\mathrm{LAS}} = M_{\mathrm{LAS}} \frac{I_{z,G}^{\mathrm{LAS}}}{A_{\mathrm{LAS}}}. \tag{E.13}$$

Parallel Axis Theorem

The total moment of inertia about the global center of gravity is finally obtained using the Huygens-Steiner theorem:

$$I_{\mathrm{CG}} = \sum_i \big(I_i + M_i (x_{G,i} - X_{\mathrm{CG}})^2\big). \tag{E.14}$$

This formulation allows the instantaneous evaluation of the vehicle inertia properties, consistently accounting for staging events, mass depletion, and shifting reference frames.

Mass Derivation

To perform the stress analysis on the cylindrical shell that combines tank and outer shell thicknesses Ch. 6, available inert mass from the structural indexes defined in Ch. 3 and overall mass layout discussed in Ch. 6 had to be derived. The procedure is documented in Tab. E.2, and it was motivated by the simplicity required by design goals and in agreement with literature [35]. It is important to underline that at this level of design, thickness related to propellant tanks are assumed to be equal for both LCH_4 and LOX, as literature suggests similar thermal insulation MERs [14], and length is taken into account for the different volumes required. Moreover they are considered to be pressurized at the same pressure mentioned above (320 kPa). Wings and fins masses are derived from the Pegasus's[17] and by employing scaling factor as presented in 8.

Table E.2: Structural Mass Breakdown of the LV Stages.

Stage	Component	Mass (kg)	Percentage (%)
Stage 1	**Overall Mass**	**10841**	**100.0**
	Raptor 2 Lite Air Engines (2×) + Thrust Structure	2176	20.1
	Wings + 3 ×	1759	16.2
	Avionics & power	350	3.2
	Propellant Tanks + Outer shell (Integrated with Interstage)	6556	60.5
Stage 2	**Overall Mass**	**2521**	**100.0**
	Raptor 2 Lite Vacuum engine	428	17.0
	Payload Adapter (to be estimated in further development)	0	0.0
	Avionics (embedded in Sirius capsule)	0	0.0
	Propellant tanks + Outer Shell	2093	83.0

Key Equations for Structural Verification

Equivalent Uniform Thickness – The shell thickness t derived from the structural mass is:

$$t = \frac{M_{\text{shell}}}{\rho_{\text{mat}} \cdot A_{\text{total}} \cdot k_{\text{smear}}} \tag{E.15}$$

where:

- $\rho_{\text{mat}} = 2700\ \text{kg/m}^3$ (Al–Li 2195), [C]
- $A_{\text{total}} = 2\pi R L_{\text{struct}}$ is the total cylindrical surface area, [35]
- $k_{\text{smear}} = 1.15$ accounts for welds, flanges, and reinforcements. [35]

Stress Components – Axial stress due to thrust and bending:

$$\sigma_{\text{axial}} = \frac{P}{A}, \quad \sigma_{\text{bend}} = \frac{M}{Z} \tag{E.16}$$

where:

- P is the axial compressive force;
- M is the bending moment;
- $A = 2\pi R t$ is the cross-sectional area;
- $Z = \pi R^2 t$ is the section modulus.

Hoop stress from internal pressure: [14]

$$\sigma_{\text{press}} = \frac{pR}{2t} \tag{E.17}$$

Critical Buckling Stress (Cylindrical Shell) – For axial compression, This is [98]:

$$\sigma_{\text{cr}} = \gamma \cdot E \cdot \frac{t/R}{\sqrt{3(1-\nu^2)}} \tag{E.18}$$

where:

- $E = 69$ GPa is Young's modulus;
- $\nu = 0.33$ is Poisson's ratio;
- $\gamma = 0.40$ is the empirical knockdown factor for axial compression.

Shear Buckling Stress – For a ring-stiffened cylinder, the critical shear stress is:

$$\tau_{\text{cr}} = \gamma_{\text{shear}} \cdot K_s \cdot \frac{\pi^2 E}{12(1-\nu^2)} \left(\frac{t}{L}\right)^2, \qquad K_s = 0.85 \left(\frac{L^2}{Rt} \sqrt{1-\nu^2}\right)^{0.75} \tag{E.19}$$

where L is the ring spacing, $\gamma_{\text{shear}} = 0.75$ [98] and K_s is the shear-buckling coefficient.

Safety Factors – Safety factors are computed as:

$$\text{SF}_{\text{buckling}} = \frac{\sigma_{\text{cr}}}{\sigma_{\text{comp}}}, \quad \text{SF}_{\text{yield}} = \frac{F_{ty}/\text{SF}_{\text{req}}}{\sigma_{\text{tens}}}, \quad \text{SF}_{\text{shear}} = \frac{\tau_{\text{cr}}}{\tau} \tag{E.20}$$

where:

- $F_{\text{ty}} = 560$ MPa is the yield strength of Al–Li 2195; [82]

- $\mathrm{SF}_{\mathrm{req}} = 1.4$ is the required human-rated safety factor; [22]
- σ_{comp} and σ_{tens} are the maximum compressive and tensile stresses;
- τ is the applied shear stress.

Structural Verification Insights

Geometric Properties

Stage 1 (primary verification):

- Radius: $R = 1.70$ m;
- Thickness: $t = 12.35$ mm;
- Cross-sectional area: $A = 2\pi R t = 0.1319\ \mathrm{m}^2$;
- Section modulus: $Z = \pi R^2 t = 0.1121\ \mathrm{m}^3$.

Stress Components

Applied loads:

- Axial force: $P = 2.35$ MN (compression);
- Bending moment: $M = 5.63$ MN m;
- Internal pressure: $p = 320$ kPa [35].

Stress components:

$$\sigma_{\mathrm{axial}} = \frac{P}{A} = 17.82\ \mathrm{MPa} \tag{E.21}$$

$$\sigma_{\mathrm{bend}} = \frac{M}{Z} = 50.20\ \mathrm{MPa} \tag{E.22}$$

$$\sigma_{\mathrm{press}} = \frac{pR}{2t} = 22.02\ \mathrm{MPa} \tag{E.23}$$

Compression Side Verification (-R)

- **Applied compressive stress:**

$$\sigma_{\mathrm{comp}} = \sigma_{\mathrm{axial}} + \sigma_{\mathrm{bend}} - \sigma_{\mathrm{press}} = 46.00\ \mathrm{MPa} \tag{E.24}$$

- **Critical buckling stress** (NASA SP-8007 [98], with empirical knockdown factor for cylindrical shells $\gamma = 0.40$):

$$\sigma_{\mathrm{cr}} = \gamma \cdot E \cdot \frac{t/R}{\sqrt{3(1-\nu^2)}} = 122.6\ \mathrm{MPa} \tag{E.25}$$

- **Safety factor:**

$$\mathrm{SF}_{\mathrm{buckling}} = \frac{\sigma_{\mathrm{cr}}}{\sigma_{\mathrm{comp}}} = 2.67 \quad (> 1.4\ \text{required}) \tag{E.26}$$

Tension Side Verification (+R)

- **Applied tensile stress:**

$$\sigma_{\text{tens}} = -\sigma_{\text{axial}} + \sigma_{\text{bend}} + \sigma_{\text{press}} = 54.40 \text{ MPa} \tag{E.27}$$

- **Allowable yield stress:**

$$\sigma_{\text{yield,allow}} = \frac{F_{ty}}{\text{SF}_{\text{yield}}} = \frac{560 \text{ MPa}}{1.4} = 400.0 \text{ MPa} \tag{E.28}$$

- **Safety factor:**

$$\text{SF}_{\text{yield}} = \frac{\sigma_{\text{yield,allow}}}{\sigma_{\text{tens}}} = 7.35 \quad (> 1.0 \text{ required}) \tag{E.29}$$

Shear Buckling Verification

- **Ring-stiffened cylinder analysis** (NACA TN-3783 [99]):
- **Applied shear stress:**

$$\tau = \frac{V}{\pi R t} = \frac{1.40 \text{ MN}}{\pi \times 1.70 \text{ m} \times 0.01235 \text{ m}} = 21.22 \text{ MPa} \tag{E.30}$$

- **Critical shear stress** (with ring spacing $L = 0.85$ m):

$$Z = \frac{L^2}{Rt}\sqrt{1-\nu^2} = 32.0 \tag{E.31}$$

$$K_s = 0.85 Z^{0.75} = 11.56 \quad \text{(shear buckling coefficient)} \tag{E.32}$$

$$\tau_{\text{cr}} = \gamma_{\text{shear}} \cdot K_s \cdot \frac{\pi^2 E}{12(1-\nu^2)}\left(\frac{t}{L}\right)^2 = 128.47 \text{ MPa} \tag{E.33}$$

- **Safety factor:**

$$\text{SF}_{\text{shear}} = \frac{\tau_{\text{cr}}}{\tau} = 6.05 \quad (> 1.4 \text{ required}) \tag{E.34}$$

Appendix F

Detailed Modelling of Re-Entry Phase

Detailed Modelling of the Capsule Descent

This appendix provides a comprehensive description of the physical models, governing equations, numerical approaches, and design choices used to simulate the atmospheric descent of the capsule. In addition to the mathematical formulation, particular emphasis is placed on the technical justification of the selected parachute system and Thermal Protection System (TPS), including material selection, sizing criteria, and resulting mass breakdowns.

Reference Frames and Modelling Assumptions

To capture the dominant physical phenomena the following assumptions are adopted throughout the descent analysis:

- The motion is two-dimensional.
- The Earth is modeled as a perfect sphere.
- The capsule is treated as a point mass.
- Atmospheric properties depends on altitude and are obtained from a standard atmosphere model.
- Gravity varies with altitude according to a Newtonian law.
- Wind effects are neglected.
- A simplified control law maintains zero angle of attack during descent.
- The descent is divided into distinct phases using altitude-based event detection.
- Earth rotation effects are included through a ground-relative range correction.
- Parachute deployment and inflation are treated as discrete phase transitions.

These assumptions are standard for preliminary entry analyses and are consistent with validated entry simulation frameworks [100].

Equations of Motion

The capsule trajectory is described using spherical coordinates with respect to the Earth's centre. The state vector is defined as:

$$\mathbf{z} = [\theta,\ h,\ V,\ \gamma]^T$$

where:

- θ is the inertial longitude angle,
- h is the altitude above the Earth's surface,
- V is the velocity magnitude,

- γ is the flight-path angle measured from the local horizontal.

The radial distance is $r = R_E + h$, where R_E is the Earth radius.

The kinematic relations are:

$$\dot{\theta} = \frac{V\cos\gamma}{r} \tag{F.1}$$

$$\dot{h} = V\sin\gamma \tag{F.2}$$

The dynamic equations are given by:

$$\dot{V} = -\frac{D}{m} - g(h)\sin\gamma \tag{F.3}$$

$$\dot{\gamma} = \frac{L}{mV} + \left(\frac{V}{r} - \frac{g(h)}{V}\right)\cos\gamma \tag{F.4}$$

where D and L are the aerodynamic drag and lift forces, and $g(h)$ is the altitude-dependent gravitational acceleration:

$$g(h) = \frac{\mu}{(R_E + h)^2} \tag{F.5}$$

This formulation follows the classical entry dynamics equations presented in [100].

Atmospheric Model

Atmospheric properties (density ρ, temperature T, pressure p) are obtained from a standard Earth atmosphere model as functions of altitude. This approach is adequate for preliminary design, where the primary objective is to capture first-order effects of density variation on aerodynamic forces and heating.

The use of a tabulated standard atmosphere avoids the need for solving full thermochemical nonequilibrium flow while remaining consistent with the assumptions of engineering-level aerothermal correlations [101].

Aerodynamic Model

Aerodynamic Forces

The aerodynamic drag and lift forces are computed as:

$$D = \frac{1}{2}\rho V^2 C_D S_{\text{ref}} \tag{F.6}$$

$$L = \frac{1}{2}\rho V^2 C_L S_{\text{ref}} \tag{F.7}$$

where C_D and C_L are the drag and lift coefficients, respectively, and S_{ref} is the reference area.

For blunt-body capsules, lift is typically small compared to drag. Nevertheless, the general formulation is retained for completeness and numerical robustness.

Ballistic Coefficient Formulation

To improve numerical stability, aerodynamic deceleration is expressed in terms of the ballistic coefficient:

$$\beta = \frac{m}{C_D S_{\text{ref}}} \tag{F.8}$$

leading to:

$$\frac{D}{m} = \frac{1}{2}\frac{\rho V^2}{\beta} \tag{F.9}$$

This formulation highlights the dominant role of mass-to-area ratio in entry dynamics and is widely used in preliminary capsule design studies [102].

Aerothermal Modelling

Stagnation-Point Heating

Thermal loads during atmospheric re-entry are estimated using engineering-level correlations suitable for preliminary design. The resulting convective heat-flux time history is then used as the boundary condition for a one-dimensional transient Thermal Protection System (TPS) model. This provides a direct coupling between trajectory, aerothermal environment, and structural temperature constraints, enabling preliminary sizing of the heat shield while minimizing added mass.

The convective heat flux at the stagnation point is computed using an engineering implementation of the Fay–Riddell laminar boundary-layer theory for blunt bodies in hypersonic flow [40]. In the present model, the stagnation-point heat flux is expressed as:

$$\dot{q}_{\mathrm{conv}} = 0.57\,\mathrm{Pr}^{-0.6}\sqrt{\rho_e \mu_e}\sqrt{\left(\frac{dU_e}{dx}\right)_0}\, c_p (T_{ad} - T_w) \tag{F.10}$$

where:

- ρ_e and μ_e are density and viscosity at the boundary-layer edge,
- Pr is the Prandtl number,
- c_p is the specific heat at constant pressure,
- T_{ad} is the adiabatic wall temperature,
- T_w is the wall temperature.

This formulation is derived from the original theory developed by Fay and Riddell [40] and remains a reference standard for stagnation-point heating estimation.

Velocity Gradient at the Stagnation Point

The stagnation-line velocity gradient is approximated as:

$$\left(\frac{dU_e}{dx}\right)_0 \approx \frac{U_{\mathrm{scale}}}{R_n} \tag{F.11}$$

with

$$U_{\mathrm{scale}} = \sqrt{\frac{2(p_0 - p_\infty)}{\rho_e}} \tag{F.12}$$

where R_n is the nose radius. This formulation provides a physically consistent scaling of the stagnation flow field and avoids dimensional inconsistencies present in simpler approximations.

Wall Temperature and Radiative Equilibrium

A first-order estimate of the wall temperature is obtained by assuming radiative equilibrium between convective heating and surface radiation:

$$\dot{q}_{\text{conv}} = \varepsilon \sigma T_w^4 \tag{F.13}$$

which yields:

$$T_w = \left(\frac{\dot{q}_{\text{conv}}}{\varepsilon \sigma} \right)^{1/4} \tag{F.14}$$

where ε is the surface emissivity and σ is the Stefan–Boltzmann constant.

Compared to purely velocity-based correlations, the Fay–Riddell model provides a more physically representative description of stagnation-point heating by explicitly incorporating thermodynamic and transport properties of the high-temperature gas.

Total Heat Load

The total heat load is computed by time integration:

$$Q = \int_0^{t_f} \dot{q}_{\text{conv}}(t)\, dt \tag{F.15}$$

which provides a key metric for TPS material selection and thickness sizing.

Parachute Analysis

Parachute System Architecture and Redundancy

The recovery system is modelled as a two-stage parachute architecture consisting of a drogue parachute followed by a main parachute. For crewed-mission robustness, redundancy is explicitly included at system level:

- One nominal drogue parachute plus one backup drogue.
- One nominal main parachute plus one backup main parachute.

Only one drogue and one main parachute are required for nominal operation; the redundant units provide fault tolerance at system level and are included in the mass budget.

Parachute Sizing

The main parachute is preliminarily sized to meet a required terminal descent velocity V_{term} at sea level. Assuming equilibrium between weight and drag under terminal conditions [103, 104]:

$$mg = \frac{1}{2} \rho_{SL} V_{\text{term}}^2 C_{D0} S_0 \tag{F.16}$$

the required reference area is obtained as:

$$S_0 = \frac{mg}{\frac{1}{2} \rho_{SL} V_{\text{term}}^2 C_{D0}} \tag{F.17}$$

An equivalent canopy diameter is then computed assuming a circular parachute geometry. The drogue parachute area is defined as a fixed fraction of the main canopy area, consistent with common recovery-system design practice.

Inflation Model and Reefing

Parachute inflation is modelled through a gradual increase of the effective drag area according to:

$$C_D S(t) = C_{D0} S_0 \left(\frac{t}{t_f} \right)^b \tag{F.18}$$

where t_f is the canopy filling time and b is an inflation exponent dependent on parachute type. To limit opening loads and peak decelerations, both drogue and main parachutes incorporate reefing. Reefing is modelled as a two-stage process consisting of:

- an initial reefed configuration with reduced effective area, and
- a full-inflation stage following reefing-line release after a prescribed delay.

This approach enables controlled deployment over a wide range of dynamic pressures and is consistent with crewed recovery system design standards.

The estimated parachute system mass, including redundancy, is summarised in Table F.1.

Table F.1: Parachute mass estimate (circular slotted), including redundancy.

Component	**Mass per chute [kg]**	**Count (incl. redundancy)**
Main parachute	153.5	2
Drogue parachute	1.5	2
Total parachute system mass	310.2 kg	

Final Landing Phase and Use of Retro-Rockets.

For terrestrial landings, an additional final deceleration stage is commonly implemented using solid-propellant retro-rockets to further reduce the vertical descent velocity immediately prior to ground contact. This approach has been successfully employed in crewed capsule recovery systems, most notably in the Soyuz descent module, where a set of small, downward-facing solid motors is mounted on the capsule base [105, 106].

In such systems, the retro-rockets are ignited a few meters above the ground following the activation of mechanical landing probes, providing a short-duration impulse that reduces the vertical descent velocity from approximately 8 m/s under the main parachute to about 2 m/s at touchdown [42]. This final braking stage significantly limits impact loads transmitted to the capsule structure and crew.

Due to their extremely short burn time and activation at very low altitude, the contribution of the retro-rockets to the overall descent trajectory, aerodynamic loads, and thermal environment is negligible. Consequently, their effect is not explicitly included in the trajectory integration, and their function is treated as a localized landing-load mitigation system rather than as an active phase of the descent dynamics.

Thermal Protection System Modelling

TPS Physical Model

The TPS is modelled as a one-dimensional multilayer thermal system normal to the capsule forebody surface, consisting of:

- an external non-ablative TPS layer

- an internal structural layer representing the pressure vessel or load-bearing support structure.

Heat transfer is governed by transient one-dimensional conduction. Lateral heat transfer is neglected, which is acceptable for a preliminary stagnation-point analysis. Material properties are assumed constant and isotropic.

TPS Thickness Selection

The TPS thickness is selected to satisfy two primary thermal constraints:

1. maximum allowable surface temperature,
2. maximum allowable back-face temperature of the structural shell.

TPS Mass Estimation

The TPS mass is estimated assuming uniform thickness over the capsule heat-shield area:

$$m_{\text{TPS}} = \rho_{\text{TPS}} S_{\text{shield}} L_{\text{TPS}}. \tag{F.19}$$

TPS Governing Equation

The TPS is modelled using a one-dimensional transient heat conduction equation:

$$\rho c_p \frac{\partial T}{\partial t} = \frac{\partial}{\partial x}\left(k \frac{\partial T}{\partial x}\right)$$

where k is the thermal conductivity, ρ the density, and c_p the specific heat of the TPS material.

TPS Selection

Based on the predicted aerothermal environment and the resulting heat-load and temperature constraints, a non-ablative Thermal Protection System based on FRCI-12 was selected for the capsule forebody. This material provides an optimal trade-off between thermal performance and mass at preliminary design level, offering low density, low thermal conductivity, and high allowable surface temperature. The TPS thickness was sized to ensure that both the maximum surface temperature and the back-face temperature of the underlying aluminium structure remain below their respective allowable limits throughout the descent.

Boundary Conditions

At the hot face:

$$-k \left.\frac{\partial T}{\partial x}\right|_{x=0} = \dot{q}_{\text{conv}} - \varepsilon \sigma T^4$$

At the back face:

$$-k \left.\frac{\partial T}{\partial x}\right|_{x=L} = h_{\text{int}}(T_{\text{back}} - T_{\text{cabin}})$$

This formulation allows direct coupling between trajectory heating and internal structural constraints.

Justification of the 1D Model

A one-dimensional TPS model is adequate at preliminary design level because the dominant heat transfer occurs in the direction normal to the surface. Multidimensional effects are negligible for axisymmetric capsules with relatively uniform heating near the stagnation region [107].

Numerical Implementation

The complete descent problem is solved using a time-marching numerical integration scheme. Event detection is used to trigger parachute deployment, reefing line cutting, and phase transitions. This modular approach allows efficient trade studies and sensitivity analyses.

Normal Load Factor During Descent

The normal load factor is defined as the longitudinal deceleration experienced by the capsule, normalized by the standard gravitational acceleration:

$$n(t) = -\frac{1}{g_0}\frac{dV}{dt}, \tag{F.20}$$

where V is the capsule velocity along the trajectory and g_0 is the standard gravitational acceleration at sea level. The negative sign reflects the decelerative nature of the aerodynamic and parachute-induced forces acting on the capsule during descent.

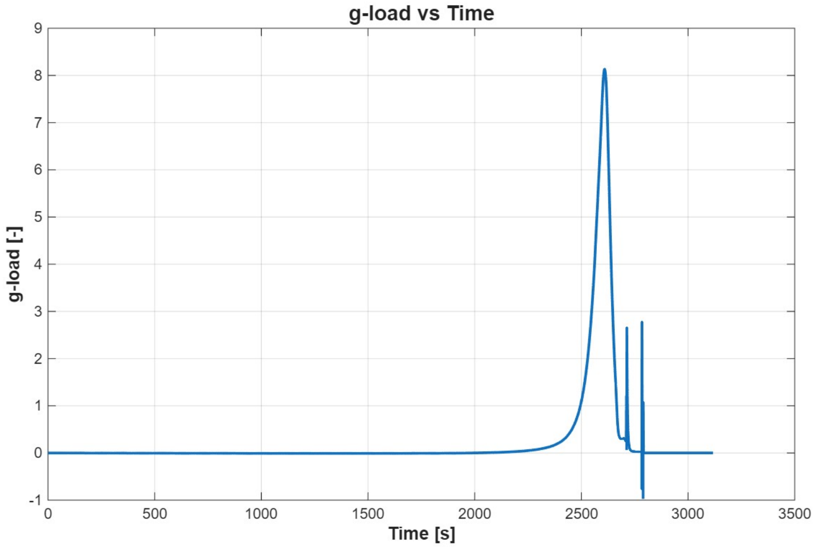

Figure F.1: Normal load factor (g-load) versus time.

The resulting time history of the normal load factor is shown in Figure F.1. The g-load profile reflects the combined contribution of aerodynamic deceleration during the high–dynamic-pressure phase of atmospheric re-entry and the transient loads associated with parachute deployment and inflation. The peak load occurs during the atmospheric braking phase, when high velocity coincides with rapidly increasing atmospheric density. Lower-amplitude, short-duration load transients are observed during parachute inflation, whose magnitude is effectively mitigated through reefed and staged deployment. Overall, the predicted g-load levels remain within acceptable limits for crewed return profiles, confirming that the adopted entry trajectory and parachute sequence provide adequate mitigation of mechanical loads during descent.

Appendix G

Aerodynamics Further Insights

Aerodynamic Elements

Saddle

The saddle is a structure which has the main purpose of sustaining the wing from the structural point of view and to transmit the forces generated to the launcher body, while trying to minimize its own drag contribute. The study of aerodynamics, forces and stresses on this structure was not considered in this analysis since it goes above our capacities and our scope.

Wing-body Fillet

The wing-body fillet is an active aerodynamic element whose function is to minimize interference drag and ensure attached shock waves at hypersonic regimes, while preserving the stability induced by the vortexes at high angles of attack [50, 53]. In order to replicate this behavior a these parameter have been chosen for our configuration:

Table G.1: Geometric optimization of the wing-body fillet.

Geometric Parameter	Value	Optimization Process
Sweep Angle (Λ_{fillet})	75°	High sweep angle chosen to generate vortex lift and to stabilize the flux at high angles of attack [108].
Ramp Angle (θ)	7.13°	Optimized for the hypersonic regime. The value is well below the limit for shock wave detachment ($\theta_{\text{max}} \approx 12°$–$15°$) [50], granting attached shock waves and reducing wave drag and thermal impact on the wing leading edge.
Total Length (L)	2.00 m	Available space on the interstage surface.

Missile DATCOM Software

The software utilizes the Component Buildup Method, where the aerodynamic forces on the nose, body, and lifting surfaces are calculated separately and then superimposed, accounting for interference effects. For the supersonic regime, DATCOM employs the Second-Order Shock Expansion Method (SOSE) for the fuselage and theoretical-experimental databases for the lifting surfaces[47–49].

Modified Newtonian Theory

Aerodynamic performance coefficient have been estimated through a panel method analysis that takes as an input surface triangulation (STL) of the launcher and utilizes the Modified Newtonian Theory in order to compute the Pressure Coefficient that acts on each panel:

$$C_p = C_{p_{\max}} \sin^2(\theta) \tag{G.1}$$

A critical parameter in this formulation is the stagnation pressure coefficient $C_{p,\text{max}}$, in this analysis it has been estimated using the Rayleigh-Pitot formula assuming a calorically perfect gas model.

$$C_{\text{p,max}} = \frac{2}{\gamma_{gas} M_\infty^2} \left[\left(\frac{(\gamma_{gas}+1)^2 M_\infty^2}{4\gamma_{gas} M_\infty^2 - 2(\gamma_{gas}-1)} \right)^{\frac{\gamma_{gas}}{\gamma_{gas}-1}} \left(\frac{1-\gamma_{gas}+2\gamma_{gas} M_\infty^2}{\gamma_{gas}+1} \right) - 1 \right] \tag{G.2}$$

Although the flight trajectory covers the hypersonic regime (from Mach 5 to Mach 10) where high temperature effects modify the gas behaviour, and so the calorically perfect gas assumption ($\gamma_{gas} = 1.4$), this formulation still provides an efficient approximation for our preliminary conceptual design.

Body Correction

The semi-empirical method proposed by Allen and Perkins [51] and refined by Jorgensen [52] states that the normal force acting on a slender body (C_N) is the superimposition of two components: a term derived from potential flow theory and a term resulting from viscous separation:

$$C_N = \underbrace{\frac{S_b}{S_{\text{ref}}} \sin(2\alpha)\cos\left(\frac{\alpha}{2}\right)}_{\text{Potential Term}} + \underbrace{\eta C_{d,c} \frac{S_{\text{plan}}}{S_{\text{ref}}} \sin^2(\alpha)}_{\text{Viscous Cross-Flow Term}} \tag{G.3}$$

The first component depends on the variation of the cross-sectional area ($\partial S/\partial x$), it dominates force generation on the nose and on the boat-tail sections but it's almost null for the cylindrical body where where the cross-section remains constant($\partial S/\partial x = 0$). Moreover the contribution of the nose is already considered by the Modified Newtonian Theory solver used in the analysis. In order to avoid double-counting of forces on the nose, only the viscous term has been considered for the cylindrical body. This term takes into account the effects of boundary layer separation on the leeward side of the body, where it forms vortexes that generates a normal force proportional to the square of the angle of attack. The final correction is:

$$C_{N_{\text{body}}} = \eta \cdot C_{d,c} \cdot \frac{S_{\text{plan}}}{S_{\text{ref}}} \cdot \sin^2(\alpha) \tag{G.4}$$

where $\eta \approx 0.65$ is the cross-flow efficiency factor for finite cylinders, and $C_{d,c} \approx 1.2$ represents the cross-flow drag coefficient. This correction has been applied due to the low accuracy of the Modified Newtonian Theory in capturing the force generated by the long cylindrical fuselage at low angles of attack.

Wing Correction

The Modified Newtonian Theory fails to capture the whole contribute to the total force given by the wing surface, in particular at low angle of attack. This is due to the fact that it ignores the pressure difference between the suction side (expansion waves) and the pressure side (shock wave) which is the main contribute to the force generated by these aerodynamic surfaces [50]. Nielsen [53] illustrates how, for thin wings in supersonic and hypersonic regimes, the force generated by these surfaces follows a linear trend:

$$C_{L\alpha} = \frac{4}{\sqrt{M^2-1}} \tag{G.5}$$

Although the linear theory term, that was superimposed to the Modified Newtonian Fluid contribute, loses accuracy at high mach numbers, it remains sufficient for the scope of this conceptual phase design, providing robust and plausible approximate results.

Drag Corrections

Since the Panel Method based on the Modified Newtonian Theory only estimates the main contribution to the drag ($C_{D,wave}$), two terms has been superimposed to the results in order to estimate the total Drag Coefficient:

$$C_{D,total} = C_{D,wave} + C_{D,friction} + C_{D,base} \tag{G.6}$$

Friction Drag

Since the Modified Newtonian Theory solver is purely inviscid, a semi-empirical correction has to be applied in order to take into account the skin friction drag. It is a dominant component at lower altitudes but it's still not negligible until the launcher crosses the Kármán Line (100 km). This contribute is due to to the shear forces developed in the boundary layer attached to the vehicle surface. The contribution to the total Drag Coefficient is computed by scaling the average skin friction coefficient (C_f) by the launcher's wetted surface area (S_{wet}):

$$C_{\text{D, friction}} = C_f \cdot \frac{S_{\text{wet}}}{S_{\text{ref}}} \tag{G.7}$$

To determine the compressible skin friction coefficient C_f, the Van Driest II[54] method was utilized, the Kármán-Schoenherr relation is solved taking into account the Reynolds number based on the launcher length (Re_L) and the Van Driest transformation factors (F_c and F_{Re}):

$$\frac{0.242}{\sqrt{C_f \cdot F_c}} = \log_{10}\left(Re_L \cdot C_f \cdot F_{\text{Re}}\right) \tag{G.8}$$

Base Drag

The panel method typically assumes free-stream or no pressure on the shadowed panels, failing to capture the full suction effect in this region, characterized by low pressure and recirculating flows. In order to take into account also this effect a semi-empirical correlation based on the Hoerner drag analysis[55] has been applied. For supersonic and hypersonic missiles, the base drag coefficient decreases as the Mach number increases:

$$C_{\text{D, base}} \approx \frac{1}{M^2} \tag{G.9}$$

This relationship approximately models the rapid decrease in base pressure influence at high Mach numbers.

Results Analysis and Graphs

The evolution of the Lift Coefficient as a function of Mach number for different angles of attack is illustrated in Fig. G.3. The reference surface used to compute the coefficient is the main body section (conventional missile standard). The results shows physically consistent behaviors:

- **Compressibility Effects:** In the subsonic range, C_L increases due to compressibility (Prandtl-Glauert effect)[109].

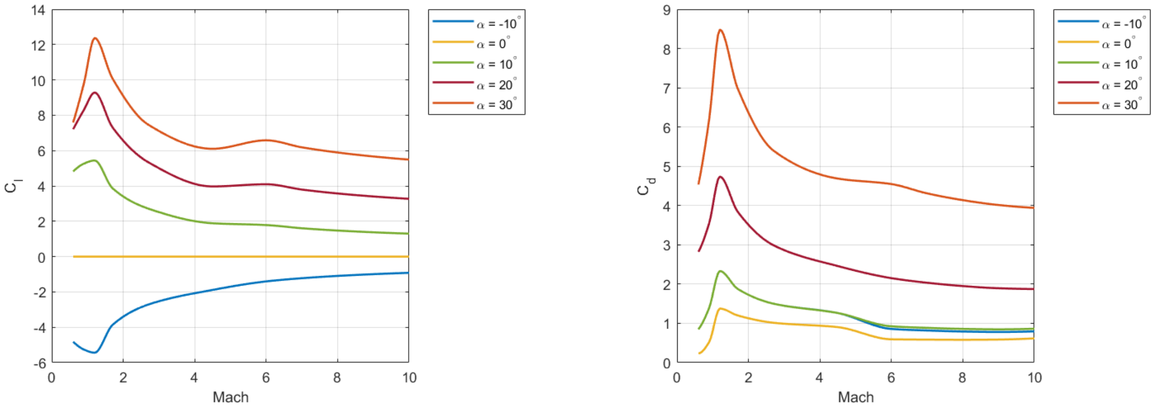

Figure G.1: Interpolated C_l vs. Mach

Figure G.2: Interpolated C_d vs. Mach

Figure G.3: Interpolated Aerodynamic Coefficients

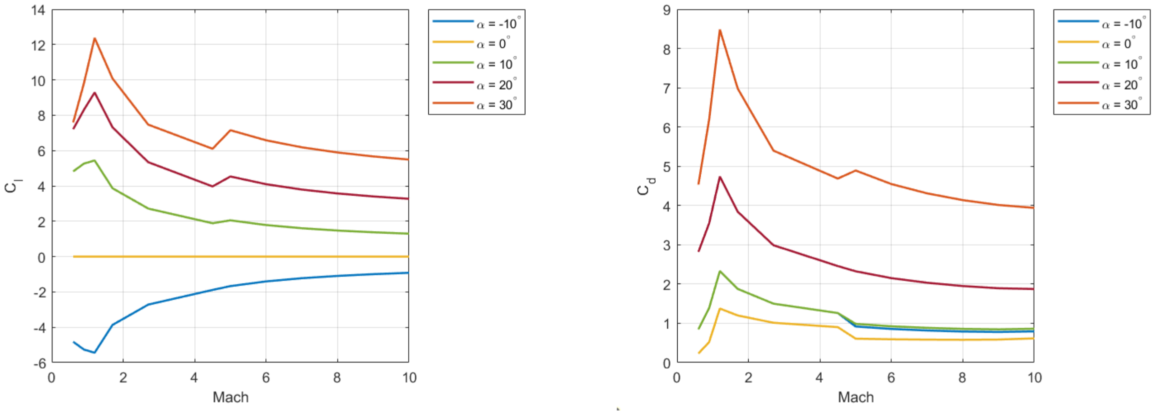

Figure G.4: C_l vs. Mach

Figure G.5: C_d vs. Mach

Figure G.6: Non Interpolated Aerodynamic Coefficients.

- **Supersonic/Hypersonic Decay:** Beyond Mach 1.2, the lift efficiency progressively decreases. The analysis successfully captures the asymptotic decay at high Mach numbers, accordingly to the Independence Mach Principle [50].

Second Stage Graphs

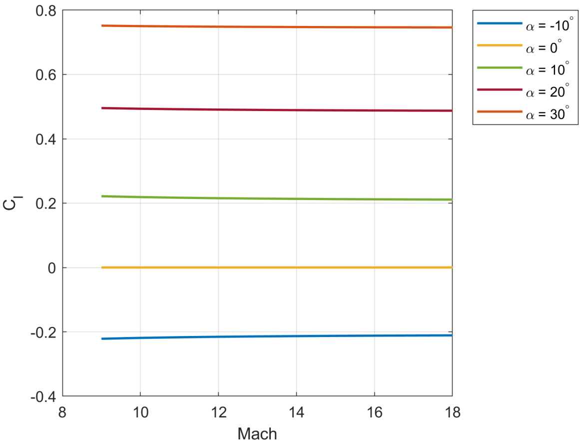

Figure G.7: Second Stage C_l vs. Mach

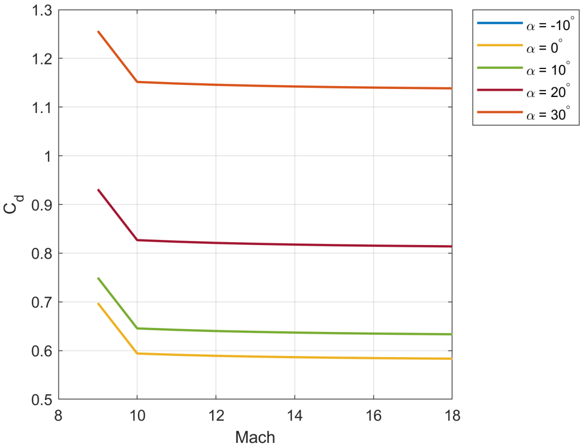

Figure G.8: Second Stage C_d vs. Mach

Capsule Aerodynamics Details

A multi-regime approach has been adopted to estimate the values of the Drag Coefficient during the capsule descent trajectory because no single numerical method is accurate enough to compute the aerodynamic coefficient values in such a wide range of different airflow physics conditions. The trajectory has been divided into four regimes considering the local Knudesn number (Kn) and Mach number (M). Since the analysis assumes a constant angle of attack of $\alpha = 180°$ and the capsule presents an axisymmetric geometry, the Lift Coefficient has been approximated to zero throughout the whole descent profile. The analysis focuses on the Drag Coefficient.

Regime 1: Free Molecular Flow (200 km – 140 km)

The Knudsen number in this region is large $(Kn > 10)$, this means that the free path of the molecules is larger the characteristic length of the capsule [110]. Molecules here do not interact between each other, preventing the formation of shockwaves. In this Free Molecular Flow regime the analysis considers a constant Drag Coefficient, relying on the the hypersonic rarefied flow analysis performed on the Orion capsule by [56]:

$$C_D \approx 2.2 \quad (\text{for } h > 140 \text{ km}) \tag{G.10}$$

This is the limit value for a blunt body in high altitude atmospheric condition (as detailed in the reference study [56]).

Regime 2: Transition Regime (140 km – 100 km)

This is the region of transition between Free Molecular Flow and Continuum Flow Mechanics. In order to estimate the value of the Drag Coefficient through this complex transition phase without time consuming CFD simulations, a mathematical bridging function was implemented. The molecular value $(C_{D_{mol}})$ and the continuum Newtonian value $(C_{D_{newton}})$ have been smoothly interpolated through a sine-squared weighing function (w):

$$w(h) = \sin^2\left(\frac{h-100}{140-100} \cdot \frac{\pi}{2}\right) \qquad C_D(h) = w(h) \cdot C_{D_{mol}} + (1 - w(h)) \cdot C_{D_{newton}} \tag{G.11}$$

Regime 3: Hypersonic Continuum (100 km – 50 km)

In this region, below the Kármán Line, the flow behaves like a Continuum Fluid. The capsule travels at high hypersonic speed, causing a strong detached bow shock to form near the heat shield. In order to characterize the Drag Coefficient in this region, the same Panel Method used to study the aerodynamics of the Second Stage (based on the Modified Newtonian Theory) has been implemented.

Blending Zone (50 km – 40 km)

To prevent discontinuities between the Panel Method results and the database values, a blending zone has been implemented between 40 km and 50 km. A weighted interpolation enables a smooth transition between the two regimes.

Regime 4: Supersonic to Subsonic (40 km – 0 km)

Below 40 km the capsule goes through the supersonic transonic and subsonic regime before reaching sea level. The Modified Newtonian Theory loses accuracy in these regimes, especially in capturing the transonic drag rise. In order to ensure the accuracy of the results in this region, experimental data form the Orion Module Aerodynamic Database were utilized [57].

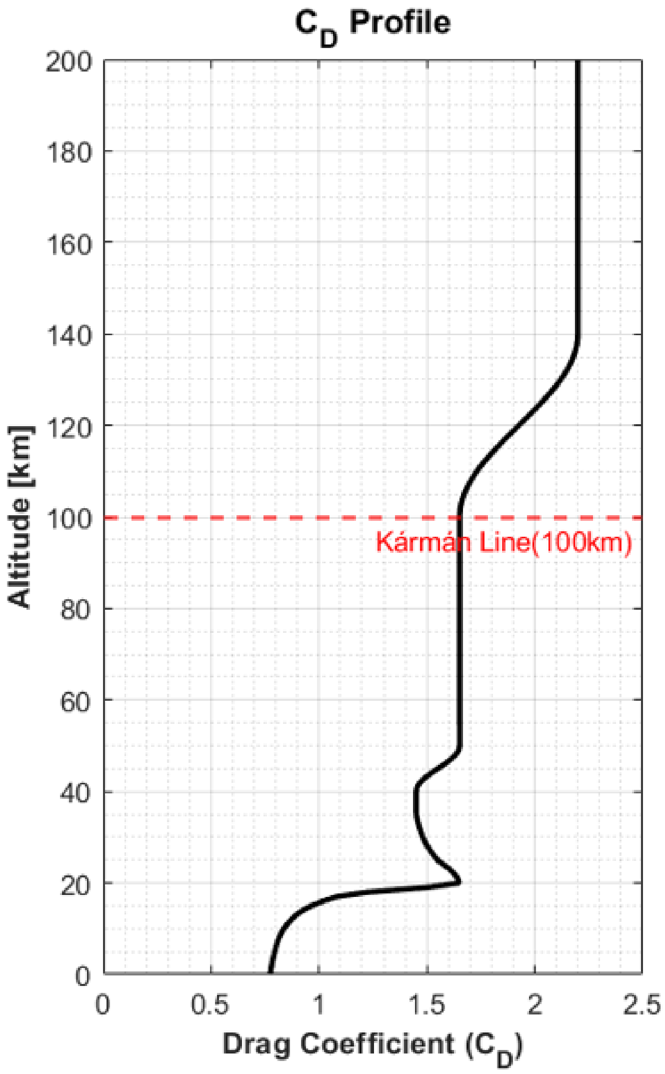

Figure G.9: Capsule C_D vs altitude

Appendix H

Ascent Phase Thermal Loads Insights

Convective Heat Flux Modelling at the Stagnation Point

Convective heating at the capsule stagnation point is modelled using an engineering-level formulation based on classical convective heat-transfer theory. The heat flux is expressed as a function of the convective heat-transfer coefficient and the temperature difference between the adiabatic wall temperature and the actual wall temperature. This approach provides a physically consistent coupling between the aerothermal environment and the Thermal Protection System (TPS) response while maintaining low computational cost.

The stagnation-point convective heat flux is written as

$$\dot{q}_{\text{conv}} = h_c\,(T_{aw} - T_w)\,, \tag{H.1}$$

where h_c is the convective heat-transfer coefficient, T_{aw} is the adiabatic wall temperature, and T_w is the wall temperature obtained from the TPS thermal model.

The adiabatic wall temperature represents the temperature that would be attained by the wall in the absence of heat transfer and is computed using a recovery-factor formulation:

$$T_{aw} = T_\infty \left(1 + r\frac{\gamma - 1}{2} M^2\right), \tag{H.2}$$

where T_∞ is the freestream temperature, γ is the ratio of specific heats, M is the local Mach number, and r is the recovery factor. The recovery factor accounts for viscous dissipation within the boundary layer and depends on the flow regime. For laminar flow, $r = \mathrm{Pr}^{1/3}$, while for turbulent flow $r = \mathrm{Pr}^{0.4}$, with Pr denoting the Prandtl number.

The convective heat-transfer coefficient is evaluated using a Nusselt-number correlation of the form

$$\mathrm{Nu} = 2 + \left(0.4\,\mathrm{Re}^{1/2} + 0.06\,\mathrm{Re}^{2/3}\right)\mathrm{Pr}^{0.4}, \tag{H.3}$$

which is applicable over a wide range of Reynolds and Prandtl numbers and is commonly used in preliminary aerospace thermal analyses.

The Reynolds number is defined as

$$\mathrm{Re} = \frac{\rho_\infty V L}{\mu}, \tag{H.4}$$

where ρ_∞ is the freestream density, V is the capsule velocity, μ is the dynamic viscosity evaluated at a film temperature, and $L = 2R_n$ is a characteristic length based on the capsule nose radius R_n.

The convective heat-transfer coefficient is then obtained from

$$h_c = \frac{\mathrm{Nu}\,k}{L}, \tag{H.5}$$

where k is the thermal conductivity of the gas, computed consistently from the dynamic viscosity and Prandtl number through standard kinetic-theory relations.

At high altitudes, where the flow progressively departs from the continuum regime, rarefaction effects become non-negligible. These effects are accounted for through a Knudsen-number-based correction applied to the convective heat-transfer coefficient. The local Knudsen number is defined as

$$\mathrm{Kn} = \frac{\lambda}{R_n}, \tag{H.6}$$

where λ is the molecular mean free path. As Kn increases beyond the continuum limit, a smooth attenuation function is applied to reduce the effective convective heat-transfer coefficient, ensuring a physically realistic transition toward the free-molecular regime.

The convective heat flux is evaluated at each trajectory time step and is coupled with the TPS thermal model through the wall temperature T_w. This coupling enables a self-consistent aero–thermal interaction in which the wall temperature directly influences the convective heat flux, and vice versa. The resulting stagnation-point temperature and heat-flux histories are shown in Figure 7.4, illustrating the evolution of the thermal environment throughout the ascent phase.

Appendix I

Public Risk and Uncertainty Analysis Details

Expected Casualty (EC) Framework and Compliance Calculation

Public risk for launch and re-entry operations is regulated through the *Expected Casualty* (EC) metric. Under *14 CFR §450.101*, operators must demonstrate that the expected number of public casualties satisfies

$$EC < 1 \times 10^{-4}. \tag{I.1}$$

This criterion constrains the overall public risk and does not directly impose a limit on the vehicle failure probability [60, 111, 112].

A common formulation is

$$EC = \sum_{i,j} EC_{ij} = \sum_{i,j} P_{ij} A_c \frac{N_p}{A_p}, \tag{I.2}$$

where:

- A_c is the effective casualty area (m^2);
- N_p/A_p is the population density over the affected footprint (people/m^2);
- P_{ij} is the probability that hazardous debris (or the vehicle) impacts population cell j for failure mode/fragment i.

For preliminary sizing studies, it is common to aggregate the debris field into a single effective casualty area and interpret P_{ij} as a single effective failure probability P_{fail} over the relevant footprint. On top of this, since the ignition of the first engine will take place over the Pacific Ocean, we may consider the expected casualty risk for take off to be null. Under these simplifying assumptions, the EC requirement yields an allowable failure probability upper bound:

$$P_{\text{fail,max}} \approx \frac{EC_{\max}}{A_c\,(N_p/A_p)}. \tag{I.3}$$

In this work, the following scenario-level assumptions were adopted:

- Effective casualty area $A_c \approx 290\ \mathrm{m}^2$ (capsule mass ~ 6.5 t, conservative exposed footprint);
- Mean population density 6.1 people/km^2 representative of the *Pontes e Lacerda* region.

Using these values and enforcing $EC_{\max} = 10^{-4}$ results in the main-text value

$$P_{\text{fail,max}} = 5.65\%. \tag{I.4}$$

This value is a regulatory **upper bound** compatible with public safety compliance, not a recommended design target. In sparsely populated regions and for limited casualty area, relatively large values of P_{fail} may still satisfy the EC constraint because the FAA regulates the product of probability and consequence (exposure), rather than probability alone [111, 112].

Empirical Reliability Benchmark from Soyuz Flight Heritage

To contextualize the EC-derived limit, historical reliability data from the Soyuz descent module were used as an operational benchmark. Soyuz represents a close analogue to a modern blunt-body capsule system due to its:

- ablative thermal protection system,
- ballistic stability during entry,
- parachute-based terminal descent,
- land touchdown operations in sparsely populated regions.

Since the last fatal Soyuz re-entry accident (Soyuz 11 in 1971), approximately $N \approx 140$ crewed re-entries have been completed with no observed catastrophic failures during atmospheric entry, parachute deployment, or landing [61, 62]. While off-nominal ballistic re-entries have occurred, these events did not result in loss of crew.

Assuming independent trials and zero observed catastrophic failures, a conservative upper bound on the catastrophic failure probability can be estimated via the binomial "rule of three":

$$P_{\text{fail,cat}} < \frac{3}{N} \qquad \text{(95\% confidence).} \tag{I.5}$$

For $N \approx 140$, this gives

$$P_{\text{fail,cat}} < 2.1\% \qquad \text{(95\% confidence).} \tag{I.6}$$

This estimator is widely used in reliability engineering for rare, unobserved events [113].

Therefore, the empirically inferred upper bound ($\sim 2.1\%$) lies below the EC-derived permissible upper bound (5.65%). Thus, the EC constraint is not in conflict with demonstrated capsule heritage; rather, it is permissive under the assumed low-density operating environment.

Uncertainty Modeling for Ascent Parameters

The nominal ascent trajectory assumes ideal (deterministic) parameter values. For robustness assessment, uncertainty was introduced in the dominant propulsion and mass parameters commonly treated in preliminary launch-vehicle analyses [63, 114–116]:

- specific impulse I_{sp},
- thrust T,
- initial mass M_0,

applied to both Stage 1 and Stage 2.

Sampling Method: Latin Hypercube Sampling (LHS) Latin Hypercube Sampling (LHS) was adopted rather than standard Monte Carlo sampling because, for a given sample size N, LHS typically provides reduced estimator variance for mean and quantile estimates by stratifying each marginal distribution into equiprobable intervals and forcing one sample per stratum [64, 65]. This improves marginal coverage and stabilizes tail estimates (e.g., P5/P95), which is particularly useful when assessing dispersion and performance envelopes.

In the present implementation, Stage 1 and Stage 2 parameter uncertainties were treated as independent marginals (i.e., no cross-stage correlation was imposed unless explicitly stated otherwise).

Specific Impulse Uncertainty For each stage, I_{sp} was modeled as a normal distribution centered at the nominal value with a standard deviation of

$$\sigma_{I_{sp}} = 0.01\, I_{sp,\text{nom}}, \tag{I.7}$$

truncated at $\pm 3\sigma$. This corresponds to a mature-engine assumption and is consistent with typical instrumentation/error-budget magnitudes and performance repeatability reported for developed propulsion systems [63, 114].

Mass Uncertainty A secondary multiplicative mass perturbation was introduced to represent integration tolerances, propellant loading resolution, and bookkeeping effects not captured by I_{sp} uncertainty alone. The adopted dispersion was

$$\sigma_{M_0} = 0.005\, M_{0,\text{nom}}, \tag{I.8}$$

also truncated at $\pm 3\sigma$ [63, 116].

Thrust Uncertainty Thrust uncertainty for each stage was modeled with

$$\sigma_T = 0.01\, T_{\text{nom}}, \tag{I.9}$$

truncated at $\pm 3\sigma$, consistent with conservative hot-fire repeatability and measurement uncertainties [114, 115].

Trajectory Propagation and Interpretation of Asymmetric Dispersion

For each sampled parameter set, the ascent equations of motion were integrated using the same open-loop guidance law (nominal pitch program) adopted for the baseline trajectory. This isolates the effect of parametric uncertainty while preserving guidance consistency across realizations.

The stochastic trajectory ensemble remains of the same order of magnitude as the nominal trajectory but exhibits a pronounced skew toward reduced apogee and downrange distance. This behavior is physically expected in fixed-guidance ascent because:

- the nominal guidance law is near-optimal only for the nominal vehicle, and becomes suboptimal for off-nominal performance realizations;
- off-nominal vehicles (especially low-thrust/high-mass/low-I_{sp} cases) spend longer in dense atmosphere and accrue larger gravity and drag losses;
- nonlinear ascent physics (e.g., $D \propto v^2$ and coupled thrust–mass-flow–I_{sp} behavior) cause symmetric input perturbations to map to asymmetric output dispersion [28, 117–119].

Accordingly, the resulting set of trajectories should be interpreted as a robustness envelope about the nominal ascent rather than a symmetric uncertainty cloud. This interpretation is consistent with established uncertainty quantification practice for nonlinear systems [120].

Figures: Input Distributions and Stochastic Trajectory Dispersion

Figure I.1 presents the sampled input distributions used for uncertainty propagation. Figures I.2–I.2c illustrate representative trajectory dispersion in state histories, planar trajectories, velocity magnitude, and flight-path angle.

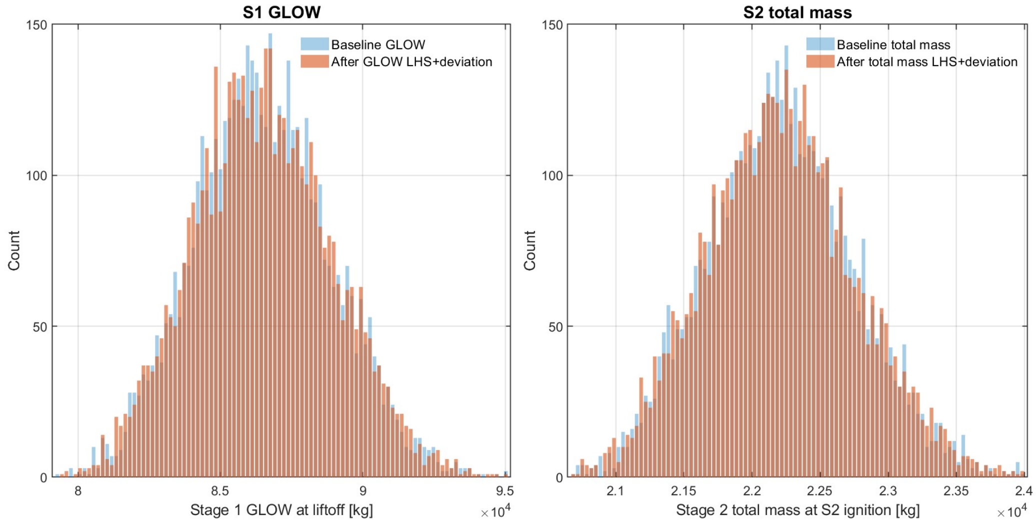

(a) Stage 1 GLOW and Stage 2 total mass distributions before and after residual LHS-based deviation.

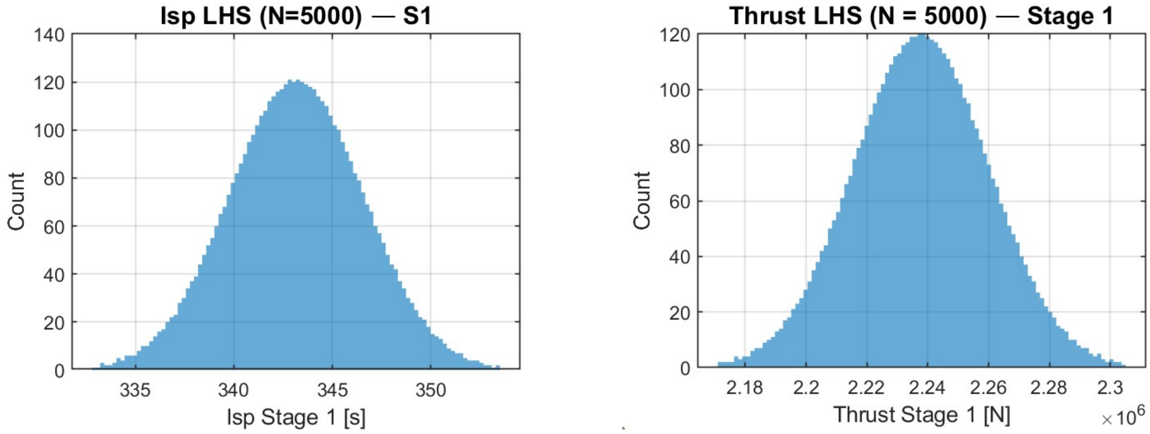

(b) Stage 1 specific impulse $I_{sp,1}$.

(c) Stage 1 thrust T_1.

(d) Latin Hypercube Sampling distributions for Stage 1 propulsion parameters.

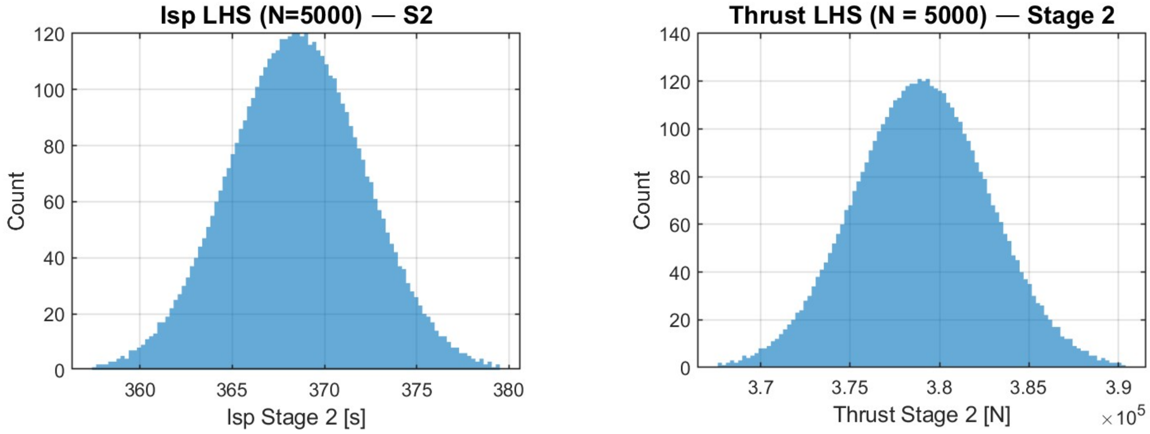

(e) Stage 2 specific impulse $I_{sp,2}$.

(f) Stage 2 thrust T_2.

(g) Latin Hypercube Sampling distributions for Stage 2 propulsion parameters.

Figure I.1: Uncertainty propagation inputs and resulting mass distributions for the two-stage launch vehicle.

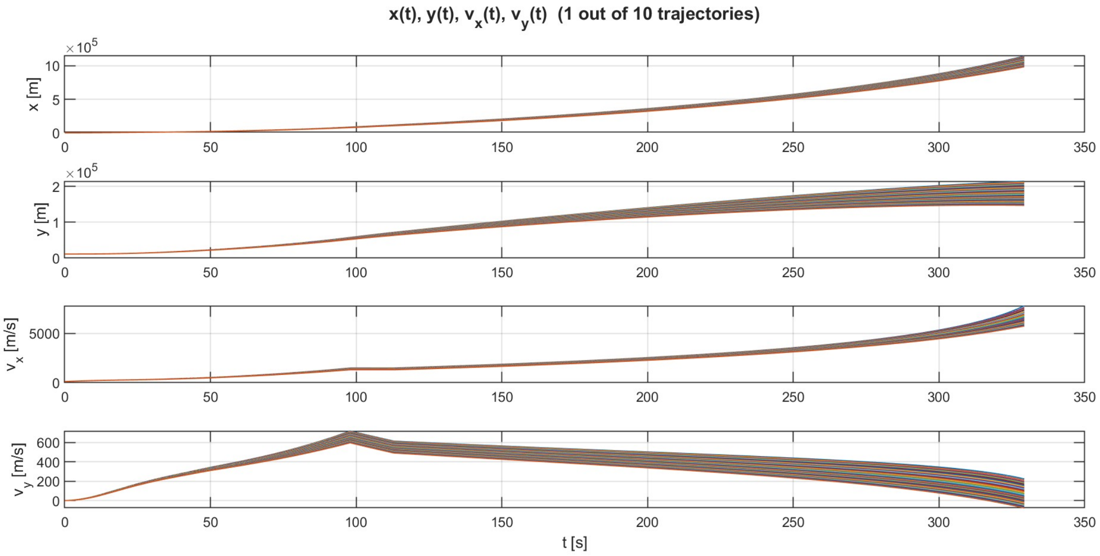

(a) Time histories of position and velocity components for a subset of stochastic trajectories.

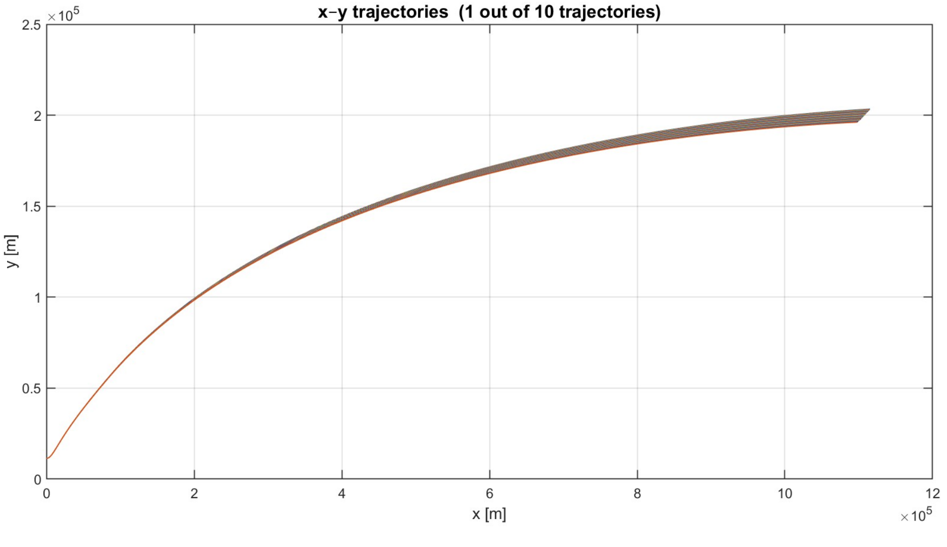

(b) x–y plane trajectories for the same stochastic realization subset.

Figure I.2: Stochastic ascent trajectory dispersion illustrated through state variables and physical trajectories.

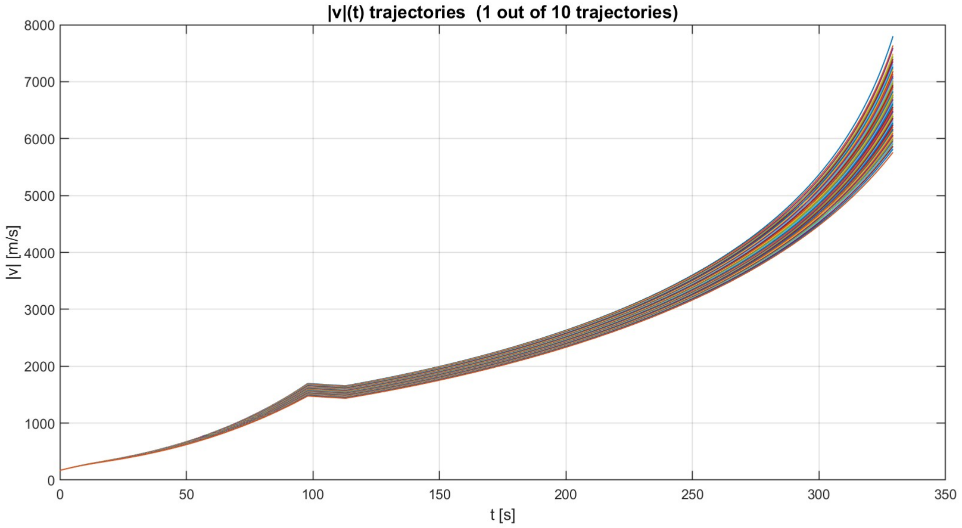

(c) Velocity magnitude time histories, showing dispersion during ascent for the selected trajectories.

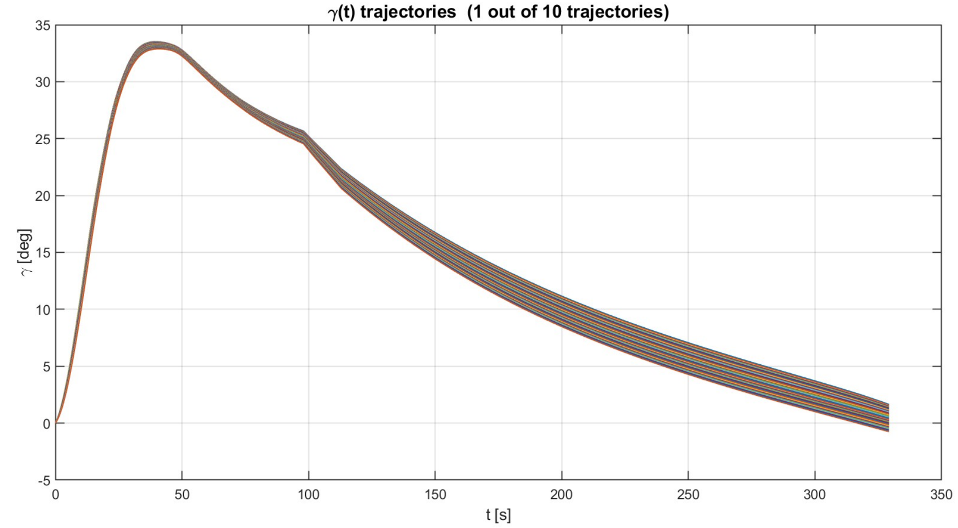

(d) Flight-path angle evolution as a function of time for the same stochastic trajectory subset.

Figure I.2: Stochastic ascent trajectory dispersion illustrated through velocity magnitude and flight-path angle time histories (continued).

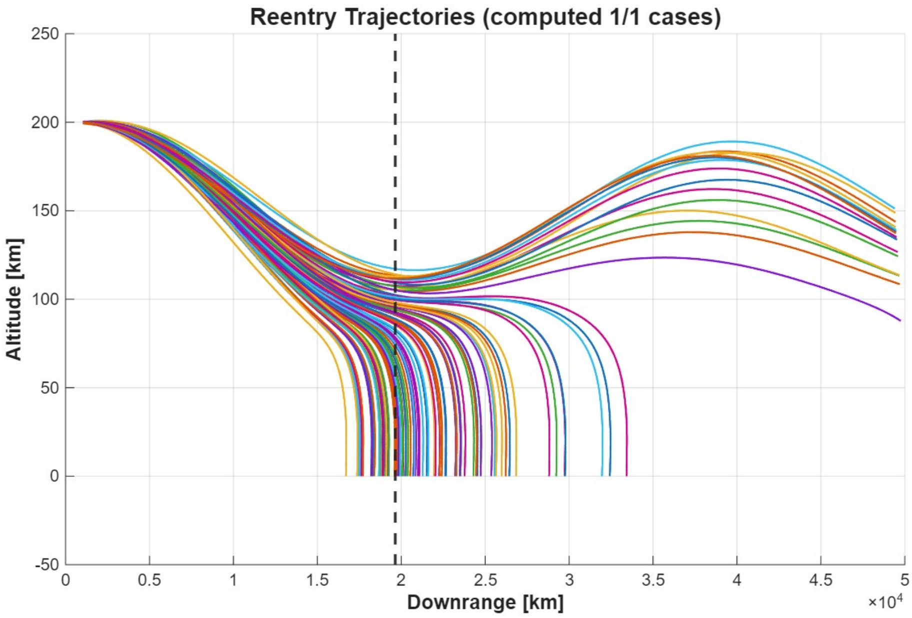

Figure I.3: Re-entry trajectory set (altitude vs. downrange) for the simulated cases. The vertical dashed line indicates the target downrange.

Landing Accuracy Analysis

This section presents a landing accuracy analysis for the re-entry capsule based on a numerical two-dimensional re-entry model. The total landing dispersion is modeled as the quadrature sum of four physically distinct and statistically independent error sources:

$$\sigma_{\text{tot}} = \sqrt{\sigma_{\text{wind}}^2 + \sigma_{\text{para,sys}}^2 + \sigma_{\text{entry}}^2 + \sigma_{\text{atm}}^2} \tag{I.10}$$

Before computing each contribution, the following subsections describe the physical origin and interpretation of each error term.

Meaning of Each Error Term

Entry Dispersion (σ_{entry})

This term represents the landing error caused by uncertainties in the state vector at atmospheric entry. It accounts for:

- navigation uncertainty at entry,
- stage separation errors,
- sensitivity to atmospheric deceleration.

Atmospheric Variability (σ_{atm})

Atmospheric density variations modify the aerodynamic drag force,

$$D = \frac{1}{2}\rho A C_D V^2, \tag{I.11}$$

thereby altering the deceleration path and producing dispersion in downrange impact. This term captures:

- meteorological density fluctuations,
- uncertainty in atmospheric models.

Parachute System Variability ($\sigma_{\mathrm{para,sys}}$)

Once the capsule transitions to subsonic flight under parachutes, small variations in drag coefficient or deployment timing directly affect the descent duration. Longer or shorter descent times result in increased or reduced exposure to wind drift. This term captures:

- dispersion in parachute drag coefficient C_D,
- variability in full-deployment altitude,
- terminal velocity variations.

Wind Drift During Parachute Descent (σ_{wind})

Wind drift represents the dominant low-altitude uncertainty. During parachute descent, the capsule drifts horizontally with the local wind:

$$\Delta x_{\mathrm{wind}} = V_{\mathrm{wind}}\, t_{\mathrm{desc}}. \tag{I.12}$$

Uncertainty in wind forecasts therefore produces direct landing dispersion. This term captures:

- unresolved local wind gusts,
- errors in meteorological prediction.

Entry Dispersion: Numerical Sensitivities

Entry dispersion is computed through numerical sensitivities of downrange distance with respect to entry velocity and flight-path angle using finite differences:

$$\frac{\partial R}{\partial V} = \frac{R(V+\Delta V) - R(V)}{\Delta V}, \tag{I.13}$$

$$\frac{\partial R}{\partial \gamma} = \frac{R(\gamma+\Delta\gamma) - R(\gamma)}{\Delta\gamma}. \tag{I.14}$$

The resulting entry-induced dispersion is given by:

$$\sigma_{\mathrm{entry}} = \sqrt{\left(\frac{\partial R}{\partial V}\sigma_V\right)^2 + \left(\frac{\partial R}{\partial \gamma}\sigma_\gamma\right)^2}. \tag{I.15}$$

Atmospheric Density Variability

Atmospheric density is scaled by ±10%, and the resulting change in downrange distance is used to compute the sensitivity:

$$K_{\mathrm{atm}} = \frac{R(+10\%) - R(-10\%)}{0.2}. \tag{I.16}$$

The atmospheric dispersion is then given by:

$$\sigma_{\mathrm{atm}} = |K_{\mathrm{atm}}|\,\sigma_{\rho,\mathrm{rel}}. \tag{I.17}$$

Parachute System Variability

Variations in parachute drag coefficient and effective deployment height modify the total descent time. The associated sensitivities are:

$$\frac{\partial t}{\partial C_{D,\mathrm{rel}}} = \frac{1}{2} t_{\mathrm{desc}}, \tag{I.18}$$

$$\frac{\partial t}{\partial H} = \frac{t_{\mathrm{desc}}}{H_{\mathrm{eff}}}. \tag{I.19}$$

The resulting parachute-induced time dispersion is:

$$\sigma_t^2 = \left(\frac{1}{2} t_{\mathrm{desc}} \sigma_{C_D}\right)^2 + \left(\frac{t_{\mathrm{desc}}}{H_{\mathrm{eff}}} \sigma_H\right)^2. \tag{I.20}$$

This time dispersion is converted into downrange dispersion through wind drift:

$$\sigma_{\mathrm{para,sys}} = V_{\mathrm{wind}} \sigma_t. \tag{I.21}$$

Wind Drift During Parachute Descent

The wind-induced dispersion during parachute descent is computed as:

$$\sigma_{\mathrm{wind}} = t_{\mathrm{desc}} \sigma_{V_{\mathrm{wind}}}. \tag{I.22}$$

Total Landing Accuracy

The final landing accuracy is obtained as:

$$\sigma_{\mathrm{tot}} = \sqrt{\sigma_{\mathrm{wind}}^2 + \sigma_{\mathrm{para,sys}}^2 + \sigma_{\mathrm{entry}}^2 + \sigma_{\mathrm{atm}}^2}. \tag{I.23}$$

Summary of Landing Accuracy Contributions

Table I.1: Summary of landing accuracy contributions (placeholder values).

Error Source	**1σ Dispersion [km]**
Wind drift	5.71
Parachute system errors	0.57
Entry state dispersion	2.26
Atmospheric variability	1.20
Total σ_{tot}	**6.29**

Appendix J

Carrier Analysis Details

Launch and landing site with 20km range around the exact antipode

Figure J.1: Launch and landing site with 20km range around the exact antipode

Possible flight path launching East

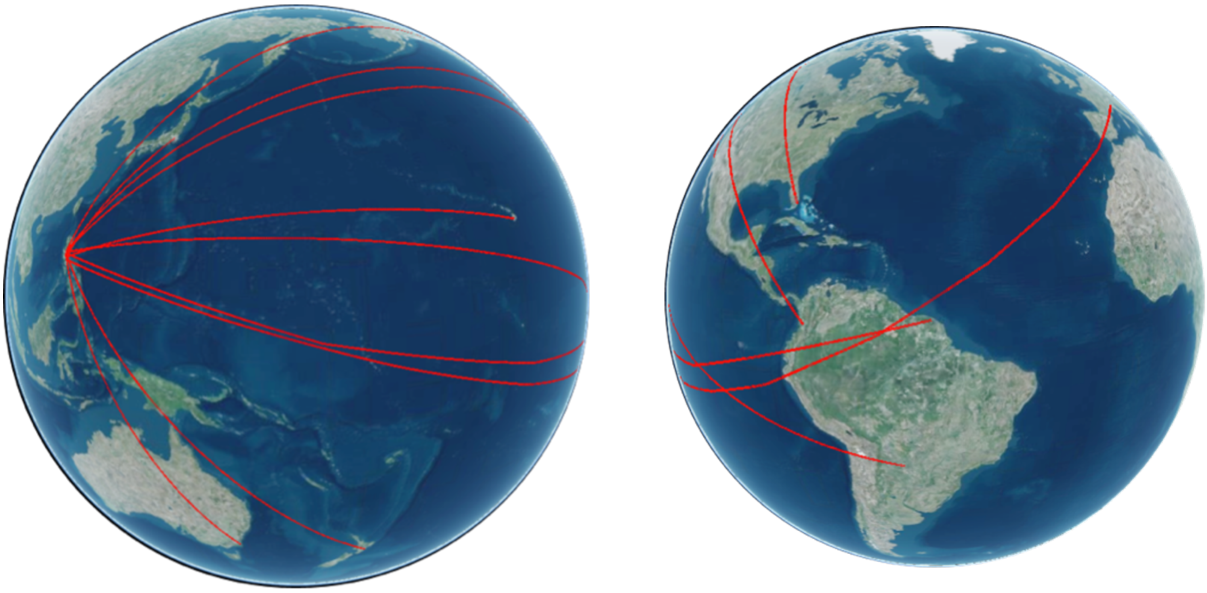

Figure J.2: Possible flight path launching East

Estimated flight envelope of Stratolauncher "Roc" with and without payload along with the projected Release point

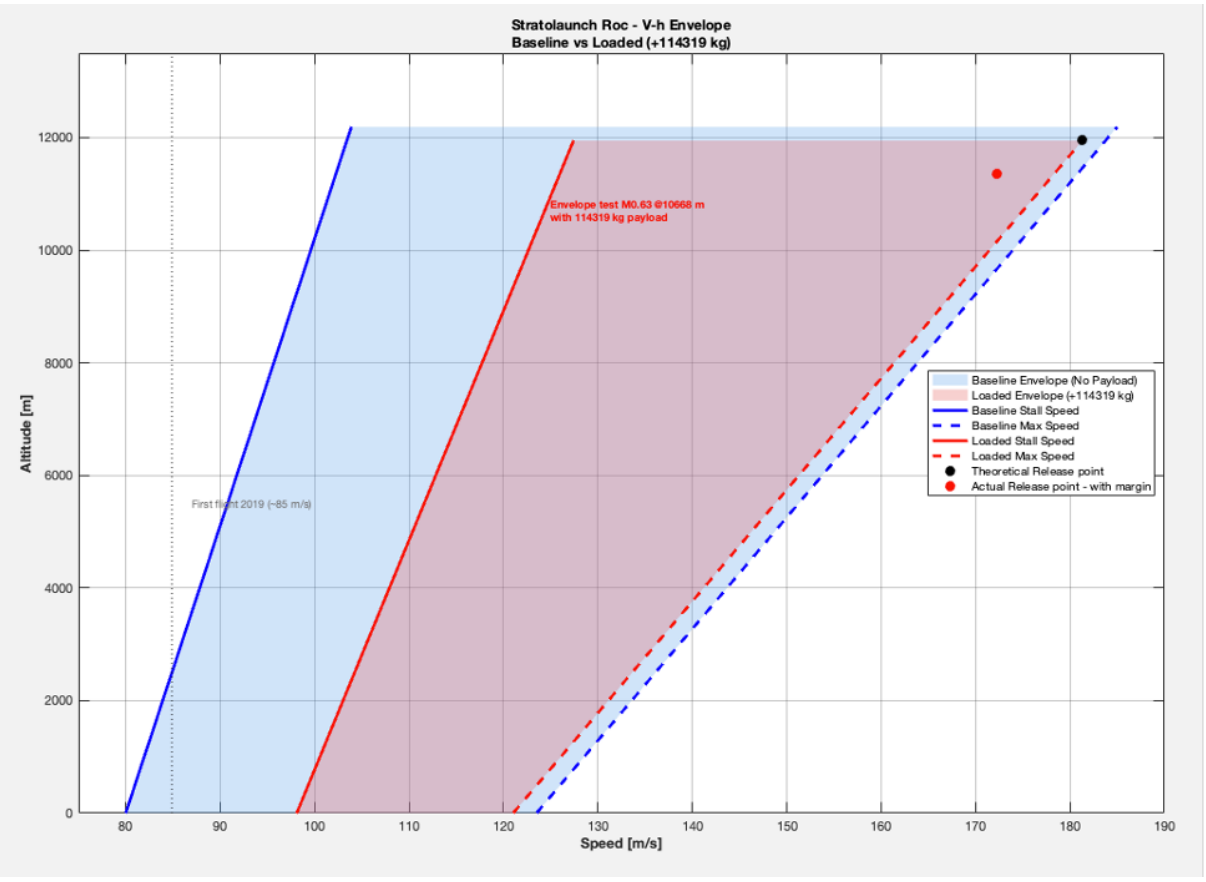

Figure J.3: Estimated flight envelope of Stratolauncher "Roc"

5s free fall plots for the altitude, velocity and trajectory

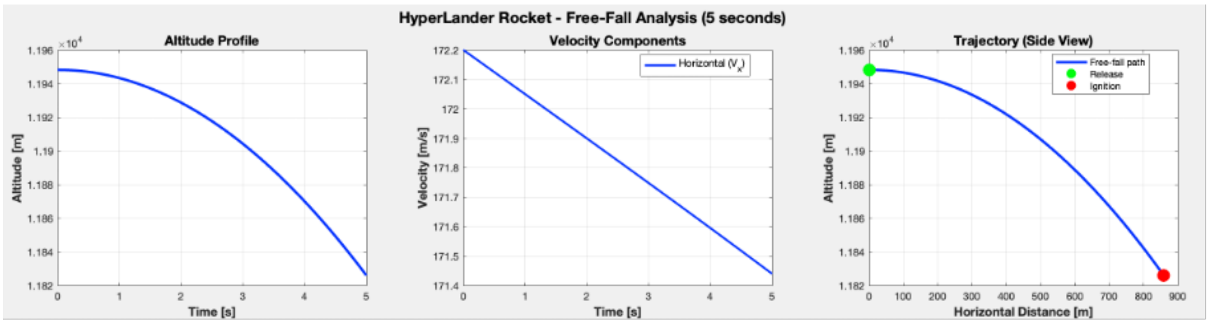

Figure J.4: 5s free fall plots for the altitude, velocity and trajectory

Supporting Calculations and Data Tables

Route Selection Criteria and Detailed Trajectory

The mission requires traveling from one point to its exact antipode on Earth, with a 20km tolerance. To explore the launch sites possibilities, here are the set of requirements:

- 3700m runway length for heavy vehicle takeoff
- Regulatory approval and Boeing 747 capability
- Flight path avoiding overpopulated areas, launching over ocean
- Proximity to equator for delta V gain
- Flat landing area

The selected launch site providing optimal delta V gain is: **Manila Airport, Philippines to near Bom Morto, west Brazil** (see Fig. J.2) . This route is advantageous as Manila Airport's proximity to the equator provides significant delta V from Earth's rotation. Additionally, Philippines and Brazil maintain good diplomatic relations, eliminating political concerns for this military mission.

Using the flight envelope parameters, and applying a 2% climb rate to obtain the following flight parameters:

Table J.1: Detailed Trajectory Parameters for Manila-Brazil Route

Trajectory - Route	**Value**
Time to climb (min)	58.9
Distance travelled (km)	569.743
Distance Left to travel (km)	**19467**
Initial latitude – Launch site (°)	14.515
Launch latitude – At release (°)	**13.181**
Inclination (°)	104.51
Delta V gain from earth rotation – At release (m/s)	**450.16**

Using trigonometry to calculate Earth's rotation speed at launch latitude, then modeling the carrier's ascent phase to estimate time to climb and distance covered before release. This allowed to determine the new latitude at release and calculate the precise delta V gain from Earth's rotation.

Polar Characterization of Stratolaunch Roc

The aerodynamic polar of the Stratolaunch *Roc* carrier aircraft has been reconstructed using publicly available flight-test data and official design information. Following standard subsonic transport aircraft methodology, a parabolic drag polar is assumed:

$$C_D = C_{D0} + kC_L^2. \tag{J.1}$$

Here, C_{D0} represents the zero-lift drag coefficient, while k is the induced drag factor.

From official Stratolaunch and Scaled Composites data [44], the main geometric parameters of the vehicle are:

- Wing area: $S \approx 900$ m^2,
- Wingspan: $b = 117.0$ m,
- Aspect ratio:

$$AR = \frac{b^2}{S} \approx 15.2. \tag{J.2}$$

The induced drag factor is computed assuming an Oswald efficiency factor $e \approx 0.80$, which is consistent with a high-aspect-ratio wing affected by twin-fuselage interference:

$$k = \frac{1}{\pi ARe} \approx \frac{1}{\pi \times 15.2 \times 0.80} \approx 0.026. \tag{J.3}$$

The zero-lift drag coefficient C_{D0} is estimated using the most constraining documented flight condition:

- Altitude: 35,000 ft [121],
- Mach number: $M = 0.63$,
- Aircraft mass: $\approx$ 440,000 kg (partially fueled, with hypersonic payload).

At this condition, the atmospheric properties are approximately $\rho \approx 0.40$ kg/m^3 and $V \approx 187$ m/s. Steady level flight requires a lift coefficient of about

$$C_L \approx 0.73. \tag{J.4}$$

Assuming a conservative target lift-to-drag ratio of

$$\left(\frac{L}{D}\right)_{\text{cal}} \approx 14, \tag{J.5}$$

the corresponding drag coefficient is

$$C_{D,\text{cal}} = \frac{C_L}{(L/D)_{\text{cal}}} \approx \frac{0.73}{14} \approx 0.052. \tag{J.6}$$

Substituting into the parabolic polar expression yields the zero-lift drag coefficient:

$$C_{D0} \approx C_{D,\text{cal}} - kC_L^2 \approx 0.052 - 0.026 \times (0.73)^2 \approx 0.038. \tag{J.7}$$

The final reconstructed aerodynamic polar for Stratolaunch Roc is therefore:

$$C_D = 0.038 + 0.026\,C_L^2. \tag{J.8}$$

This polar provides a maximum lift-to-drag ratio of approximately

$$\left(\frac{L}{D}\right)_{\text{max}} \approx 14.4 \tag{J.9}$$

at an optimal lift coefficient of

$$C_L \approx 0.72, \tag{J.10}$$

corresponding to the cruise condition.

The relatively high value of C_{D0} compared to conventional transport aircraft (typically 0.020–0.025) is consistent with the aerodynamic penalties introduced by the twin-fuselage configuration, pylons, and external payload integration [122] [123].

The reconstructed polar is consistent with three documented flight conditions (first flight at 17,000 ft and 164 kt [124], an intermediate test at 23,500 ft and 178 kt [125], and the calibration point [121]), all yielding lift-to-drag ratios in the range 14–15.6.

This aerodynamic model is subsequently used to compute the baseline theoretical flight envelope of the carrier aircraft, both with baseline payload and with the full 114,266 kg payload configuration.

Carrier Flight Envelope Analysis

To determine a suitable release altitude and speed, an analysis of Stratolaunch Roc's flight envelope using maiden flight data [124] combined with the above mentioned estimations for the aircraft's polar was performed. Since the program has never been tested at full payload capacity, the baseline flight envelope was modeled from a flight carrying a 2-ton payload. The projection of that flight condition at different altitudes and at the design payload was taken as the upper bound of the flight envelope. To determine the lower bound of the envelope a $\simeq 80 m/s$ minimum speed for liftoff (sea level) was assumed[1]; being more interested in upper bounds, this condition was not investigated further.

From the baseline flight envelope, the model configuration with the 114.266 t LV payload, gave the new maximum altitude, stall speed, and max speed. Results for the the upper bound for release conditions, applying a 5% safety margin on maximum speed (See Fig. J.3), are presented in Tab. J.2.

Table J.2: Maximum release conditions

Parameter	**Value**
Maximum release altitude	11 948.2 m
Maximum release speed	172.2 m/s

Rocket Free-Fall Analysis

To set realistic altitude and speed at ignition, a simple analysis was conducted on the rocket's 5-second free fall [2] after carrier release.

Using computed aerodynamic coefficients and release point data:

- $C_D = 0.55$ (drag coefficient below Mach 0.8)
- 114,266 kg payload mass
- 9.079 m^2 reference area

This study (See Figure J.4) does not consider the lift coefficient from the wings of the rocket and gives conservative performance estimates.

Table J.3: Free-Fall Losses and Ignition Conditions

Free fall losses	**Conditions at ignition**
• Altitude loss: 122.2 m • Horizontal speed loss: 0.76 m/s (0.44%) • Vertical speed gain: -48.97 m/s	• Altitude: 11,826 m • Horizontal velocity: 171.4 m/s • Vertical velocity: -48.97 m/s • Mach number: 0.612 • Distance covered while falling: 859 m

This analysis reveals a crucial element: modelling the free fall leads to a negative flight angle at ignition due to negative vertical velocity, therefore a non zero flight path angle would be required to the carrier. Not necessarily a pull up, yet at least a stationary climb.

---

[1] based on Boeing 747-400[126]

[2] based on Pegasus's operations[43]

By comparing data Tab. J.2 via the analysis in J.3 with the ignition conditions selected in Tab J.4, the available margins were considered in line with the design goals, yet shall be investigated further in next iterations.

γ_0	h_0	v_0
0°	11400 m	170 m/s

Table J.4: Ignition Conditions

Final Launch Parameters Summary

Table J.5: Final Launch Parameters at Rocket Ignition

Trajectory – At ignition	**Value**
Distance travelled (km)	569
Distance Left to travel – at ignition (km)	**19467**
Initial Altitude – at ignition (m)	**11400**
Initial Speed – at ignition (m/s)	**170**
Delta V gain from earth rotation – at ignition (m/s)	**450.16**
TOTAL Delta V gain – at ignition (m/s)	**608.2**

In the end, the total Delta V gained is 608.2 m/s for the rocket, releasing at 11400m and 170 m/s.

Appendix K

Further Guidance & Control Insights

Mass and Inertia Modeling

The mass properties of aerospace vehicles are commonly modeled as time-varying quantities in order to account for propellant consumption, staging events, and changes in mass distribution throughout the flight [58]. In this study, the vehicle is represented as a multi-segment rigid body system consisting of the first stage, second stage, payload capsule, and launch abort system (LAS).

The total mass of the vehicle at time t is expressed as the sum of the individual segment masses [58]:

$$m(t) = \sum_{i=1}^{n} m_i(t), \tag{K.1}$$

where n denotes the number of vehicle segments and $m_i(t)$ represents the time-varying mass of the i-th segment. In this study, $n = 4$.

The longitudinal center of gravity location of the vehicle is computed using the standard mass-weighted formulation for composite bodies [58]:

$$x_{\text{cg}}(t) = \frac{\sum_{i=1}^{n} m_i(t)\, x_i(t)}{\sum_{i=1}^{n} m_i(t)}, \tag{K.2}$$

where $x_i(t)$ denotes the center of gravity location of the i-th segment measured along the body-fixed longitudinal axis. The mass moment of inertia of the vehicle about the out-of-plane axis passing through the overall center of gravity is calculated using the parallel axis theorem for composite rigid bodies [58]:

$$I_{\text{cg}}(t) = \sum_{i=1}^{n} \left(I_i(t) + m_i(t)\, r_i^2(t) \right), \tag{K.3}$$

where $I_i(t)$ is the moment of inertia of the i-th segment about its own center of gravity, and $r_i(t)$ is the distance between the center of gravity of the i-th segment and the overall center of gravity.

To estimate the inertia properties of geometrically complex vehicle components, simplified geometric representations are commonly employed [58]. In this work, the first and second stages are modeled as rectangular bodies, while the payload capsule and the launch abort system are approximated as an isosceles trapezoid and an isosceles triangle, respectively. The geometric moments of inertia of these components are first computed based on their shape and dimensions and subsequently converted into mass moments of inertia using the corresponding mass-to-area ratios.

The mass and inertia properties of the vehicle are evaluated over four distinct flight phases to ensure physical consistency across propulsion and staging events [58]:

First stage burn → Coast phase prior to stage separation → Coast phase following stage separation → Second stage burn

Different mass distributions, reference frames, and active vehicle components are adopted for each flight phase in order to accurately capture the dynamic evolution of the vehicle mass properties throughout the mission.

PID Control Law Formulation

The thrust vector deflection angle $\delta(t)$ is generated by a proportional–integral–derivative (PID) controller acting on the pitch tracking error $e_\theta(t) = \theta_{\text{ref}}(t) - \theta(t)$. Therefore, the control law is defined as [127]:

$$\delta(t) = K_P e_\theta(t) + K_I \int_0^t e_\theta(\tau)\, d\tau + K_D \dot{e}_\theta(t), \tag{K.4}$$

where K_P, K_I, and K_D denote the proportional, integral, and derivative gains, respectively.

Additional Guidance and Control Results

This appendix presents additional simulation results for the second stage of flight to provide further insight into the guidance and control performance. The figures illustrate the evolution of key flight variables and demonstrate the consistency between the optimized reference trajectories and the controlled response.

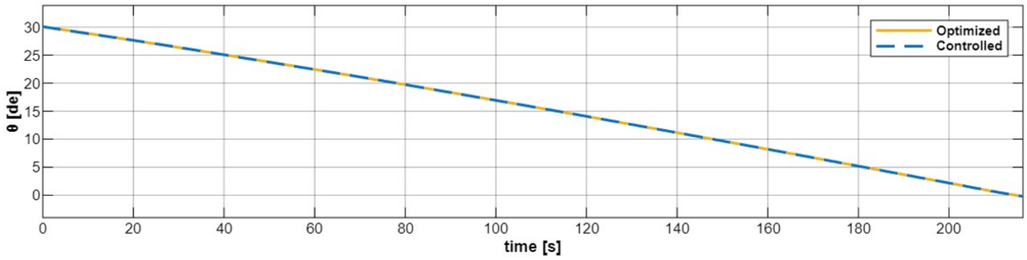

Figure K.1: Optimized and controlled pitch angle during the second stage.

Fig. K.1 demonstrates that the controlled pitch angle closely follows the optimized reference throughout the maneuver.

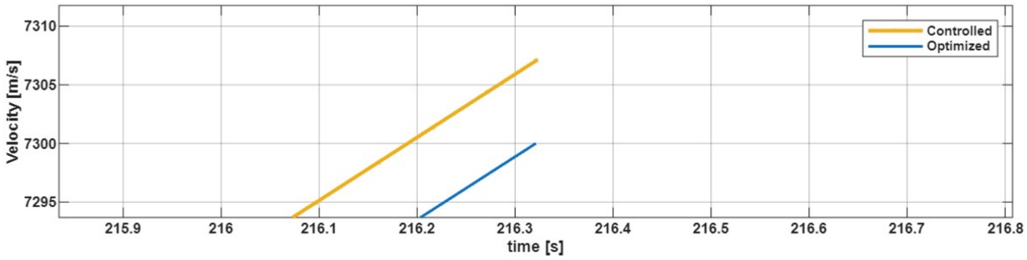

Figure K.2: Optimized and controlled total velocity during the second stage.

Fig. 9.1 shows the commanded thrust vector deflection angle. An initial transient due to uncertainty in the initial pitch rate and derivative action is observed, after which small thrust vector deflections are sufficient to maintain trajectory tracking, indicating limited control effort.

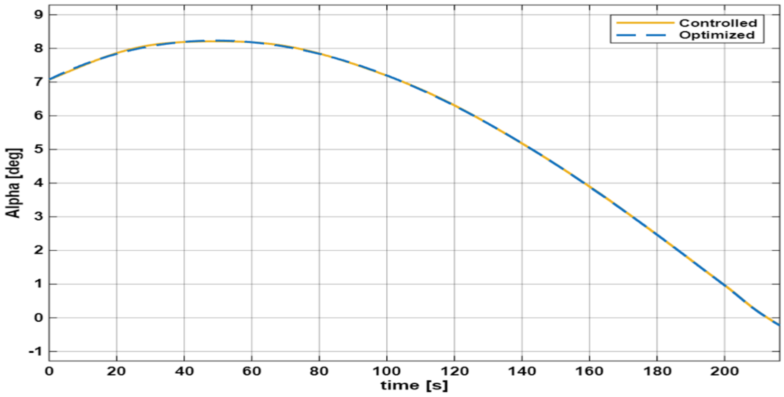

Figure K.3: Time history of the angle of attack during the second stage, comparing the optimized reference and the controlled response.

Fig. K.3 shows the angle of attack evolution during the second stage. The controlled response closely follows the optimized reference throughout the maneuver, indicating effective regulation of aerodynamic loading.

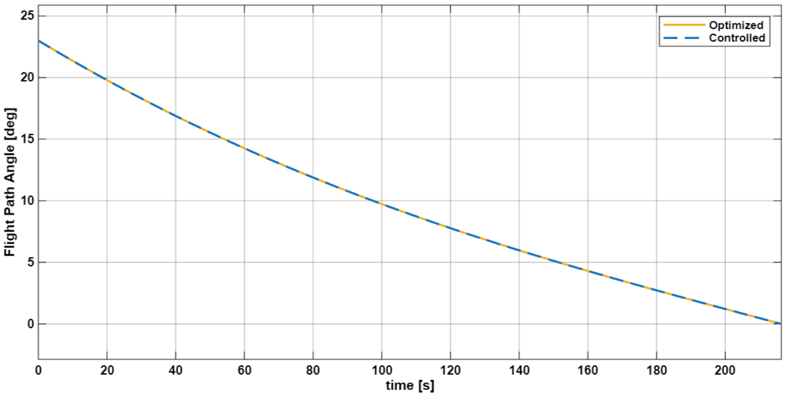

Figure K.4: Flight path angle during the second stage for the optimized and controlled trajectories.

Fig. K.4 illustrates the flight path angle evolution. The near-perfect overlap between the optimized and controlled profiles confirms accurate trajectory tracking in the inertial frame.

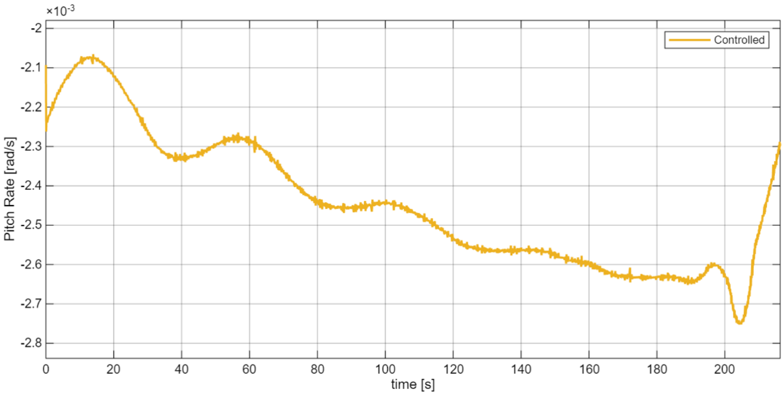

Figure K.5: Pitch rate response of the controlled vehicle during the second stage.

Fig. K.5 presents the pitch rate of the controlled vehicle. Small oscillations are observed during the initial transient, followed by a smooth response, proving sufficient damping by the control law.

Appendix L

Trajectory Data & Validation

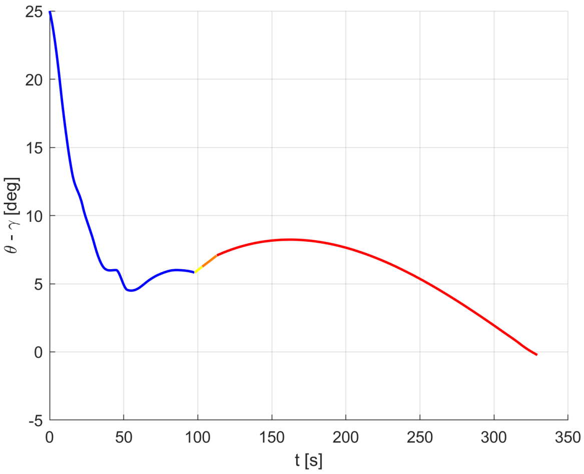

Figure L.1: $\alpha(t) = \theta(t) - \gamma(t)$.

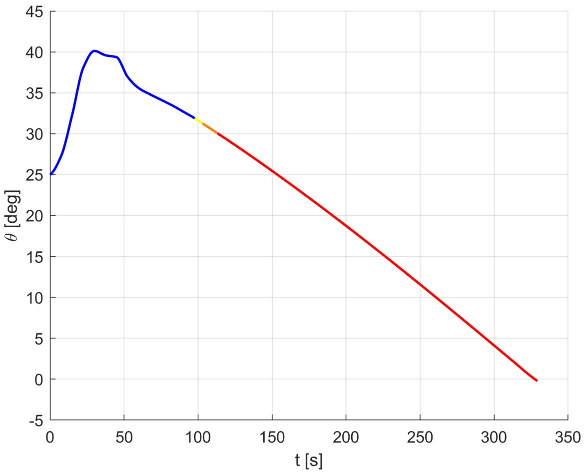

Figure L.2: Optimal $\theta(t)$

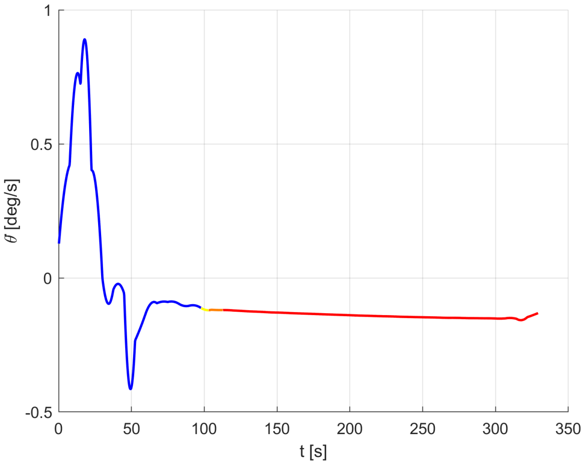

Figure L.3: pitch rate $\dot{\theta}(t)$.

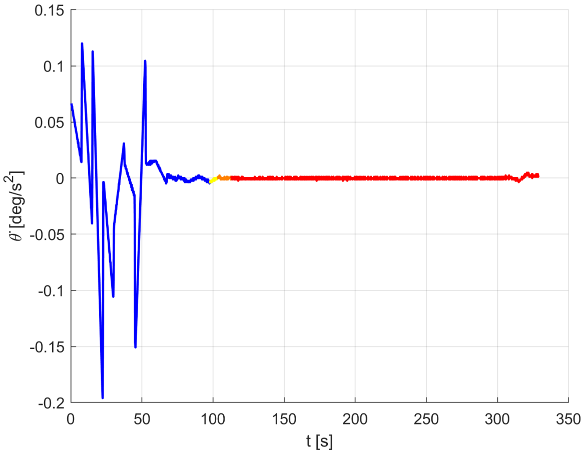

Figure L.4: angular acceleration $\ddot{\theta}(t)$.

[redacted]

Figure L.5: Pegasus’s $\alpha(t)$ and dynamic pressure according to first test flight [16].

[redacted]

Figure L.6: Pegasus’s ascent profiles according to [38].

[redacted]

Figure L.7: Pegasus’s altitude profile according to first mission data [15]

[redacted]

Figure L.8: Pegasus’s aerodynamic coefficients according to first mission data [15].

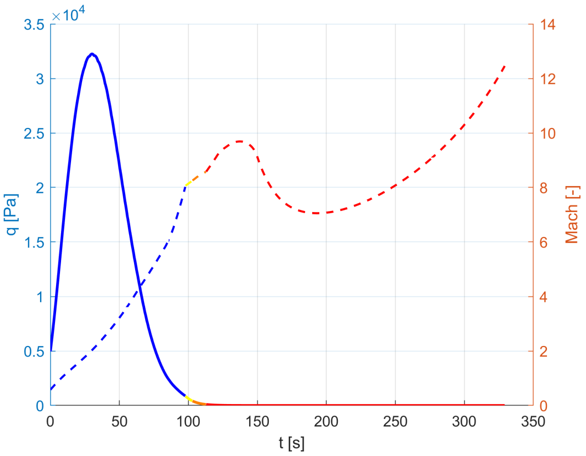

Figure L.9: Dynamic pressure and Mach number profiles.

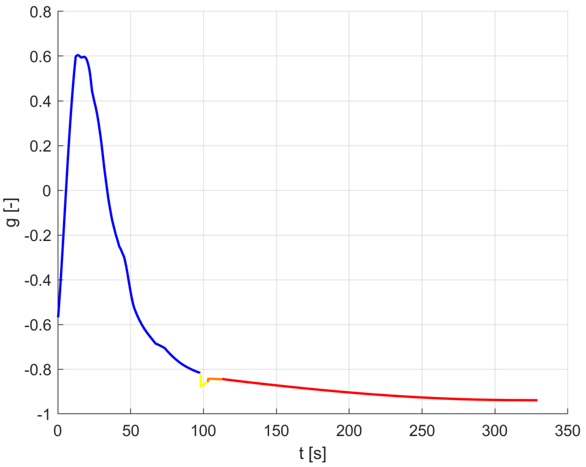

Figure L.10: Normal Accelerations in g-load

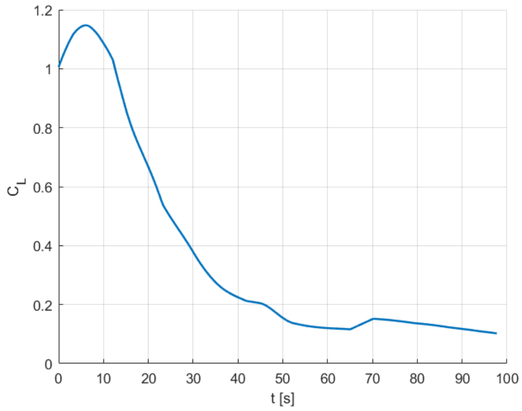

Figure L.11: C_L from nominal trajectory (first stage).

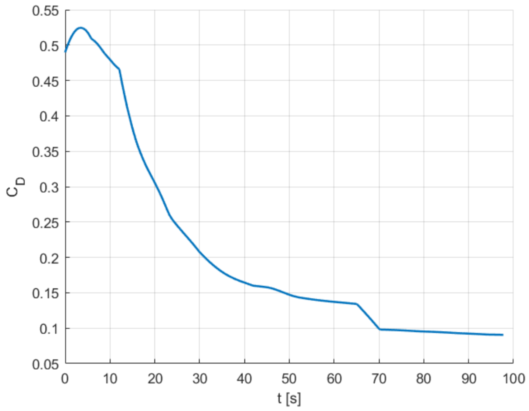

Figure L.12: C_D from nominal trajectory (first stage).

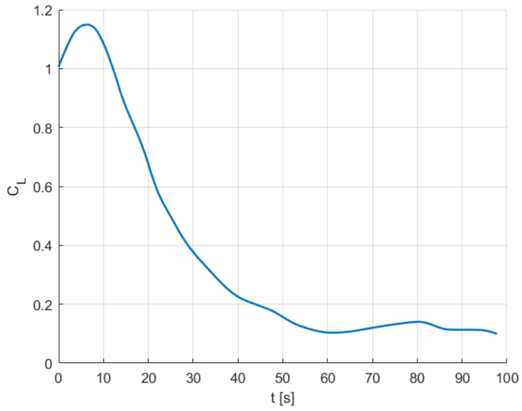

Figure L.13: C_L from trajectory with model smoothing implemented(first stage).

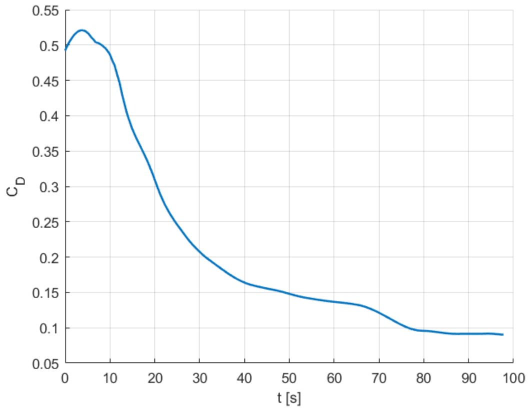

Figure L.14: C_L from trajectory with model smoothing implemented(first stage).

Appendix M

Functional Analysis & Requirements Allocation

This appendix presents the functional analysis and requirement's system allocation for the Hyper-Lander concept design. The analysis breaks down the mission into three main operational phases: Pre-launch, Ascent Operations, and Recovery. Each phase is further decomposed into primary functions and subfunctions to illustrate the sequence of operations and system interdependencies.

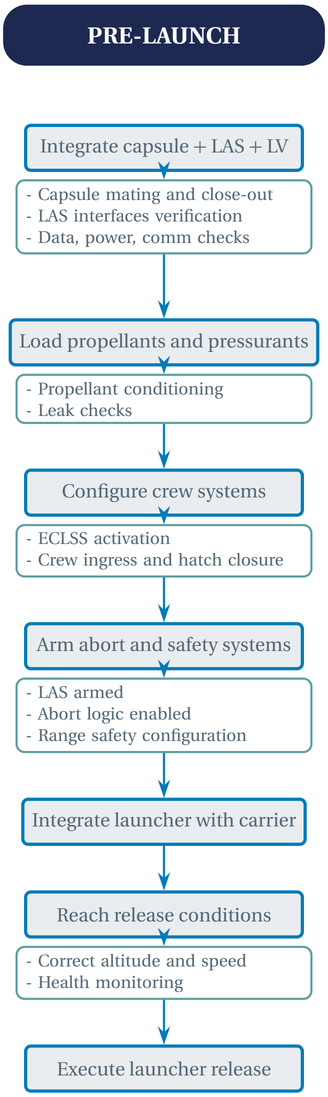

Figure M.1: Functional Analysis — Pre-launch phase.

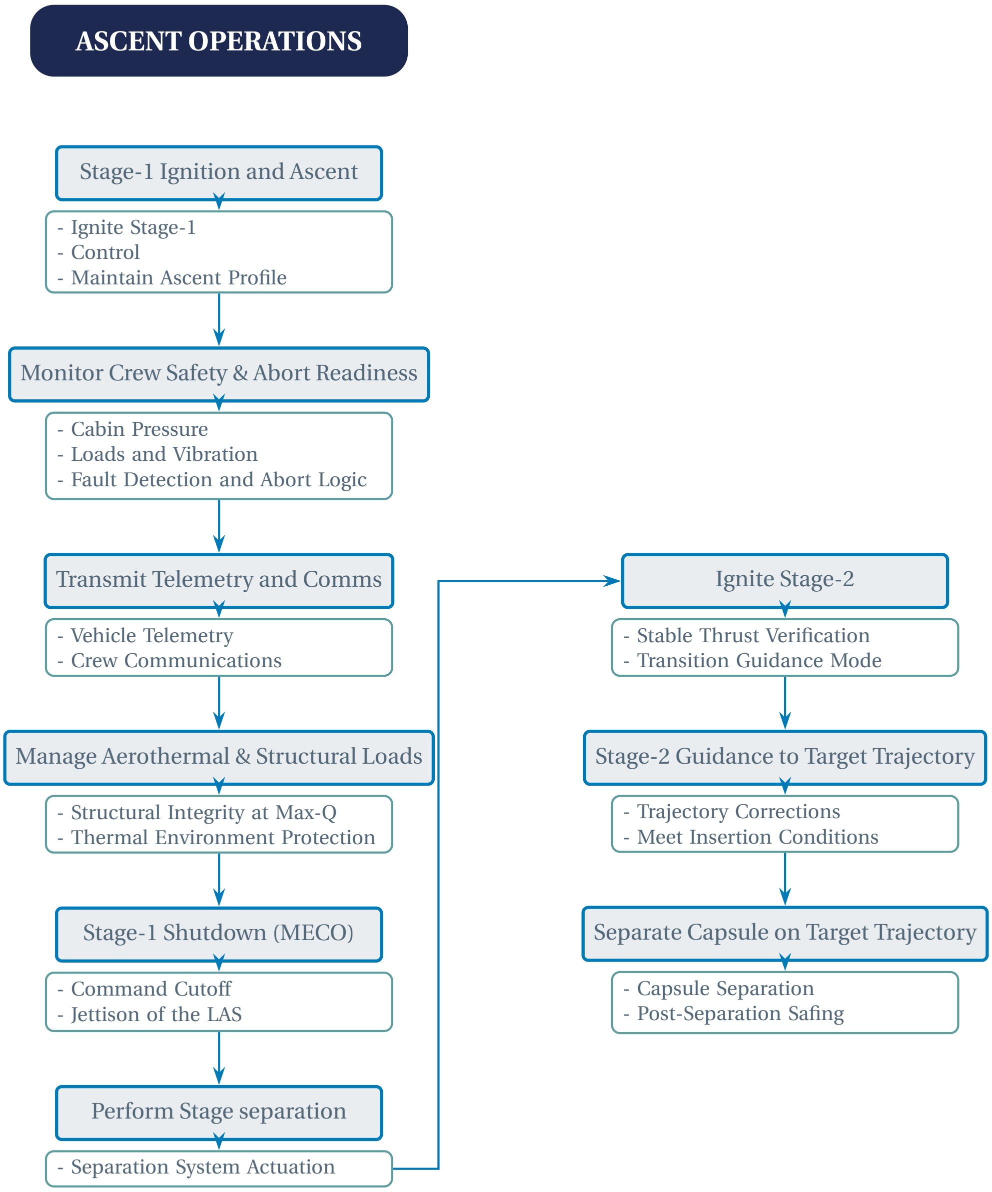

Figure M.2: Functional Analysis — Ascent operations.

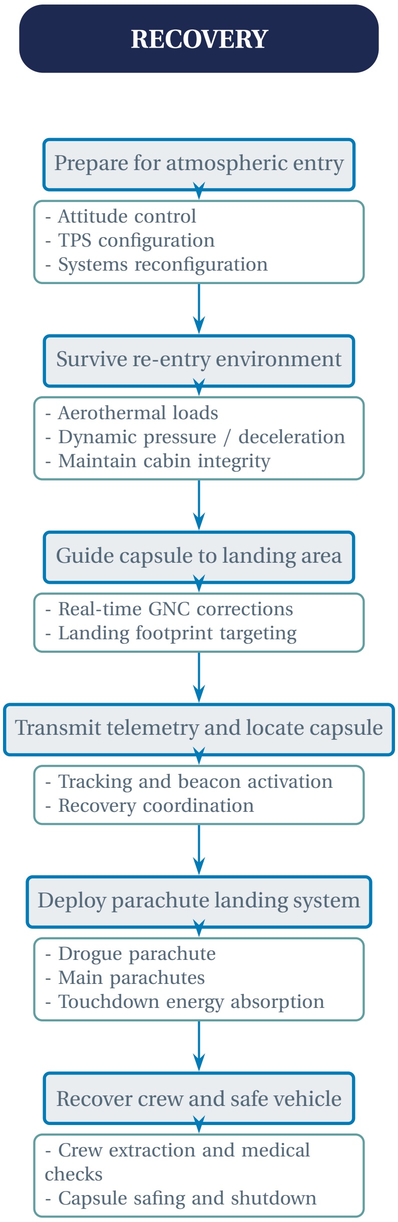

Figure M.3: Functional Analysis — Recovery phase.

The functional analysis presented in this appendix provides a systematic breakdown of the HyperLander mission operations. The three phases — Pre-launch, Ascent Operations, and Recovery — encompass all critical functions required for mission success. Each function has been defined with associated subfunctions to ensure comprehensive coverage of operational requirements.

The color coding used in the diagrams follows a logical hierarchy:

- Dark blue: Main operational phases
- Medium blue: Primary functions and flow arrows
- Cadet blue: Subfunction borders
- Light blue: Function backgrounds

This analysis serves as the foundation for detailed system design and operational planning for the project.

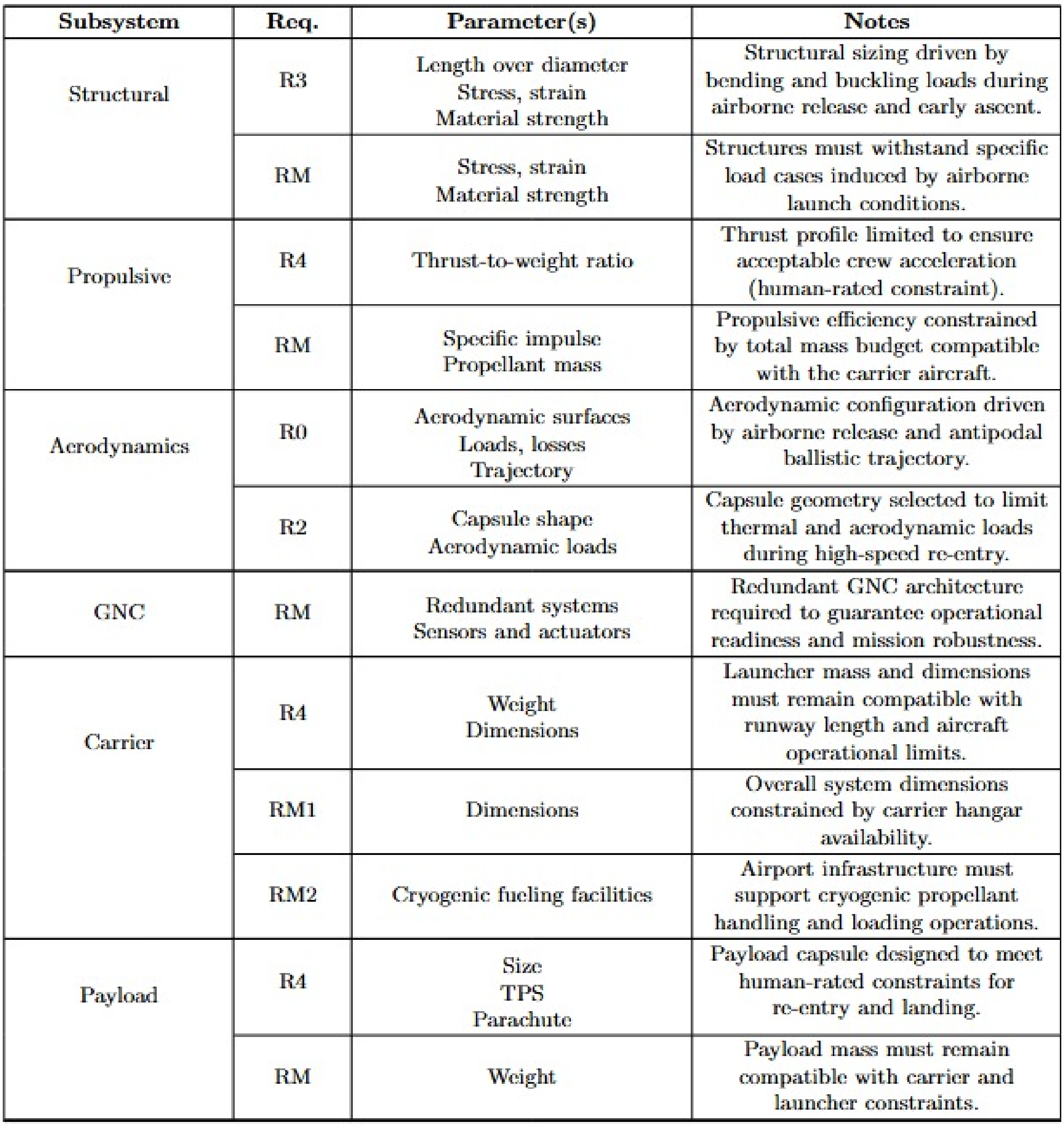

Subsystem	Req.	Parameter(s)	Notes
Structural	R3	Length over diameter Stress, strain Material strength	Structural sizing driven by bending and buckling loads during airborne release and early ascent.
	RM	Stress, strain Material strength	Structures must withstand specific load cases induced by airborne launch conditions.
Propulsive	R4	Thrust-to-weight ratio	Thrust profile limited to ensure acceptable crew acceleration (human-rated constraint).
	RM	Specific impulse Propellant mass	Propulsive efficiency constrained by total mass budget compatible with the carrier aircraft.
Aerodynamics	R0	Aerodynamic surfaces Loads, losses Trajectory	Aerodynamic configuration driven by airborne release and antipodal ballistic trajectory.
	R2	Capsule shape Aerodynamic loads	Capsule geometry selected to limit thermal and aerodynamic loads during high-speed re-entry.
GNC	RM	Redundant systems Sensors and actuators	Redundant GNC architecture required to guarantee operational readiness and mission robustness.
Carrier	R4	Weight Dimensions	Launcher mass and dimensions must remain compatible with runway length and aircraft operational limits.
	RM1	Dimensions	Overall system dimensions constrained by carrier hangar availability.
	RM2	Cryogenic fueling facilities	Airport infrastructure must support cryogenic propellant handling and loading operations.
Payload	R4	Size TPS Parachute	Payload capsule designed to meet human-rated constraints for re-entry and landing.
	RM	Weight	Payload mass must remain compatible with carrier and launcher constraints.

Figure M.4: General system's requirements allocation.

Appendix N

Optimal Staging

Problem definition

A two-stage launch vehicle is considered with a prescribed total mission requirement

$$\Delta V_1 + \Delta V_2 = \Delta V_{\text{req}}, \qquad \Delta V_i \geq 0. \tag{N.1}$$

A Launch Abort System (LAS) of mass m_{LAS} is attached at lift-off and jettisoned at second-stage ignition. As a consequence, stage 2 accelerates a reduced upper mass compared to stage 1.

Objective The objective is to minimize the lift-off mass:

$$\min\ m_{0,1}. \tag{N.2}$$

Rocket equation and mass-ratio formalism

Each stage $i \in \{1,2\}$ is modeled with constant specific impulse $I_{sp,i}$, defining the effective exhaust velocity

$$v_{e,i} = g_0 I_{sp,i}. \tag{N.3}$$

The mass ratio required to deliver ΔV_i is given by the Tsiolkovsky equation:

$$R_i = \frac{m_{0,i}}{m_{f,i}} = \exp\left(\frac{\Delta V_i}{v_{e,i}}\right), \qquad \Delta V_i = v_{e,i} \ln R_i. \tag{N.4}$$

Here $m_{0,i}$ and $m_{f,i}$ are respectively the ignition and burnout masses of stage i.

Structural mass fraction and stage growth factor

Let $m_{s,i}$ and $m_{p,i}$ be the dry structural mass and propellant mass of stage i. The structural mass fraction is defined as

$$\varepsilon_i = \frac{m_{s,i}}{m_{s,i} + m_{p,i}}, \qquad 0 < \varepsilon_i < 1. \tag{N.5}$$

Let $m_{\text{upper},i}$ denote the mass carried above stage i at ignition. Then

$$m_{0,i} = (m_{s,i} + m_{p,i}) + m_{\text{upper},i}, \tag{N.6}$$

$$m_{f,i} = m_{s,i} + m_{\text{upper},i}. \tag{N.7}$$

From the definition of ε_i,

$$m_{s,i} = \frac{\varepsilon_i}{1-\varepsilon_i}\, m_{p,i}. \tag{N.8}$$

Combining this relation with the rocket equation yields the stage growth factor :

$$\lambda_i = \frac{m_{0,i}}{m_{\text{upper},i}} = \frac{R_i(\varepsilon_i - 1)}{R_i \varepsilon_i - 1}. \tag{N.9}$$

Feasibility condition The growth factor is physically meaningful only if

$$R_i < \frac{1}{\varepsilon_i} \qquad \Leftrightarrow \qquad R_i \varepsilon_i - 1 < 0, \tag{N.10}$$

otherwise the required mass would diverge.

Growth factor as a function of ΔV_i Since $R_i = \exp(\Delta V_i / v_{e,i})$,

$$\lambda_i(\Delta V_i) = \frac{\exp(\Delta V_i / v_{e,i})(\varepsilon_i - 1)}{\varepsilon_i \exp(\Delta V_i / v_{e,i}) - 1}. \tag{N.11}$$

LAS separation and upper-mass definitions

With LAS jettison at second-stage ignition, the upper masses are

$$m_{\text{upper},2} = m_{PL}, \tag{N.12}$$

$$m_{\text{upper},1} = m_{0,2} + m_{\text{LAS}}. \tag{N.13}$$

Using the growth factor,

$$m_{0,2} = \lambda_2 m_{PL}, \tag{N.14}$$

and therefore the lift-off mass becomes

$$m_{0,1} = \lambda_1 \big(\lambda_2 m_{PL} + m_{\text{LAS}}\big). \tag{N.15}$$

This expression captures the effect of LAS separation: the LAS penalizes stage 1 only, hence tends to shift the optimal ΔV toward stage 2.

Optimization problem

Decision variables and constraints

The decision variables can be taken as either $(\Delta V_1, \Delta V_2)$ or equivalently (R_1, R_2):

$$R_1 = \exp\left(\frac{\Delta V_1}{v_{e,1}}\right), \qquad R_2 = \exp\left(\frac{\Delta V_2}{v_{e,2}}\right). \tag{N.16}$$

The mission constraint is $\Delta V_1 + \Delta V_2 = \Delta V_{\text{req}}$, together with the feasibility constraints for both stages.

Lagrangian formulation

To avoid confusion with the growth factors λ_i, the Lagrange multiplier is denoted Λ. The constrained problem is

$$\min_{\Delta V_1, \Delta V_2} m_{0,1}(\Delta V_1, \Delta V_2) \quad \text{s.t.} \quad \Delta V_1 + \Delta V_2 = \Delta V_{\text{req}}. \tag{N.17}$$

The Lagrangian is

$$\mathscr{L} = m_{0,1}(\Delta V_1, \Delta V_2) + \Lambda(\Delta V_1 + \Delta V_2 - \Delta V_{\text{req}}). \tag{N.18}$$

Stationarity yields

$$\frac{\partial m_{0,1}}{\partial \Delta V_1} = \frac{\partial m_{0,1}}{\partial \Delta V_2} = -\Lambda. \tag{N.19}$$

Meaning of Λ At optimum, Λ represents the marginal penalty in lift-off mass per unit increase in mission requirement:

$$\Lambda = \frac{\partial m_{0,1}^{\star}}{\partial \Delta V_{\text{req}}} \left[\frac{\text{kg}}{\text{m s}^{-1}}\right]. \tag{N.20}$$

Final formulas for the ΔV split

Using the mission constraint,

$$\Delta V_2 = \Delta V_{\text{req}} - \Delta V_1. \tag{N.21}$$

The mass ratios become

$$R_1(\Delta V_1) = \exp\left(\frac{\Delta V_1}{v_{e,1}}\right), \tag{N.22}$$

$$R_2(\Delta V_1) = \exp\left(\frac{\Delta V_{\text{req}} - \Delta V_1}{v_{e,2}}\right). \tag{N.23}$$

The corresponding growth factors are

$$\lambda_1(\Delta V_1) = \frac{R_1(\varepsilon_1 - 1)}{R_1\varepsilon_1 - 1}, \tag{N.24}$$

$$\lambda_2(\Delta V_1) = \frac{R_2(\varepsilon_2 - 1)}{R_2\varepsilon_2 - 1}. \tag{N.25}$$

Substituting into the lift-off mass expression yields the one-variable objective:

$$m_{0,1}(\Delta V_1) = \lambda_1(\Delta V_1)\big[\lambda_2(\Delta V_{\text{req}} - \Delta V_1) m_{PL} + m_{\text{LAS}}\big]. \tag{N.26}$$

Closed-form optimality equation

The optimum satisfies

$$\frac{d}{d\Delta V_1} m_{0,1}(\Delta V_1) = 0. \tag{N.27}$$

Since $\lambda_i = \lambda_i(R_i)$ with $R_i = \exp(\Delta V_i / v_{e,i})$,

$$\frac{d\lambda_i}{d\Delta V_i} = \frac{(1-\varepsilon_i)R_i}{v_{e,i}(R_i\varepsilon_i - 1)^2}. \tag{N.28}$$

Applying the optimality condition gives

$$\left(\frac{d\lambda_1}{d\Delta V_1}\right)(\lambda_2 m_{PL} + m_{\text{LAS}}) = \lambda_1 m_{PL}\left(\frac{d\lambda_2}{d\Delta V_2}\right), \qquad \Delta V_2 = \Delta V_{\text{req}} - \Delta V_1. \tag{N.29}$$

Once solved numerically for $\Delta V_1^{\star}$,

$$\Delta V_2^{\star} = \Delta V_{\text{req}} - \Delta V_1^{\star}, \tag{N.30}$$

$$R_1^{\star} = \exp\left(\frac{\Delta V_1^{\star}}{v_{e,1}}\right), \tag{N.31}$$

$$R_2^{\star} = \exp\left(\frac{\Delta V_2^{\star}}{v_{e,2}}\right). \tag{N.32}$$

Appendix O

Atmospheric Model

In the whole design process the US 1976 standard atmosphere model was adopted [110].

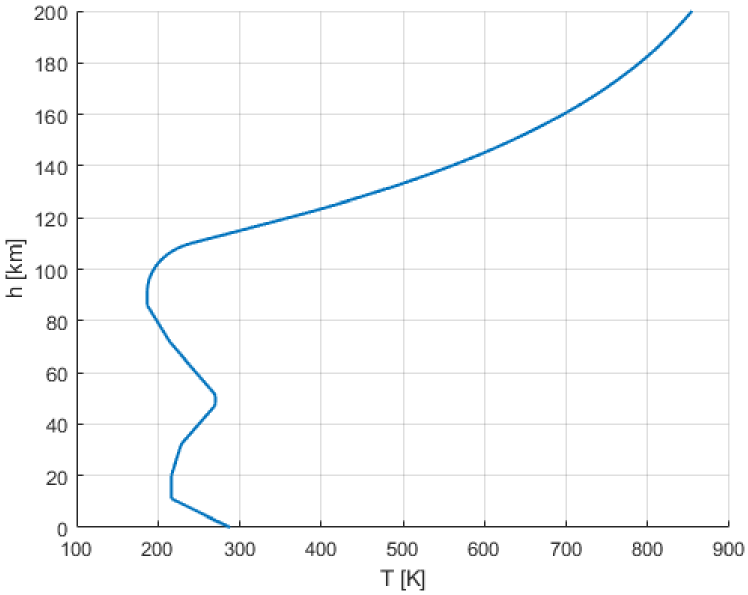

Figure O.1: Temperature Profile

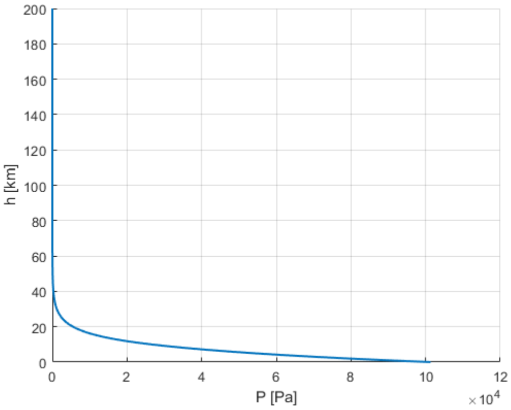

Figure O.2: Pressure Profile

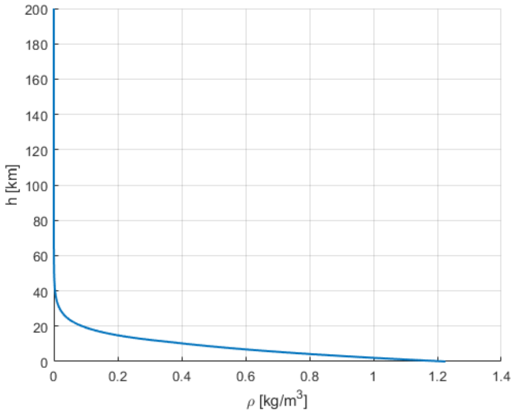

Figure O.3: Density Profile

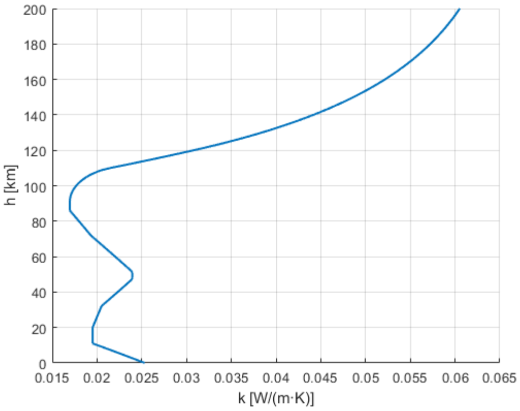

Figure O.4: Thermal Conductivity Profile

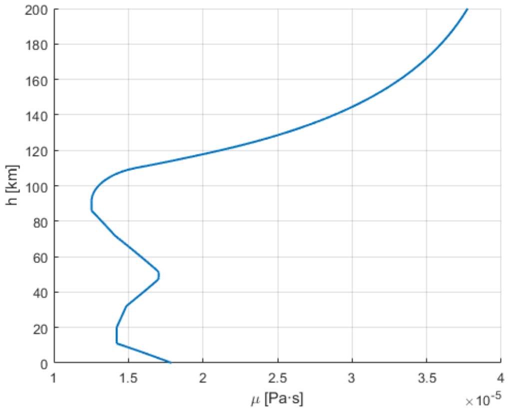

Figure O.5: Dynamic Viscosity Profile